PhD Thesis

Superconducting double quantum dot hybrids in parallel InAs nanowires

Olivér Csaba Kürtössy

Supervisor: Dr. Szabolcs Csonka
Associate Professor

Budapest University of Technology and Economics
Department of Physics
2024

Contents

List of abbreviations

ABS	Andreev bound state
BCS	Bardeen-Cooper-Schrieffer
CAR	crossed Andreev reflection
CPS	Cooper pair splitting
DOS	density of states
EBL	electron beam lithography
EC	elastic cotunneling
IVC	inner vacuum chamber
LAR	local Andreev reflection
LPT	local pair tunneling
MBE	molecular beam epitaxy
MF	Majorana fermion
OVC	outer vacuum chamber
QD	quantum dot
RHEED	reflection high-energy electron diffraction
SC	superconductor
SCI	superconducting island
SEM	scanning electron microscopy
TEM	transmission electron microscopy
UHV	ultra high vacuum
YSR	Yu-Shiba-Rusinov
ZBA	zero bandwidth approximation

Chapter 1

Introduction

The limits of classical computation became evident in the past decades. The tendency to increase the number of transistors on a chip is likely unsustainable in the long run [1,2]. This is not only a constraint for the capacity of the stored information but restricts the speed of its processing as well. This restraint with the deficiency and lack of innovation in silicon technology outlined the necessity of novel devices based on the laws of quantum mechanics [3]. In contrast to classical bits, a quantum mechanical two-level system constituting a quantum bit (or qubit) can take an arbitrary superposition of its two basis states [4–7]. The entanglement of these quantum devices can be utilized for such algorithms, e.g. in the field of cryptography, which are not accessible for classical computers [8–12]. This conceptually different approach inspired the scientific community of quantum electronics to establish and manipulate qubits, as the main goal of this field of modern physics, and by now, quantum supremacy over classical data processing has also been reported as a milestone in the field [13].

Recently, a wide variety of qubits have been revealed [14]. Besides spin qubits [15–21], diverse superconducting qubits, like flux (or fluxonium) [22–27], Andreev [28–31], charge qubits [32–34], transmons [35–40], or gatemons [41,42] are particularly popular nowadays since the superconductors (SCs) intrinsically provide entangled electrons by Cooper pairs. The main concerns of most qubits listed above are their instability, the susceptibility to external noises, and the decoherence to them. A. Kitaev suggested the application of anyons as the fundamental units of universal logic gates [43]. In his theory, a 1D array of SCs and atoms can host Majorana fermions (MFs), the most elementary non-Abelian excitations derived from electrons, at the end of the chain. These exotic excitations are topologically protected against any external inhomogeneity, therefore braiding them realizes fault-tolerant operations, and thus, quantum computation [44–47]. Nowadays the proposed system named the Kitaev chain attracts huge attention and has become a central topic of topologial condensed matters.

The main interest of this thesis is the experimental investigation of parallel artificial atoms, namely quantum dots (QDs) coupled to a SC since they compose the basic building block of the Kitaev chain [48]. The interplay between the QDs via the SC is essential to maintain a long-range interaction in the future. Therefore the target of our work is to discover the system in 3 different regimes: the weak and strong QD-SC couplings, and the Coulombic limit of the SC. In the first case, the interaction can be manifested by splitting the entangled electrons of the Cooper pair reservoir and separating them spatially addressed as Cooper pair splitting (CPS). In the second one, the quantum mechanical levels of the QDs can hybridize via the SC, as a strong signature of their interaction. The resulting state is the so-called Andreev molecule, bearing non-local peculiarities analogously to conventional molecules. Structurally, it resembles an H_2 molecule with the differences of the medium being the SC instead of the vacuum, and the hydrogen atoms are replaced with artificial ones. A similar many-body state might arise in the third limit when

a single, isolated electron resides in the SC and the QDs bind to it. This condition is achieved by scaling down the size of the SC and discretizing its energy levels, hence a quasi-particle can exist together with the condensate of Cooper pairs. Remaining at the language of molecules, a H_2O-like object is predicted as an outcome of a 3-particle bond, which we entitle as a polyatomic Andreev molecule. If the phenomena discussed above are thoroughly explored, they can have a huge impact and will bring the community closer to understand the physics of a minimal Kitaev chain.

Materialwise, parallel InAs nanowires connected by an epitaxial Al shell, which became available recently, offer a suitable platform to construct our double QD-SC system. Due to the defect-free SC-semiconductor interface and the two quasi-one-dimensional channels being tightly close by, the interaction of the QDs can be maximized. Other advantageous properties, like the strong spin-orbit interaction, make them a preferable material in all kinds of nanocircuits in later applications.

We build up the thesis in the following way. In Chapter 2, we review the basics of QDs, superconductivity, their combination, and the Kitaev chain model. Without completeness, we explain the most relevant features and perform calculations, mostly in the frame of second quantization. In the same Chapter, we discuss the technical background needed for low-temperature transport experiments in a nutshell. In Chapter 3, we demonstrate CPS experiments in a QD-SC-QD system hosted by parallel InAs nanowires. In the weak coupling limit, we verify a high-efficient pair-splitting signal in the presence of strong electrostatic interaction of the adjacent QDs. In Chapter 4, the formation of an Andreev molecular state is under the scope. We show how 2 subgap states residing in separate QD-SC hybrid couple to each other by analyzing the excitation spectra of the system. We also confirm the existence of the molecule by numerical simulations. In Chapter 5, the development of a 3-particle bound state assisted by a superconducting QD is presented. The general behavior of this extraordinary state is supported by numerical calculations, similarly to the Andreev molecule. Finally, we summarize our findings and the impact of this work imposed in the field.

Chapter 2

Theoretical & technical background

2.1 Quantum dots

QDs (QDs) are artificial islands below the micrometer scale, where movements of the electrons are restricted in all 3 dimensions. The small spatial confinement of a potential well and the Coulomb interaction induce the quantization of the total charge in them, forcing the electrons to discrete energy levels similar to real atoms. This property makes the QDs universal tools [49] to control the transport of the electrons via quantum tunneling and manipulate them individually if their thermal energy is sufficiently suppressed. In practice several types from metal grains to molecules exist, but 2D or close to 1D semiconductors are the most frequently used platforms.

2.1.1 Constant interaction model

The behavior of a QD can be described by an electrostatic model as shown in Fig. 2.1.1**a**. In this picture, the QD grounded via a source and a drain electrode, while it is also shunted capacitively by a plunger gate.

The electron transfer can take place from the source to the drain through the potential barriers with tunnel rates Γ_{S} and Γ_{D}, which serve the confinement itself. However, the QD acts as a capacitor towards the metallic electrodes as shown in Fig. 2.1.1**a**, thus the quantized levels are gate tunable. When the QD is filled with N number of electrons with gate voltage V_{G}, the total energy can be calculated as [50,51]

$$E(N) = \left(\frac{N}{2} - \frac{C_{\mathrm{G}} V_{\mathrm{G}}}{e}\right) NU + \sum_{i=1}^{N} \epsilon_i, \tag{2.1.1}$$

where

$$\begin{aligned} U &= \frac{e^2}{C_\Sigma} \\ C_\Sigma &= C_{\mathrm{S}} + C_{\mathrm{D}} + C_{\mathrm{G}}. \end{aligned} \tag{2.1.2}$$

U is the charging energy and $N = 0$ at $V_{\mathrm{G}} = 0$ is assumed. ϵ_i is the the energy of the ith occupied orbital [52–54] yielding the total kinetic energy of the N electrons. One can show that the energy cost of adding one more electron to the QD is:

$$\Delta E \approx \mu(N+1) - \mu(N) = E(N+1) - E(N) - \big(E(N) - E(N-1)\big) = U + \delta_N, \tag{2.1.3}$$

where μ is the electrochemical potential of the QD and δ_N is the level spacing, the energy difference of the orbitals filled by the $N+1$th and the Nth electrons.

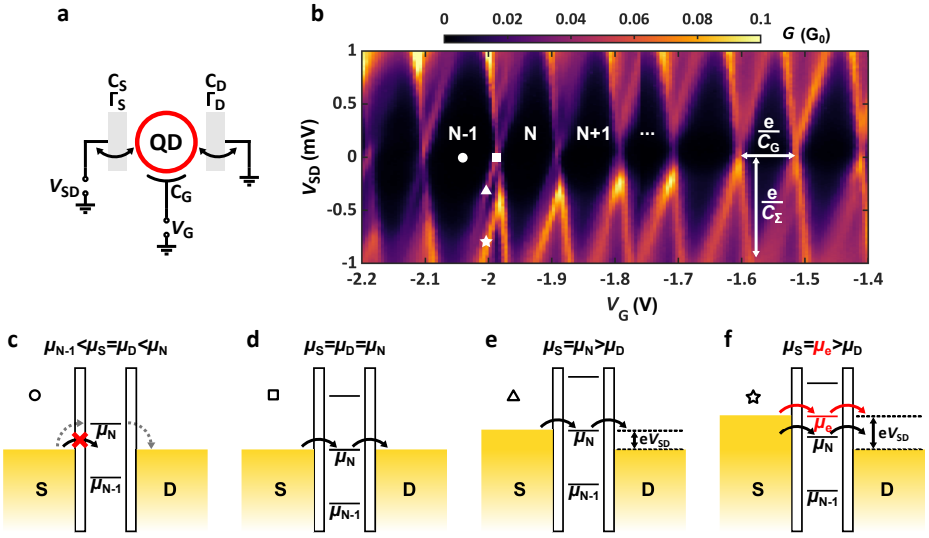

Figure 2.1.1: **Constant interaction model of a QD a** Minimal circuit diagram of a QD tunnel coupled to the source (S) and drain (D) electrode, and capacitively coupled to a gate (G). **b** Finite-bias spectroscopy of a QD as a function of the level position (controlled by V_G) and the source-drain voltage, V_{SD}. The differential conductance measurement, G, yields an array of Coulomb diamonds whose slopes are defined by the capacitive network. **c-f** Diagrams explaining the transport at specific settings in the spectrum from panel **b**. In the middle of the diamonds **c** (circle), tunneling occurs via cotunneling, while **d** the tip of the diamond (square) presents a charge degeneracy with $\mu_S = \mu_N = \mu_D$. This setting provides electron transport from the source to the drain at zero bias. **e** At finite bias the blockade is lifted at smaller V_G, and **f** increasing it further allows another orbital to carry current (star). The measurement of panel **b** was performed by the Author.

Considering the transport mechanism, the excitation spectrum of a QD exhibits the so-called Columb diamond pattern[51,53], such one is demonstrated in Fig. 2.1.1**b**, where the differential conductance, $G = dI/dV_{SD}$ is shown as a function of the plunger gate voltage V_G and the bias voltage V_{SD}. Electron transfer is blocked at zero bias (see the white circle and 2.1.1**c**) and only cotunneling processes are available via virtual states (see the gray dashed arrows) except when one of the energy levels of the QD is aligned to the chemical potential of the source (μ_S) and the drain (μ_D) with V_G (see the white square). In these particular level positions, the states with $N-1$ and N number of electrons are degenerate, $E(N-1) = E(N)$, and the blockade is lifted as illustrated in panel **d**. By applying finite bias voltage to the source, current can flow in a wider range of V_G as the energy level of the QD can be arbitrary in the energy window eV_{SD}. At the white triangle in 2.1.1**b**, $\mu_S = \mu_N$ is maintained allowing the charge transport along a Coulomb diamond edge as shown in panel **e**. We note that the bias also tunes the QD levels due to the finite capacitance to the leads and the spectrum becomes asymmetric since $C_S \neq C_D$ holds in general. One can define the lever arm as the efficiency factor of the gate electrode, $\alpha = C_G/C_\Sigma$. At the star icon in panel **b**, an excitation line parallel to the low-energy diamond edge is observable belonging to the N occupation number, but involving another orbital. It opens an additional conductance channel thereby increasing the current in the system, which is illustrated in panel **f**. From the height and the width of the diamonds, U and C_G can be estimated as shown by the white arrows in panel **b**. The condition $k_BT < U$ must be satisfied to exclude thermally active electrons from the transport. It is also substantial to have tunnel resistances for $R > h/e^2$ to keep the tunneling regime valid.

2.1.2 Anderson model

The main properties of a QD can be captured by a simple model called the Anderson model[55,56]. For simplicity, we assume 2 spin-degenerate quantum mechanical orbitals with dif-

ferent energies on the QD. In the Fock space, the second-quantized Hamiltonian of an isolated QD reads as

$$H_{\mathrm{QD}} = \varepsilon \sum_{\alpha} n_{\alpha} + \left(\sum_{\alpha} n_{\alpha} \right) \left(\sum_{\beta} n_{\beta} - 1 \right) \frac{U}{2} + \sum_{\alpha} n_{\alpha} \epsilon_{\alpha}, \tag{2.1.4}$$

and

$$n_{\alpha} = \sum_{\sigma} d^{\dagger}_{\alpha\sigma} d_{\alpha\sigma}. \tag{2.1.5}$$

Here n_{α} is the particle number operator of orbital α with $d^{(\dagger)}_{\alpha\sigma}$ being the annihilation (creation) operator of an electron in the QD with spin σ, ε is the on-site energy, U is the Coulomb energy, and ϵ_{α} is the energy of orbital α, similarly to 2.1.1. With the basis of total QD electron occupation, which is a good quantum number, H_{QD} is diagonal. The excitations between eigenstates differing in only 1 electron altogether become available in transport measurements. Fig. 2.1.2**a** presents the energy diagram of a single-orbital QD in the Anderson picture[55] as the function of the level position i.e. the gate voltage in experiments. For a single level, the Hamiltonian in Eq. 2.1.4 becomes rather simple as

$$H_{\mathrm{QD}} = \varepsilon \sum_{\sigma} n_{\sigma} + U n_{\uparrow} n_{\downarrow}. \tag{2.1.6}$$

The black line in Fig. 2.1.2**a** corresponds to the ground state, which is the empty QD, $|0\rangle$ for $0 < \varepsilon/U$, the twice degenerate doublet state,$|\uparrow\rangle, |\downarrow\rangle$, for $-1 < \varepsilon/U < 0$ with energy ε, and the double occupied singlet, $|2\rangle$ for $\varepsilon/U < -1$ with energy $2\varepsilon + U$. Taking the energy difference between the ground state and the first excited state (blue) reproduces the Coulomb diamonds, which is illustrated by the dashed gray lines. The red lines correspond to higher energy excitations.

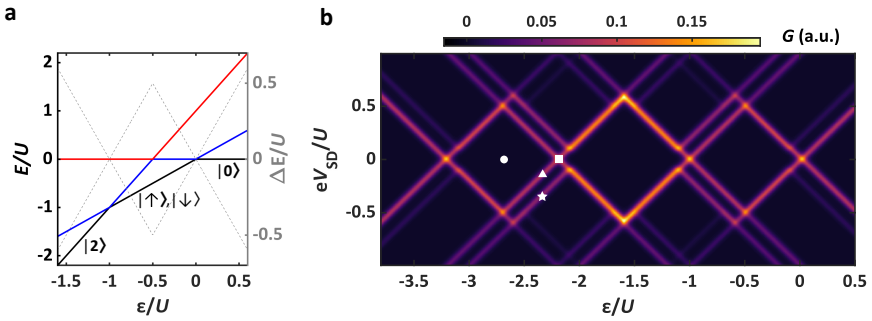

Figure 2.1.2: **Anderson model. a** Energy diagram of the eigenstates of the single-orbital Anderson model. The black line indicates the ground state, while the blue and the red ones (belonging to the left axis in the plot) correspond to the first and second excited states, respectively. The gray dashed line (right axis) shows the energy difference between the black and the blue lines as the lowest possible excitations exhibiting the Coulomb diamonds. **b** Differential conductance through a QD with 2 orbitals in the Anderson picture. The current is calculated with a rate equation model with $\delta/U = 0.2$ level spacing. The symbols belong to the transport processes depicted in Figs.2.1.1**b-f**. The simulation was performed by the Author.

Transport through such a QD coupled to Fermi-seas can also be calculated using a rate equation model[56,57]. By allowing 2 orbitals with a level spacing $\delta/U = 0.2$, one can derive the differential conductance of the system as a function of the level position and the bias as demonstrated in Fig. 2.1.2**b** by solving the classical Master equation. For the details of the calculation, see Appendix A.1. When the QD is complemented with an additional orbital, higher energy excitations like the ones shown in Figs.2.1.1**b** and 2.1.1**f** can be reproduced as well as the Coulomb diamond patterns. We note that the intensity of the lines is determined

by the coupling strengths (Γ) while the sharpness is governed by the finite temperature (T) as lifetime broadening is not included in the model.

2.1.3 Coulomb resonance lineshape

In Figs. 2.1.1**b** and **d-f** we showed when the chemical potential of a QD level is aligned with either μ_S or μ_D, there is no more Coulomb blockade and the QD becomes resonant. Now we discuss how the lineshape evolves around the vicinity of a single-level resonance, i.e. at the white square and triangle in Figs 2.1.1**b** and **d**.

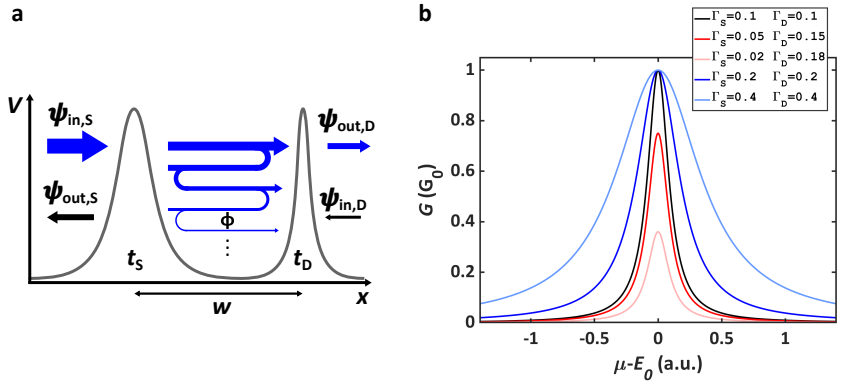

Figure 2.1.3: **Coulomb resonance.** **a** Quantum tunneling through double barriers. The incident electron is transmitted coherently either directly or as a series of reflections between the two barriers while developing a phase shift of Φ. **b** Differential conductance of a resonant tunneling in the Lorentzian approximation as a function of the detuning energy. The more asymmetric the couplings are, the smaller the peak evolves, whereas the higher its total value is, the wider the resonance gets.

The basic problem of the resonant tunneling traces back to the longitudinal transmission of an electron through two scattering centers in series[58–60]. The incident and outcoming wavefunctions on the two sides depicted in Fig. 2.1.3**a** can be described in the frame of the S-matrix formalism[60,61] as

$$\Psi_{\text{out}} = S\Psi_{\text{in}} \tag{2.1.7}$$

with

$$\begin{aligned} \Psi_{\text{in(out)}} &= \begin{pmatrix} \Psi_{\text{in(out),S}} \\ \Psi_{\text{in(out),D}} \end{pmatrix} \\ S &= \begin{pmatrix} r & t' \\ t & r' \end{pmatrix}. \end{aligned} \tag{2.1.8}$$

All elements of the unitary S matrix are the combination of the complex transmission and reflection amplitudes t_S, t_D, r_S, and r_D on the source and drain-side barriers. The transmission probability t of an electron is the sum of individual paths constructed as a sequence of transmissions and reflections on the two barriers as illustrated with the blue arrows in Fig. 2.1.3**a**,

$$t = t_D t_S + t_D r'_S r_D t_S + t_D r'_S r_D r'_S r_D t_S + ..., \tag{2.1.9}$$

which yields

$$t = \frac{t_D t_S}{1 - r'_S r_D}, \tag{2.1.10}$$

since Eq. 2.1.9 is a geometrical series. From Eq. 2.1.10 the total transmission reads as

$$T = |t|^2 = \frac{T_D T_S}{1 + R_S R_D - 2\sqrt{R_S R_D}\cos(\Phi)}. \tag{2.1.11}$$

We used the notation $T_{\mathrm{S(D)}} = |t_{\mathrm{S(D)}}|^2$. $\Phi = \arg(r'_{\mathrm{S}}) + \arg(r_{\mathrm{D}})$ is the phase shift acquired in one round-trip between the scatterers, which depends on the wave number k and the energy E of the electron. For a QD with hardly opaque tunnel barriers the Lorentzian approximation R_S, $R_D \approx 1$ is assumed, therefore 2.1.11 can be expanded as

$$T \approx \frac{T_{\mathrm{D}} T_{\mathrm{S}}}{\left(\frac{T_{\mathrm{D}}+T_{\mathrm{S}}}{2}\right)^2 + 2\left(1-\cos(\Phi)\right)}. \tag{2.1.12}$$

The QD becomes resonant at energy E_0 if $\Phi \approx 2\pi n,\ n \in \mathbb{Z}$, thus Eq. 2.1.12 can be expanded further using

$$1-\cos(\Phi) \approx \frac{1}{2}\left(\Phi - 2\pi n\right)^2 \approx \frac{1}{2}\left(\frac{d\Phi}{dE}\right)^2 \left(E-E_0\right)^2. \tag{2.1.13}$$

The phase shift can be expressed by the wave number k and the distance of the barriers w as $\Phi \approx 2kw$. One can introduce the coupling strengths to the source and drains as

$$\Gamma_{\mathrm{S(D)}} = \frac{dE}{d\Phi} T_{\mathrm{S(D)}} \approx \frac{1}{2w}\frac{dE}{dk} T_{\mathrm{S(D)}} = hf T_{\mathrm{S(D)}}, \tag{2.1.14}$$

since f is interpreted as the frequency the electron bounces back and forth attempting to escape from the QD. By combining Eqs. 2.1.12, 2.1.13 and 2.1.14, the transmission takes the form

$$T = \frac{\Gamma_{\mathrm{S}}\Gamma_{\mathrm{D}}}{\Gamma_{\mathrm{S}}+\Gamma_{\mathrm{D}}} \frac{\Gamma_{\mathrm{S}}+\Gamma_{\mathrm{D}}}{\left(\frac{(\Gamma_{\mathrm{S}}+\Gamma_{\mathrm{D}})}{2}\right)^2 + (E-E_0)^2}, \tag{2.1.15}$$

from which the differential conductance is obtained with the Landauer formalism [61–63] providing the Breit-Wigner formula [64]:

$$G = 2\frac{e^2}{h}\int \left(-\frac{\partial f(E)}{\partial E}\right) T(E) dE \approx 2\frac{e^2}{h}\frac{\Gamma_{\mathrm{S}}\Gamma_{\mathrm{D}}}{\Gamma_{\mathrm{S}}+\Gamma_{\mathrm{D}}} \frac{\Gamma_{\mathrm{S}}+\Gamma_{\mathrm{D}}}{\left(\frac{(\Gamma_{\mathrm{S}}+\Gamma_{\mathrm{D}})}{2}\right)^2 + (\mu-E_0)^2}. \tag{2.1.16}$$

Here f is the Fermi function and we assumed that $\Gamma_{\mathrm{S(D)}} \gg k_{\mathrm{B}}T$, hence the broadening is limited to the finite lifetime only with the

$$\frac{\partial f\left(E\right)}{\partial E} \approx \delta\left(E-\mu\right) \tag{2.1.17}$$

approximation used.

Fig. 2.1.3**b** illustrates the Lorentzian Coulomb resonances as a function of the detuning energy $\mu - E_0$ at different Γ_{S} and Γ_{D} values in $\mu - E_0$ units. The conductance takes its maximum, $G = G_0$, if the source-drain couplings are symmetric, e.g. in case of the black curve, and it decreases by increasing the asymmetry (see the red and pink curves with $\Gamma_{\mathrm{S}}/\Gamma_{\mathrm{D}} = 1/3$ and $\Gamma_{\mathrm{S}}/\Gamma_{\mathrm{D}} = 1/9$, respectively). The full width at half maximum is given by $\Gamma_{\mathrm{S}} + \Gamma_{\mathrm{D}}$ characterizing the lifetime broadening of the QD resonance (see the blue curves where the symmetric coupling is maintained).

2.1.4 Double quantum dots

QDs can be connected either in series or parallel similarly to classical resistors. In the following Chapters, we discuss measurements performed in double QD systems, therefore the most important features are reviewed here.

Fig. 2.1.4**a** depicts schematics of a circuit consisting of two QDs (red, labeled by A, and green,

labeled by B) in series. Compared to a single QD case introduced in Fig. 2.1.1**a** the red and green QDs are not only coupled to the source and the drain with $C_\mathrm{S}, \Gamma_\mathrm{S}$ and $C_\mathrm{D}, \Gamma_\mathrm{D}$, respectively, but they have a mutual capacitance C_M and inter-dot tunnel rate t as well[65]. Furthermore, the QD level positions are governed by their plunger gates, V_A and V_B. Nonetheless, the cross capacitance of V_A to ε_B and vice versa is not negligible and leads to a finite tunability of both QDs by either gate.

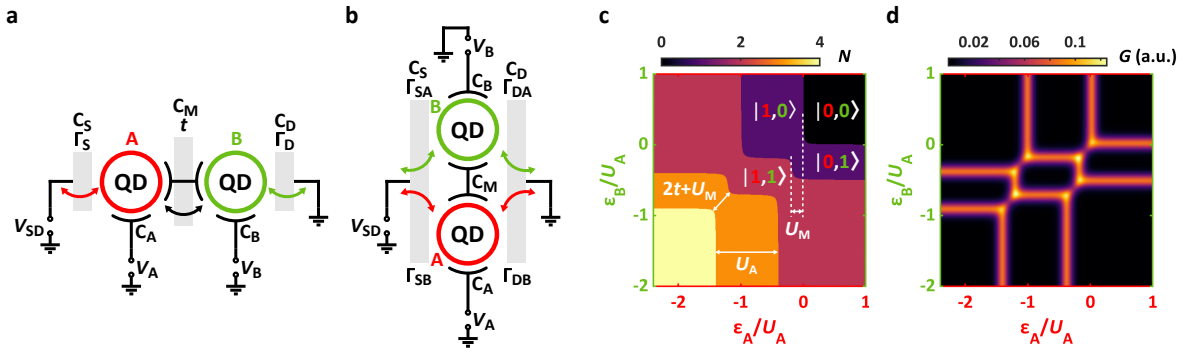

Figure 2.1.4: **Constant interaction model of double QDs.** **a** Circuit diagram of double QDs in series and **b** parallel. The circuits differ resistively, but capacitively are almost equivalent. **c** total ground state charge, N, vs $\varepsilon_\mathrm{A}/U_\mathrm{A}$ and $\varepsilon_\mathrm{B}/U_\mathrm{A}$ map for double QDs in series. $U_\mathrm{M}/U_\mathrm{A(B)}$, and $t/u_\mathrm{A(B)}$ are read off from the shift of the charge degeneracies and the curvature of them around the triple points. **d** Simulated differential conductance G diagram of panel **c**, but for parallel double QDs ($t = 0$). The current is enhanced in the triple points as both QDs get close to their resonances. The simulations were performed by the Author.

Another possibility is to connect the two QDs in parallel which is shown in Fig. 2.1.4**b**. Here direct tunneling between the QDs is excluded whereas they are coupled to the source and the drain. In the constant interaction picture[65], where the energy depends on the total charges on the capacitors, the two systems are equivalent. The Anderson Hamiltonian of such a double QD network[55,66] is written as

$$H_\mathrm{DQD} = \sum_{\alpha=\mathrm{A,B}} \left(\varepsilon_\alpha n_\alpha + n_\alpha \left(n_\alpha - 1 \right) \frac{U_\alpha}{2} \right) + U_\mathrm{M} n_\mathrm{A} n_\mathrm{B} + t \left(\sum_\sigma d^\dagger_{\mathrm{A}\sigma} d_{\mathrm{B}\sigma} + d^\dagger_{\mathrm{B}\sigma} d_{\mathrm{A}\sigma} \right), \quad (2.1.18)$$

where $U_\mathrm{A(B)}$ is the charging energy of QD A(B) and U_M is the inter-dot Coulomb energy:

$$\begin{aligned} U_\mathrm{A(B)} &= \frac{e^2}{C_{\Sigma\mathrm{A(B)}}} \left(\frac{1}{1 - \frac{C_\mathrm{M}^2}{C_{\Sigma\mathrm{A}} C_{\Sigma\mathrm{B}}}} \right) \\ U_\mathrm{M} &= \frac{e^2}{C_\mathrm{M}} \left(\frac{1}{\frac{C_{\Sigma\mathrm{A}} C_{\Sigma\mathrm{B}}}{C_\mathrm{M}^2} - 1} \right). \end{aligned} \quad (2.1.19)$$

For serial connection of the QDs (Fig. 2.1.4**a**), $C_{\Sigma\mathrm{A(B)}} = C_\mathrm{A(B)} + C_\mathrm{S(D)} + C_\mathrm{M}$, for parallel arrangement (Fig. 2.1.4**b**), $C_{\Sigma\mathrm{A(B)}} = C_\mathrm{A(B)} + C_\mathrm{S} + C_\mathrm{D} + C_\mathrm{M}$ total capacitances are taken. In the latter case, $t = 0$ is assumed. The ground state QD occupations can be derived by the direct diagonalization of Eq. 2.1.18 and the calculation of $\langle \Psi_\mathrm{GS} | n_\mathrm{A} + n_\mathrm{B} | \Psi_\mathrm{GS} \rangle$ expectation value, which is demonstrated in Fig. 2.1.4**c** (N) as a function of the on-site energies ε_A and ε_B normalized with U_A. Here we considered double QDs in series with $U_\mathrm{A} = 1$ (as a reference), $U_\mathrm{B} = 0.5$, $U_\mathrm{M} = 0.2$

and $t = 0.04$. The stability diagram takes the form of a honeycomb pattern, where the different sectors correspond to different ground state fillings noted by $|m,n\rangle = |m\rangle_{\mathrm{A}} \otimes |n\rangle_{\mathrm{B}}$. With $U_{\mathrm{M}} \to 0$ the crossings of the red and green QD phase boundaries define four-fold degenerate quadruple points, which split into pairs of three-fold degenerate triple points as U_{M} becomes finite. This feature stems from the QD A (B) being sensitive to the charging of QD B (A). Hence loading (or emptying) one of the QDs effectively gates the other one shifting its charge degeneracies by $-U_{\mathrm{M}}$. This gating effect is visible e.g. between the $|0,0\rangle \longleftrightarrow |1,0\rangle$ and $|0,1\rangle \longleftrightarrow |1,1\rangle$ transitions. The charge degeneracy is located at $\varepsilon_{\mathrm{A}}/U_{\mathrm{A}} = 0$ if $n_{\mathrm{B}} = 0$, however, it is displaced to $\varepsilon_{\mathrm{A}}/U_{\mathrm{A}} = -U_{\mathrm{M}}/U_{\mathrm{A}} = -0.2$. The same amount of shift arises along in ε_{B}. The separation of the triple points increases further with finite t and equals to $2t + U_{\mathrm{M}}$ as indicated in Fig. 2.1.4.

With the application of the same rate equation model used for a single QD in Fig. 2.1.2**b**, zero-bias transport through double QDs coupled to metallic leads can be simulated as a function of ε_{A} and ε_{B}. Such calculated stability map of parallel, isolated QDs ($t = 0$) is shown in Fig. 2.1.4**d**. Finite conductance G is obtained if one of the QDs is resonant, in accordance with the phase diagram of panel **c**, and it is enhanced in the triple points. For the details of the calculation see Appendix A.1.

2.2 Basics of superconductivity

SCs have two typical, phenomenological properties in general. One is the zero electrical resistance, and the other one is the Meissner effect meaning that the SC behaves as a perfect diamagnet by expelling the magnetic field out of the material. These effects can be explained by the phenomenological London model[67,68]. The first microscopic model describing the superconducting condensate properly was the Bardeen-Cooper-Schrieffer (BCS) theory[69,70], which we briefly discuss below.

2.2.1 Bardeen-Cooper-Schrieffer theory

One of the assumptions of BCS theory is the existence of a weak, phonons-induced attractive interaction between two electrons contributing to the formation of Cooper pairs with opposite spin and momentum, which are fully entangled. The ground state of this system can be described as

$$|\Psi_{\mathrm{GS}}\rangle = \prod_{\mathbf{k}} \left(u_{\mathbf{k}} + v_{\mathbf{k}} c^{\dagger}_{\mathbf{k}\uparrow} c^{\dagger}_{\text{-}\mathbf{k}\downarrow} \right) |0\rangle, \tag{2.2.1}$$

where

$$|u_{\mathbf{k}}|^2 + |v_{\mathbf{k}}|^2 = 1. \tag{2.2.2}$$

Here $u_{\mathbf{k}}$ and $v_{\mathbf{k}}$ express the probability of the states $\mathbf{k}\uparrow$, $\text{-}\mathbf{k}\downarrow$ being empty or occupied by a Cooper pair. The Hamiltonian of the superconducting phase can be written with the second quantized formalism as

$$H = H_{\mathrm{kin}} + H_{\mathrm{pot}} = \sum_{\mathbf{k},\sigma} \epsilon_{\mathbf{k}} c^{\dagger}_{\mathbf{k}\sigma} c_{\mathbf{k}\sigma} + \sum_{\mathbf{k},\mathbf{k'}} V_{\mathbf{k}\mathbf{k}'} c^{\dagger}_{\mathbf{k}\uparrow} c^{\dagger}_{\text{-}\mathbf{k}\downarrow} c_{\text{-}\mathbf{k}'\downarrow} c_{\mathbf{k}'\uparrow}. \tag{2.2.3}$$

The four fermionic operator (interaction) term considers the scatterings of the Cooper pairs, while pair splitting processes are neglected. The minimal energy of the condensate can be obtained by taking the variation of the free energy in a grand-canonical ensemble

$$\delta \langle \Psi_G | H - \mu N | \Psi_G \rangle = \delta \left(2 \sum_{\mathbf{k}} \xi_{\mathbf{k}} |v_{\mathbf{k}}|^2 + \sum_{\mathbf{k},\mathbf{k'}} V_{\mathbf{k}\mathbf{k}'} u_{\mathbf{k}} v^{*}_{\mathbf{k}} u^{*}_{\mathbf{k}'} v_{\mathbf{k}'} \right) = 0, \tag{2.2.4}$$

where μ is the chemical potential and the identities

$$\begin{aligned} \langle N \rangle &= \left\langle \sum_{\mathbf{k},\sigma} c^{\dagger}_{\mathbf{k}\sigma} c_{\mathbf{k}\sigma} \right\rangle = 2 \sum_{\mathbf{k}} |v_{\mathbf{k}}|^2 \\ \xi_{\mathbf{k}} &= \epsilon_{\mathbf{k}} - \mu \end{aligned} \tag{2.2.5}$$

were used. One can calculate Eq. 2.2.4 regarding to $u_{\mathbf{k}}$ and $v_{\mathbf{k}}$ and derive the formula

$$\Delta_{\mathbf{k}} = -\frac{\sum_{\mathbf{k}'} \Delta_{\mathbf{k}'} V_{\mathbf{k}\mathbf{k}'}}{2E_{\mathbf{k}}}, \tag{2.2.6}$$

where

$$\begin{aligned} \Delta_{\mathbf{k}} &= -\sum_{\mathbf{k}'} V_{\mathbf{k}\mathbf{k}'} u_{\mathbf{k}'} v_{\mathbf{k}'} \\ E_{\mathbf{k}} &= \sqrt{\Delta^2_{\mathbf{k}} + \xi^2_{\mathbf{k}}}. \end{aligned} \tag{2.2.7}$$

Eq. 2.2.6 is the so-called gap equation, which has a non-trivial solution with the values

$$\Delta_{\mathbf{k}} = \begin{Bmatrix} \Delta, & \text{if } |\xi_{\mathbf{k}}| < E_c \\ 0, & \text{otherwise} \end{Bmatrix}, \tag{2.2.8}$$

and

$$V_{\mathbf{k}} = \begin{Bmatrix} -|V|, & \text{if } |\xi_{\mathbf{k}}| < E_c \\ 0, & \text{otherwise} \end{Bmatrix}. \tag{2.2.9}$$

$E_c = \hbar\omega_{\mathrm{D}}$ is the cut-off energy window defined by the Debye frequency within the attractive interaction is assumed. Putting Eqs. 2.2.6 and 2.2.8 together

$$\Delta = \frac{2\hbar\omega_{\mathrm{D}}}{\mathrm{sh}\left(\frac{2}{V\rho_{\mathrm{N}}(0)}\right)} \tag{2.2.10}$$

is given with $\rho_{\mathrm{N}}(0)$ being the normal density of states (DOS) at the Fermi level.

In the BCS theory, Δ is the order parameter that directly appears in the energy spectrum of the quasi-particles. In practice, it can be considered as the binding energy of the Cooper pair. By knowing the result Eq. 2.2.8, the effective mean-field Hamiltonian can be constructed from Eq. 2.2.3

$$H = \sum_{\mathbf{k},\sigma} \xi_{\mathbf{k}} c^{\dagger}_{\mathbf{k}\sigma} c_{\mathbf{k}\sigma} + \sum_{\mathbf{k}} \left(\Delta c^{\dagger}_{\mathbf{k}\uparrow} c^{\dagger}_{\text{-}\mathbf{k}\downarrow} + \Delta^* c_{\text{-}\mathbf{k}\downarrow} c_{\mathbf{k}\uparrow} \right), \tag{2.2.11}$$

with

$$\Delta = V \langle c_{\text{-}\mathbf{k}\downarrow} c_{\mathbf{k}\uparrow} \rangle. \tag{2.2.12}$$

Regarding the transport properties, the DOS in the SC can be calculated by its definition and concerning the excitation energy from Eq. 2.2.7

$$\rho(E) = \frac{1}{(2\pi)^3} \int_{S_{E'}} \frac{dS}{|\nabla_{\mathbf{k}} E_{\mathbf{k}}|} = \frac{\partial \xi_{\mathbf{k}}}{\partial E} \frac{1}{(2\pi)^3} \int_{S_{E'}} \frac{dS}{|\nabla_{\mathbf{k}} \xi_{\mathbf{k}}|} = \begin{Bmatrix} \rho_{\mathrm{N}}(0) \frac{E}{\sqrt{E^2 - \Delta^2}}, & \text{if } E > \Delta \\ 0, & \text{otherwise} \end{Bmatrix}. \tag{2.2.13}$$

In a SC-insulator-normal metal (SC-I-N) junction, the DOS can be estimated since it is proportional to the differential conductance. When the junction is biased by $|eV_{\mathrm{SD}}| > \Delta$ the current

is obtained from the tunnel formula[61–63]

$$I = A|T|^2\rho_{\mathrm{N}}(0)\int_{-\infty}^{\infty}\rho(E)\left(f(E) - f(E + eV_{\mathrm{SD}})\right)dE, \tag{2.2.14}$$

where T is the transmission ($|T| \ll 1$) and A is a constant. Assuming ultra low temperature ($k_{\mathrm{B}}T \longrightarrow 0$):

$$-\frac{\partial f\left(E + eV_{\mathrm{SD}}\right)}{\partial\left(eV_{\mathrm{SD}}\right)} \approx \delta\left(E + eV_{\mathrm{SD}}\right), \tag{2.2.15}$$

from which the differential conductance is

$$G = \frac{dI}{dV_{\mathrm{SD}}} = G_{\mathrm{N}}\frac{\rho(eV_{\mathrm{SD}})}{\rho_{\mathrm{N}}(0)}, \tag{2.2.16}$$

where G_{N} is the conductance of a normal metal-insulator-normal metal junction. In the next subsections, N-SC junctions are under the scope.

2.2.2 Local Andreev reflection

The transport mechanism of a SC-normal metal interface can be described in the frame of local Andreev reflection (LAR)[71]. In this process, an electron with spin σ is transmitted to the SC if its energy is smaller than the superconducting gap ($|E| < \Delta$), and a hole with spin $\overline{\sigma}$ is reflected yielding $2e$ charge transfer as a Cooper pair in net as illustrated in Fig. 2.2.1**a**. To understand the physics behind the LAR, one can consider the electron-hole description of superconductivity with the Bogoliubov de Gennes equations[72,73], where the wave function inside the material can be described by a 2 component vector, $\Psi_{\mathbf{k}0}$, which contains the electron and hole amplitudes. Due to the electron-hole pairing (with different spins and momentum), gaps with 2Δ are opened at the Fermi wavenumber (k_{F}) as depicted in Fig. 2.2.1**b**.

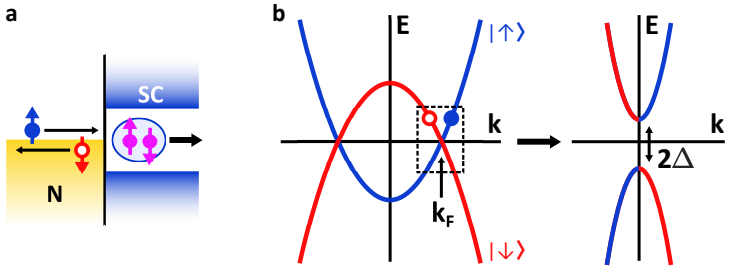

Figure 2.2.1: **Andreev reflection and electron-hole pairing in SCs. a** LAR on a normal metal-SC interfface. In the electron-hole language, an electron (blue) is injected and a hole (red) is reflected constituting a transmitted Cooper pair. **b** Dispersion relation in the electron-hole interpretation. At the crossing of the dispersions at the Fermi level, the electron-hole interaction induces a band gap of 2Δ.

The Hamiltonian in a SC can be written in a two by two matrix:

$$\begin{pmatrix} H_N & \Delta \\ \Delta^* & -H_N \end{pmatrix}\Psi_{\mathbf{k}0} = E\Psi_{\mathbf{k}0}, \tag{2.2.17}$$

where:

$$\begin{aligned} \Psi_{\mathbf{k}0} &= \begin{pmatrix} u \\ v \end{pmatrix} \\ H_N &= \frac{p^2}{2m^*} - \mu \\ \Delta &= |\Delta|e^{i\phi}. \end{aligned} \tag{2.2.18}$$

The solution for E is equivalent to the one in Eq. 2.2.7:

$$E = \sqrt{\left(\frac{\hbar^2 k^2}{2m^*} - \mu\right)^2 \pm |\Delta|^2}. \tag{2.2.19}$$

Considering the eigenvectors, the ratio of v and u when $|E| < |\Delta|$:

$$\frac{v_{e(h)}}{u_{e(h)}} = \frac{E \mp \mathrm{sgn}(E) i\sqrt{|\Delta|^2 - E^2}}{|\Delta| e^{i\phi}}. \tag{2.2.20}$$

The indices e and h refer to the electrons and holes. We note that the $\Delta = 0$ limit describes a normal metal yielding independent electron and hole components. To calculate the amplitude of the LAR for $|E| < |\Delta|$, the Bogoliubov de Gennes equations of a SC-normal metal (SC-N) junction with perfect transmittance on the interface have to be solved. To determine the r_A reflection amplitude parameter, the boundary conditions of the problem must be satisfied. It denotes matching the wave functions and their derivatives on the interface. Simplifying the situation to 1D:

$$\begin{aligned} \Psi_N(0) &= \Psi_S(0) \\ \frac{\partial \Psi_N(0)}{\partial x} &= \frac{\partial \Psi_S(0)}{\partial x}, \end{aligned} \tag{2.2.21}$$

where Ψ_N is the wave function of the normal metal involving the incident electron, the reflected electron, and the reflected hole, while Ψ_S consists of transmitted electron and hole-like quasiparticles:

$$\begin{aligned} \Psi_N(x) &= \begin{pmatrix} 1 \\ 0 \end{pmatrix} e^{ikx} + r_e \begin{pmatrix} 1 \\ 0 \end{pmatrix} e^{-ikx} + r_\mathrm{A} \begin{pmatrix} 0 \\ 1 \end{pmatrix} e^{ikx} \\ \Psi_S(x) &= t_e \begin{pmatrix} u_e \\ v_e \end{pmatrix} e^{ikx} + t_h \begin{pmatrix} u_h \\ v_h \end{pmatrix} e^{-ikx}. \end{aligned} \tag{2.2.22}$$

Here the Andreev approximation was used, namely $\Delta \ll \mu$ and $k_e(x) \approx k_h(x) = k$. r_e, t_e correspond to electron reflection and transmission amplitudes, t_h equals to the hole reflection, respectively. As the calculation is derived by assuming perfect transmittance on the interface, r_A is obtained as:

$$r_\mathrm{A} = \frac{v_e}{u_e} = \frac{E - \mathrm{sgn}(E) i\sqrt{|\Delta|^2 - E^2}}{|\Delta| e^{i\phi}} = (\cos\omega - i\sin\omega)\, e^{-i\phi}, \tag{2.2.23}$$

where:

$$\begin{aligned} \cos\omega &= \frac{|E|}{|\Delta|} \\ \sin\omega &= \frac{\sqrt{|\Delta|^2 - E^2}}{|\Delta|}. \end{aligned} \tag{2.2.24}$$

The result leads to:

$$\begin{aligned} |r_\mathrm{A}| &= 1 \\ \arg(r_\mathrm{A}) &= -\arccos\left(\frac{E}{|\Delta|}\right) - \phi. \end{aligned} \tag{2.2.25}$$

Consequently, all electrons with energy $|E| < |\Delta|$ Andreev reflects with the given phase.

As the hole originating from the Andreev reflection takes the time-reversed path in the normal conductor, locally, Cooper pairs are injected. This mechanism leads to the appearance of superconducting properties in the normal material too, which is called proximity effect [71,74].

Although the superconducting correlations are found close to the interface, the decoherence coming from the phase difference of the hole and the electron results in the suppression of the feature. The characteristic length where the proximity effect is observable measured from the interface is given by the coherence length.

2.2.3 Crossed Andreev reflection & Cooper pair splitting

In the previous subsection, we briefly discussed the physics of LAR, where two incident electrons were transmitted from a normal lead to the SC. Now we focus on a process where the electrons recombining as a Cooper pair in the SC originate from separate electrodes. Considering a 3-terminal junction of Fig. 2.2.2**a**, if electron enters the SC from one of the normal electrodes, an Andreev reflected hole can leave to the other one with opposite spin and momentum. One can also define its time-reversed event, when the binding of the entangled electrons is broken and they are enforced to different normal electrodes realizing their spatial separation. The previous phenomenon is called crossed Andreev reflection (CAR), the latter one is the Cooper pair splitting (CPS)[75–78]. The signature of CAR and CPS have been reported first in such metallic junctions as the one in Fig. 2.2.2**a**[79–81].

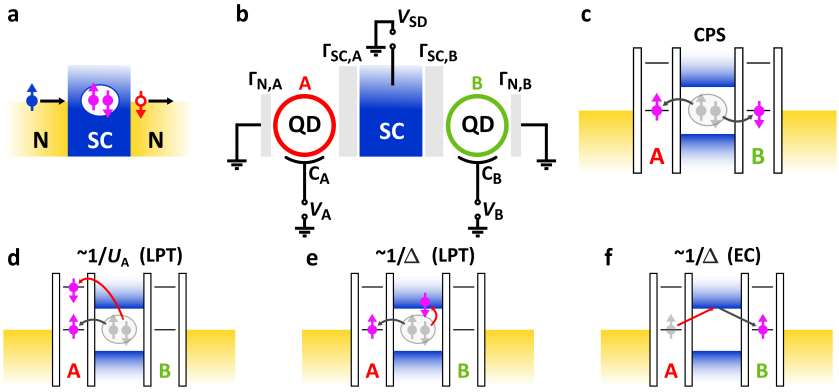

Figure 2.2.2: **Concept of CAR and CPS. a** 3-terminal device of a normal metal-SC-normal metal (N-SC-N) junction. The incident electron from the left electrode reflects as a hole in the right arm resulting in CAR. **b** Sketch of a CPS circuit with QDs A and B in parallel. $\Gamma_{\mathrm{SC,A(B)}} > \Gamma_{\mathrm{N,A(B)}}$ is preffered to gain high efficiency. **c-f** Energy diagram of CPS, LPT, and EC with resonant QD levels. The CPS can dominate since LPT and EC are suppressed by either $1/U_{\mathrm{A(B)}}$ or $1/\Delta$ (the energetically unfavorable process is depicted with the red arrows).

To obtain a sufficient CAR or CPS, one has to suppress other local processes like the LAR, which we call now local pair tunneling (LPT), or elastic cotunneling (EC), when a single charge is from one electrode goes to the other via the SC[82,83]. An efficient way to make CAR and CPS dominant is to introduce QDs at the SC-normal metal interfaces, as shown in Figs. 2.2.2**b-c**. Due to the Coulomb blockade, the double charging as an intermediate state in the QD penalizes the LPT by $1/U$, while the creation of a quasi-particle in the SC is quenched by $1/\Delta$, as illustrated in Figs. 2.2.2**d-e**. The latter also decreases the probability of the EC, which is shown in Fig. 2.2.2**f**. CPS has intensively researched in several platforms utilizing parallel double QDs hosted in them, e.g. in single wire devices[84–89], or graphene-based junctions[90–93].

In Ref. 82 CPS has been analyzed quantitaviely with a transmission matrix approach. The CPS and LPT currents were calculated based on transition rates between different initial and final states (with the tunnelings treated perturbatively), which were derived by applying Fermi's golden rule[94]. The CPS current contribution of electrons tunneling into separate QDs (like A

and B in Figs. 2.2.2**b-c**) was found to be

$$I_{\mathrm{CPS}} = \frac{e\Gamma_{\mathrm{SC,A}}\Gamma_{\mathrm{SC,B}}\left(\Gamma_{\mathrm{N,A}}+\Gamma_{\mathrm{N,B}}\right)}{\left(\varepsilon_{\mathrm{A}}+\varepsilon_{\mathrm{B}}\right)^2+\left(\frac{\Gamma_{\mathrm{N,A}}+\Gamma_{\mathrm{N,B}}}{2}\right)^2}\left(\frac{\sin\left(k_{\mathrm{F}}\delta r\right)}{k_{\mathrm{F}}\delta r}\right)^2 e^{-2\delta r/\pi\xi}, \tag{2.2.26}$$

while electron tunneling to the same QD A(B) providing the LPT contribution is

$$I_{\mathrm{LPT,A(B)}} = 2e\Gamma^2_{\mathrm{SC,A(B)}}\Gamma_{\mathrm{N,A(B)}}\left(\frac{1}{\pi\Delta}+\frac{1}{U_{\mathrm{A(B)}}}\right)^2, \tag{2.2.27}$$

valid in ballistic 3D SCs. Here $\Gamma_{\mathrm{SC,A(B)}}$, $\Gamma_{\mathrm{N,A(B)}}$ is the coupling of QD A(B) to the SC and the normal leads, respectively, $\varepsilon_{\mathrm{A(B)}}$ is the on-site energy of QD A(B), ξ is the superconducting coherence length, k_{F} is the Fermi wavenumber, and δr is the distance between the points where the electrons exit from the SC to the QDs.

The ideal parameter range of QD-based Cooper pair splitters is defined by $U_{\mathrm{A(B)}}, \Delta, \epsilon_{\mathrm{A(B)}} > \Gamma_{\mathrm{SC(N),A(B)}}, k_{\mathrm{B}}T$ and $\Gamma_{\mathrm{SC,A(B)}} < \Gamma_{\mathrm{N,A(B)}}$ inequalities[82,95]. The role of a large $U_{\mathrm{A(B)}}$ and Δ is to suppress local processes (see Figs. 2.2.2**d-f**) and their thermal excitations. $\epsilon_{\mathrm{A(B)}}$ is the level spacing of QD A(B), which is necessary to distinguish the electron just split from other ones residing in the QD. Otherwise, the loss of the entanglement is not prevented as the QD acts as a metallic capacitor, from which any of the electrons can tunnel out while the QD is resonant. Intuitively, a strong $\Gamma_{\mathrm{N,A(B)}}$ is required to empty the QDs once the electrons enter them from the SC not to block the transport.

As visible, I_{CPS} is a product of 3 different factors. The first one is a Breit-Wigner factor encompassing the level positions of the QDs. It is maximal at $\varepsilon_{\mathrm{A}} = -\varepsilon_{\mathrm{B}}$, as expected from the conservation of energy. The second one is a geometrical factor expressing a strong spatial decay in with $\sim 1/\delta r^2$. Other theoretical works and experiments accomplished in nanowires of close-to-1D systems, where the SC proximitized the material, found that this geometrical suppression vanishes and goes to 1 thereby enhancing the perceptibility of CPS. The third factor expresses an exponential decay of the current in δr scaled by ξ, which is attributed to the loss of coherence. The efficiency of the CPS is defined as

$$s = \frac{2I_{\mathrm{CPS}}}{\left(I_{\mathrm{A}}+I_{\mathrm{B}}\right)} = \frac{2\Delta G}{\left(G_{\mathrm{A}}+G_{\mathrm{B}}\right)}, \tag{2.2.28}$$

whereas its visibility in QD A(B) is

$$\eta_{\mathrm{A(B)}} = \frac{I_{\mathrm{CPS}}}{I_{\mathrm{A(B)}}} = \frac{\Delta G}{G_{\mathrm{A(B)}}}. \tag{2.2.29}$$

Here $I_{\mathrm{A(B)}}$, $G_{\mathrm{A(B)}}$, and ΔG are the total current flowing through QDs A and B, the total zero-bias conductance, and the conductance coming from CPS, respectively[84,87,96,97]. The exponential decay of I_{CPS}, and thus, s recommends the reduction of δr[82,98]. However, as the distance between the QDs is diminished, the inter-dot Coulomb energy U_{M} becomes considerable as introduced in Fig. 2.1.4 and in Eq. 2.1.19 suppressing any CAR-related processes. In Chapter 3, we demonstrate high-efficient CPS experiments carried out in parallel InAs nanowires, where the impacts of U_{M} and the loss of coherence in δr on s are addressed.

2.2.4 Andreev bound states (scattering matrix approach)

The BCS theory predicts zero DOS inside the gap of a SC as derived in Subsection 2.2.1. Even so, when a normal condcutor is attached to the SC, it gets proximitized and discrete

spectra carrying superconducting current can still exist, which are called Andreev bound states (ABSs). There are two different concepts in which the ABSs can be interpreted. The one that we discuss first is a SC-normal metal-SC (SC-N-SC) junction with a barrier inside the normal region.

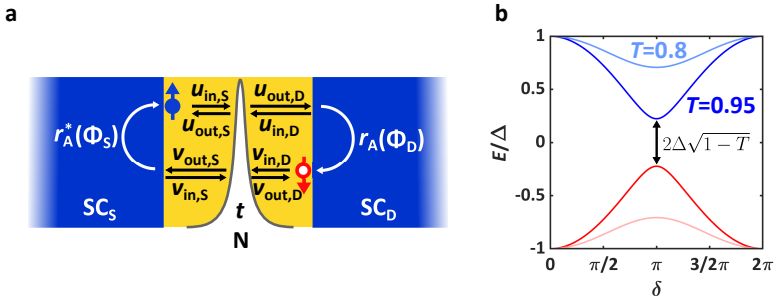

Figure 2.2.3: **ABSs in a SC-N-SC junction.** **a** Illustration of electron (hole) propagation forming an ABS. The sequence of scatterings and LARs enclose a resonant loop expressed by the $u(v)_{\mathrm{in(out),S(D)}}$ amplitudes and $\Phi_{\mathrm{S(D)}}$ superconducting phases. **b** ABS energy vs the superconducting phase difference with different transmission rates. The energy is minimal at π phase. Since the odd state has zero energy, $\Delta E = E$ for single electron excitation holds.

Let us consider a single-channel SC-N-SC junction with a symmetric tunnel barrier of transmission t as depicted in Fig. 2.2.3**a**. An incident electron propagating from the source ($u_{\mathrm{in,S}}$) is scattered according to the S-matrix formalism[60,61] already introduced at Eq. 2.1.8:

$$\begin{pmatrix} u_{\mathrm{out,S}} \\ u_{\mathrm{out,D}} \end{pmatrix} = \underbrace{\begin{pmatrix} r & t \\ t & r \end{pmatrix}}_{S} \begin{pmatrix} u_{\mathrm{in,S}} \\ u_{\mathrm{in,D}} \end{pmatrix}. \tag{2.2.30}$$

The transmitted part in the drain side $u_{\mathrm{out,D}}$ can Andreev reflect as a hole from the second SC with amplitude $r_{\mathrm{A}}(\Phi_{\mathrm{S}})$ derived in Eq. 2.2.25:

$$\begin{pmatrix} v_{\mathrm{in,D}} \\ u_{\mathrm{in,D}} \end{pmatrix} = \underbrace{\begin{pmatrix} r_{\mathrm{A}}(\Phi_{\mathrm{S}}) & 0 \\ 0 & r_{\mathrm{A}}(-\Phi_{\mathrm{S}}) \end{pmatrix}}_{A} \begin{pmatrix} u_{\mathrm{out,D}} \\ v_{\mathrm{out,D}} \end{pmatrix}. \tag{2.2.31}$$

The reflected hole $v_{\mathrm{in,D}}$ travels backward compared to the electron and scatters on the tunnel barrier with S^* from Eq. 2.2.30, and the loop is closed by the hole Andreev reflecting on the source side SC with $r_{\mathrm{A}}^*(\Phi_{\mathrm{D}})$. A resonant standing wave mode with energy $E < |\Delta|$ can form in case of constructive interference by the forth and backscatters, which we call an ABS. The sequence of scatterings is a product of normal and Andreev reflections

$$\begin{pmatrix} u_{\mathrm{in,S}} \\ u_{\mathrm{in,D}} \end{pmatrix} = A^* S^* A S \begin{pmatrix} u_{\mathrm{in,S}} \\ u_{\mathrm{in,D}} \end{pmatrix}, \tag{2.2.32}$$

from which the constructive interference condition is

$$\det(A^* S^* A S - 1) = 0, \tag{2.2.33}$$

yielding the energy-phase relation of the ABS

$$E = \pm|\Delta|\sqrt{1 - T\sin^2(\delta/2)}, \tag{2.2.34}$$

where $\delta = \Phi_D - \Phi_S$, $T = |t^2|$ notations and $k_e \approx k_h$ approximation were used.

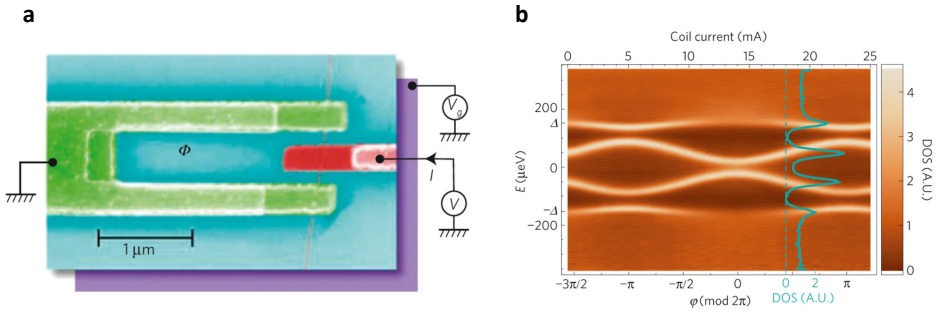

Figure 2.2.4: **Direct spectroscopy of ABSs in a SC-N-SC junction.** **a** False-colored scanning electron microscopy (SEM) image of a carbon nanotube embedded in a superconducting loop. The magnetic flux threading the loop tunes the superconducting phase difference, $\Phi \equiv \delta$. A normal lead is attached to the tube as a tunnel probe. **b** Extracted DOS from bias spectroscopy measurement via the tunnel probe. The development of the ABS energy with Φ from Fig. 2.2.3**b** is reproduced. Adapted from Ref. 99.

Fig. 2.2.3**b** demonstrates the result Eq. 2.2.34 for $T = 0.8$ (pink and light blue) and $T = 0.95$ (red and dark blue) transmission values. In the even parity ground state, the ABS with $E < 0$ is filled and the $E > 0$ one is empty with their minimal separation of $2\Delta\sqrt{1-T}$. The odd parity state of the system with $E_o = 0$ is attained by removing an electron from the negative energy ABS or adding an electron to the positive energy one with $\Delta E = E - E_o = E$. Performing the two excitations simultaneously preserves the electron number, and thus, the even parity. This anharmonic two-level system of the even sector is the basic concept of Andreev qubits, where the transition is driven by the microwave pulses with energy $2E$[28–31].

There are multiple methods to capture the direct ABS experimentally. Exploring the ABS spectrum via coupling the Andreev level current to a resonator inductively[100], recording the inelastic Cooper pair tunneling induced by photon absorption of an on-chip radiation[29], or direct spectroscopy of a tunnel probe are found among the literature[99,101]. One example of the latter one is shown in Fig. 2.2.4 adapted from Ref. 99. In that work, a carbon nanotube was forked in a superconducting loop with a normal lead attached to the middle of the tube (see panel **a**) to probe the DOS. The superconducting phase difference, $\Phi \equiv \delta$ with the notation of the Authors, was tuned by the magnetic flux penetrating the loop. The energy of the ABS was discovered by biasing the tunnel probe as a function of Φ. The spectrum with the extracted DOS is shown in Fig. 2.2.4**b** encountering the theory from Fig. 2.2.3**b**.

2.2.5 Andreev bound states & Yu-Shiba-Rusinov states in quantum dots

In the previous Subsection, we examined sub-gap states residing in a single conductance channel biased by the superconducting phase difference between the source and the drain, δ. Another origin of ABSs is the hybridization of a QD level with the bulk SC[57,99,102–115]. There are commonly used schemes to describe the formation of these states: the two simplest of them is the superconducting atomic limit (or Andreev limit), where the superconducting gap is considered to be much larger than the charging energy of the QD ($\Delta \gg U$), and the opposite limit, the so-called Yu-Shiba-Rusinov (YSR) limit ($\Delta \ll U$). We negotiate these scenarios in the zero bandwidth approximation (ZBA)[112,116–118], where the SC is treated as a single site with a pairing potential of Δ.

In the Andreev picture, quasi-particles are not allowed to appear in the SC. However, the superconductivity can couple the empty and doubly occupied QD states ($|0\rangle$ and $|2\rangle$ states from Fig. 2.1.2) via LAR as shown in Fig. 2.2.5**a** leading to a singlet superposition of them.

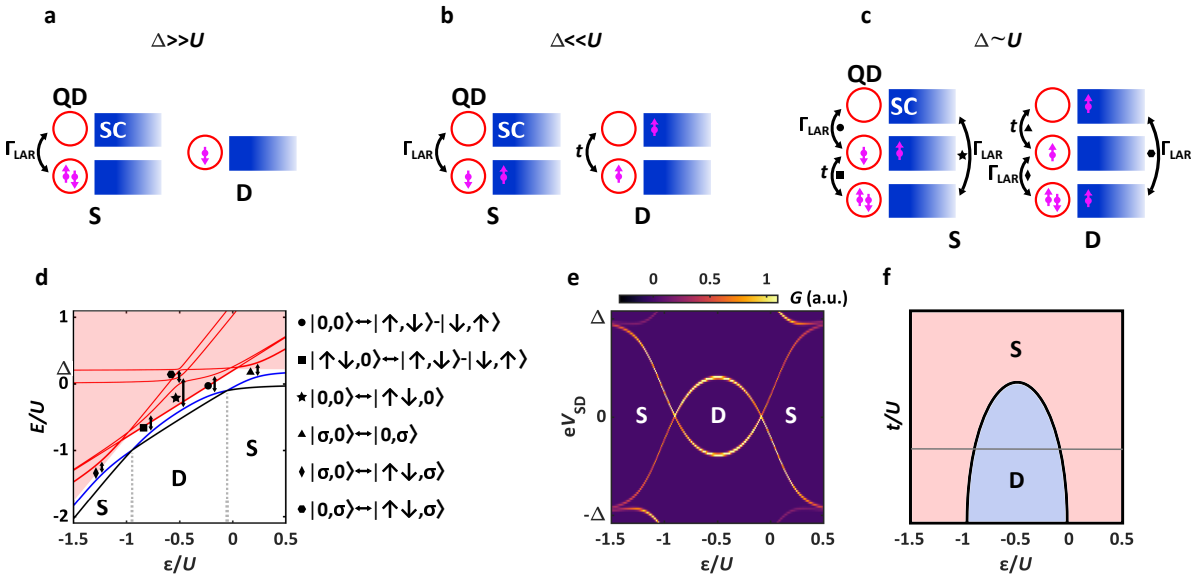

Figure 2.2.5: **Formation of superconducting bound states in QDs. a-c** Hybridization processes in different regimes. The red circle denotes the QD, whereas the blue rectangle is the superconducting electrode. Different configurations in different rows are coupled by LAR and tunneling processes (arrows). In the Andreev limit (**a**), the empty and double-occupied QD states can hybridize via LAR to form a singlet state (marked by "S"), while the doublet (marked by "D") remains intact. In the YSR limit (**b**), the double occupation of the QD is penalized. States with the same parity can hybridize in the presence of a finite tunnel coupling. In the intermediate limit (**c**), double occupation of the QD is allowed. Triplet states of parallel spins are excluded. **d** Energy diagram of the intermediate regime with $t/U = \Gamma_{\mathrm{LAR}}/U = 0.15$ and $\Delta/U = 0.2$. The black, blue, and red lines belong to the ground, first excited, and higher energy excited states, respectively. The hybridizations of different states are indicated by the black arrows assigned by the symbols from panel **c**. The energy diagram was calculated by the Author. **e** Simulated low-energy excitation spectrum of panel **c** exhibiting an "eye-shaped" curve. Transport takes place when a ground state transition ("S" to "D" or "D" to "S") is induced, i.e. at the crossing of the black and blue lines in panel **c**. **f** Phase diagram of the ground state character as a function of ε/U and t/U. The rastered region with pink represents a S ground state, the light blue a D one. By increasing t/U, the D shrinks in a dome shape.

Depending on the coupling strength, the ground state is either the doublet (singly occupied QD) or the singlet, and transitions can be induced between them by changing the on-site energy exhibiting dispersively evolving excitation lines. This limit is also discussed further in Fig. 2.2.7.

In the YSR limit, we assume that the double occupation of the QD is forbidden as a result of the large U. Therefore the relevant number of electrons in the QD, acting as an impurtiy [119–121], and quasi-particles in the SC is restricted to 0 or 1, as shown in Fig. 2.2.5**b**. In the following, we use the notation of $|n, m\rangle$ for $|n\rangle_{\mathrm{QD}} \otimes |m\rangle_{\mathrm{SC}}$ and σ for a single spin. Due to the spin degeneracy, the $|0\rangle_{\mathrm{QD}}$, $|\uparrow\rangle_{\mathrm{QD}}$, $|\downarrow\rangle_{\mathrm{QD}}$ and $|0\rangle_{\mathrm{SC}}$, $|\uparrow\rangle_{\mathrm{SC}}$, $|\downarrow\rangle_{\mathrm{SC}}$ configurations in the QD and the SC define 9 different states. When the total electron number parity of the system is even, the $|0, 0\rangle$ state can hybridize with the $|\uparrow,\downarrow\rangle - |\downarrow,\uparrow\rangle$ singlet, while in case of odd parity, the $|\sigma, 0\rangle$ and the $|0, \sigma\rangle$ doublets become coupled due to finite tunneling between the QD and the SC. Ground state transitions can be induced from the hybridized doublet to the hybridized singlet state (or from the singlet to the doublet) by changing the on-site energy.

Now we discuss an intermediate limit, where both U and Δ are finite and have the same order of magnitude. Compared to the YSR limit, the double occupation of the QD is allowed, while the number of quasi-particles is still restricted to 0 or 1. In this system, the occupations of $|0\rangle_{\mathrm{QD}}$, $|\uparrow\rangle_{\mathrm{QD}}$, $|\downarrow\rangle_{\mathrm{QD}}$, $|\uparrow\downarrow\rangle_{\mathrm{QD}}$ and $|0\rangle_{\mathrm{SC}}$, $|\uparrow\rangle_{\mathrm{SC}}$, $|\downarrow\rangle_{\mathrm{SC}}$ span 12 different states altogether.

Analogously to the YSR limit, the tunneling implies hybridization within the singlet and doublet subspaces, as depicted in Fig. 2.2.5**c**. The Fock-space Hamiltonian takes the form

$$H_{\mathrm{ABS}} = H_{\mathrm{QD}} + H_{\mathrm{SC}} + H_{\mathrm{T}}, \tag{2.2.35}$$

with

$$\begin{aligned} H_{\mathrm{QD}} &= \varepsilon \sum_{\sigma} n_{\sigma} + U n_{\uparrow} n_{\downarrow} \\ H_{\mathrm{SC}} &= \Delta \left(c^{\dagger}_{\mathrm{SC}\uparrow} c^{\dagger}_{\mathrm{SC}\downarrow} + c_{\mathrm{SC}\downarrow} c_{\mathrm{SC}\uparrow} \right) \\ H_{\mathrm{T}} &= t \left(\sum_{\sigma} d^{\dagger}_{\sigma} c_{\mathrm{SC}\sigma} + c^{\dagger}_{\mathrm{SC}\sigma} d_{\sigma} \right). \end{aligned} \tag{2.2.36}$$

Here $c^{(\dagger)}_{\mathrm{SC}\sigma}$ is the annihilation (creation) operator in the single SC site, t is the tunnel coupling between the QD and the SC, and the rest is the same as in Eq. 2.1.6. One can apply the Bogoliubov-transformation [70,122] (and its inverse transformation) as

$$\begin{aligned} c_{\mathrm{SC}\sigma} &= \frac{1}{\sqrt{2}} \left(\gamma_{\sigma} - \sigma \gamma^{\dagger}_{\bar{\sigma}} \right) \\ \gamma_{\sigma} &= \frac{1}{\sqrt{2}} \left(c_{\mathrm{SC}\sigma} + \sigma c^{\dagger}_{\mathrm{SC}\bar{\sigma}} \right), \end{aligned} \tag{2.2.37}$$

to diagonalize H_{SC}. $\gamma^{(\dagger)}_{\sigma}$ is the annihilation (creation) operator of a Bogoliubov quasi-particle with spin σ. The transformed H_{SC} and H_{T} from Eq. 2.2.36 with Eq. 2.2.37 then read as

$$H_{\mathrm{SC}} = \Delta \sum_{\sigma} \gamma^{\dagger}_{\sigma} \gamma_{\sigma}, \tag{2.2.38}$$

and

$$H_{\mathrm{T}} = \frac{t}{\sqrt{2}} \sum_{\sigma} \left(d^{\dagger}_{\sigma} \left(\gamma_{\sigma} - \sigma \gamma^{\dagger}_{\bar{\sigma}} \right) + \left(\gamma^{\dagger}_{\sigma} - \sigma \gamma_{\bar{\sigma}} \right) d_{\sigma} \right). \tag{2.2.39}$$

Eq. 2.2.38 counts the number of quasi-particles m_{SC} in the SC atomic sites. The energy spectrum of H_{ABS} after numerical diagonalization is shown in Fig. 2.2.5**d** along ε/U. States with 2 quasi-particles residing in the SC were excluded and $\Delta/U = 0.2$ and $t/U = 0.15$ parameters were used.

The black curve corresponds to the singlet (doublet) ground state "S"("D") at given ε/U and the blue one is the lowest-lying excitation. The red lines within the colored window represent higher energy excitations above Δ. The states depicted in Fig. 2.2.5**c** $|0,0\rangle$, $|\uparrow,\downarrow\rangle - |\downarrow,\uparrow\rangle$, $|\uparrow\downarrow,0\rangle$ in the singlet sector and states $|\sigma,0\rangle$, $|0,\sigma\rangle$, $|\uparrow\downarrow,\sigma\rangle$ in the doublet sector couple by direct tunneling ($t/\sqrt{2}$) or LAR ($\Gamma_{\mathrm{LAR}} = t/\sqrt{2}$) providing level repulsions in the energy diagram. All 6 hybridizations are indicated by the black arrows with symbols identifying the involved states from panel **c**, while triplet states $|\sigma,\sigma\rangle$ remain unaffected. In transport experiments, one can probe the excitation energies via finite-bias spectroscopy leading to an "eye-shaped" curve as a function of a plunger gate voltage, as outlined above. A simulation showing such a curve is depicted in Fig. 2.2.5**e** with the ground state characters indicated again by "S"("D"). The details of the numerical calculation of this curve are discussed in Chapter 4 (and in Appendix A.1) of a similar system. If the hybridization is sufficiently large the ground state is always a singlet and the doublet one vanishes. This finding is presented by a sketched phase diagram in Fig. 2.2.5**f**, where the ground state character ("S" in pink, "D" in blue) of the system is depicted along ε/U and t/U. The gray horizontal line indicates the value of t/U used in panel **e**. For an increasing t/U, the doublet sector originally existing at $-1 < \varepsilon/U < 0$ shrinks in a dome shape. As a result, the actual width of the "D" ground state is determined by the coupling strength,

which brings an asymmetry to the width of the even and odd occupation of the QDs in energy. However, the ZBA is only valid for small ($\sim t < \Delta, U$) couplings, thus the position of the dome top might deviate in a more elaborate model. In all 3 limits, the SC couples to the QD by either LAR or single electron tunneling so that sub-gap states are formed and the changes are redistributed between the SC and the QD.

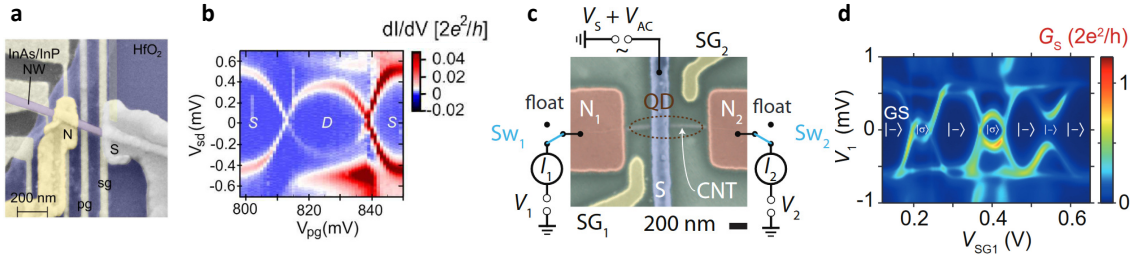

Figure 2.2.6: **ABS spectroscopy in SC-QD-N devices. a** SEM image of InAs/InP core-shell nanowire contacted by a superconducting and a normal electrode to perform tunneling spectroscopy. The QD level position is adjusted by the bottom gate voltage $V_{\rm pg}$. **b** ABS spectrum vs $V_{\rm pg}$. The dispersive lines match to the one from zero bandwidth approximation in Fig. 2.2.5**e**. **c** 3-terminal setup to probe the ABS in a carbon nanotube and **d** the local excitation spectrum captured in one of the leads. Compared to panel **b**, the SC-QD coupling is stronger deduced from the shape of the $|\sigma\rangle$ and $|-\rangle$ transitions. Panels **a-b** are adapted from Ref. 111, panels **c-d** from Ref. 113.

Numerous works studied different aspects of the ABSs in spectroscopy measurements mimicking an excitation spectrum introduced in panel **e**[99,103–106,111,112,114,115,123,124]. One example where the ABS excitation spectrum was captured in InAs/InP core-shell nanowire is introduced in Figs. 2.2.6**a-b** (adapted from Ref. 111). A superconducting and a normal electrode with plunger gates were installed (see panel **a**) to examine the SC-QD hybrid. Panel **b** reveals the dispersive ABS evolution with the plunger gate voltage matching to the curve derived in Fig. 2.2.5**e**. Another example of such measurements performed in a carbon nanotube is shown in Figs. 2.2.6**c-d** (adapted from Ref. 113). In a 3-terminal arrangement with one SC, two normal leads, and separate plunger gates (see panel **c**), the ABSs were studied both locally and non-locally (the latter one is not discussed here). A couple of singlet-doublet (indicated by $|-\rangle$ and $|\sigma\rangle$, respectively) ground state transitions are demonstrated involving further orbitals of the QDs. As the experiments tell, the universal features of the ABS are observable on multiple platforms.

We briefly elucidate the relationship between the traditional ABS and the one hosted by QDs. For simplicity, we consider the Andreev limit excluding any quasi-particles in the SC. Providing that the scattering center in Fig. 2.2.3**a** is substituted with a QD, a SC-QD-SC junction is established (see Fig. 2.2.7**a**). There is a phase difference introduced Eq. 2.2.34 between the source and drain superconducting electrodes, therefore the QD couples to them with $\Gamma_{\rm LAR} + \Gamma_{\rm LAR} e^{i\delta}$. Amending Eq. 2.2.35 with $\Delta \longrightarrow \infty$ leads to an effective Hamiltonian[125,126] of

$$H_{\rm ABS,eff} = H_{\rm QD} - \Gamma_{\rm LAR}\left(\left(1+e^{i\delta}\right) d_\uparrow^\dagger d_\downarrow^\dagger + \left(1+e^{-i\delta}\right) d_\downarrow d_\uparrow\right), \tag{2.2.40}$$

from which the δ and ε dependent energy spectrum is derived by exact diagonalization, similarly to Eq. 2.2.35.

First, we look at the energy spectra of the ABS at fixed $\delta = 0$ and $\delta = \pi$, which are depicted in Figs. 2.2.7**b-c**. The pink and light blue curves are derived with $\Gamma_{\rm LAR}/U = 0.15$, and the red and dark blue ones are calculated with $\Gamma_{\rm LAR}/U = 0.3$ values. For $\delta = 0$ (panel **b**), a diagram similar to Fig. 2.2.5**d** is obtained with the dispersive, anti-crossing singlet states (solid lines) and the decoupled doublet state (dashed pink-red line). The anti-crossing corresponds to the hybridization of the one with the "★" icon in Fig. 2.2.5**d**. For weak coupling (pink lines),

the ground state is a doublet ("D") for a certain ε interval bordered by the gray dashed lines, otherwise, it is always a singlet ("S") of

$$|S\rangle = |-\rangle = u|0\rangle_{\mathrm{QD}} - v^*|\uparrow\downarrow\rangle_{\mathrm{QD}}, \tag{2.2.41}$$

with

$$u(v) = \frac{1}{2}\sqrt{1 \pm \frac{\varepsilon + \frac{U}{2}}{\sqrt{\left(\varepsilon + \frac{U}{2}\right)^2 + \Gamma_{\mathrm{LAR}}^2}}}. \tag{2.2.42}$$

In contrast, the hybridization is absent for $\delta = \pi$ in panel **c** as expected from Eq. 2.2.40. Naively the independent fluctuations of the Cooper pairs between the QD and the two SCs can be argued restoring the simple Coulomb blockade behavior. Fig. 2.2.7**d** presents the lowest-energy excitations, ΔE, of panels **b-c**. While the pink line of $\delta = 0$ exhibits the "eye-shaped" curve reminiscant to the calculated one in Fig. 2.2.5**e**, the red one does not cross at zero energy preserving the singlet ground state of the system, regardless of ε. As outlined above, for $\delta = \pi$ the Coulomb diamonds are recovered (see Fig 2.1.2).

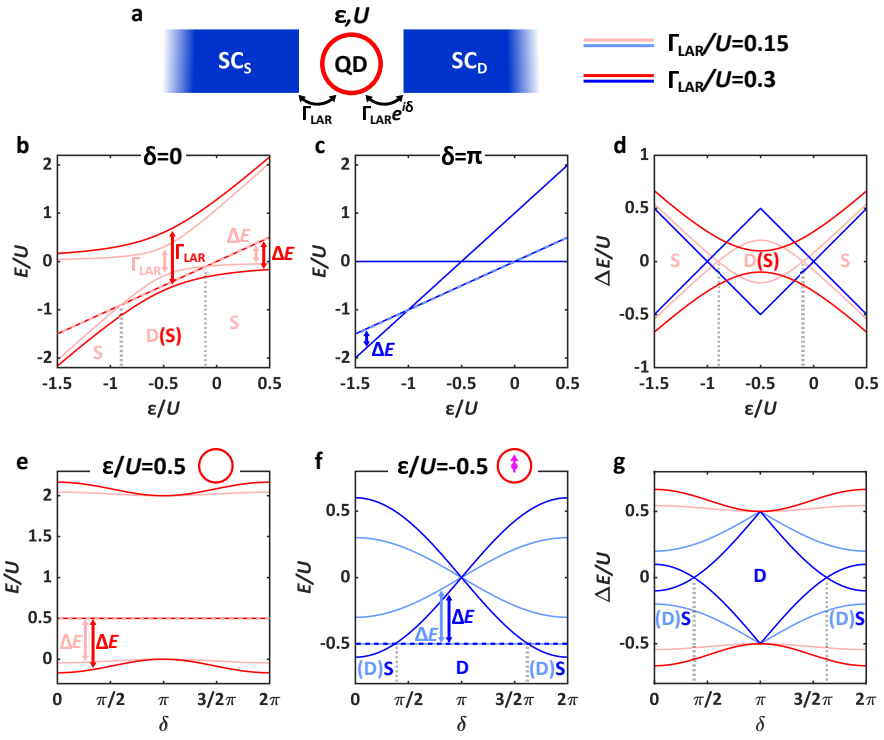

Figure 2.2.7: **ABS in a SC-QD-SC junction.** **a** Sketch of a QD connected to two SCs. Due to the superconducting phase difference of the electrons, δ, the coupling Γ_{LAR} becomes phase dependent. **b** E vs ε/U diagram of the SC-QD-SC system in the Andreev limit for $\delta = 0$ and **c** $\delta = \pi$. "S"("D") letters indicate the singlet (doublet) ground states. **d** Lowest energy excitation spectra of panels **b-c**. For $\delta = 0$ (pink and red lines), the typical ABS curves of the hybridized states are restored, for $\delta = \pi$ (blue lines) only the Coulomb diamonds are observable. **e** Energy spectrum of the ABSs vs δ for an empty QD and **f** for a singly occupied one. While the ground state is always a singlet for $\varepsilon/U = 0.5$, in the single occupation, δ drives a singlet-doublet transition if Γ_{LAR} is large (dark blue curve). **g** Similar spectra to panel **d**, but plotted along δ with fixed ε/U values from panels **e-f**. It exhibits similar development to the traditional ABS spectra too.

We now turn to the investigation of the spectra as a function of δ at fixed QD occupations, i.e. ε/U values. In Fig. 2.2.7**e**, E is plotted with the QD being empty ($\varepsilon/U = 0.5$). The ground state is always the singlet, whose energy develops dispersively alike with the ABS in Fig. 2.2.3**b**,

while the energy of the doublet (dashed pink-red line) is constant. Here one can say that Γ_{LAR} defines the bandwidth of the ABS. Fig. 2.2.7**f** shows the spectrum with the QD filled with a single electron ($\varepsilon/U = -0.5$)[127]. If the coupling is strong (see the dark blue line), the ground state is a singlet in the vicinity of $\delta = 2n\pi, n \in \mathbb{Z}$, which is driven to the doublet by shifting δ towards $(2n+1)\pi$ outputting a ground state transition at the gray dashed lines. Fig. 2.2.7**g** illustrates the lowest-lying single electron excitations from panels **e-f**, analogously to panel **d**, revealing akin features with ε/U and δ. More elaborate calculations confirm such behavior of the ABS realized in SC-QD-SC junctions[109,128]. Both on-site charge and phase-biased ground state transitions are found in Refs. 99,101,129 and 130.

2.3 Superconducting quantum dots

Bulk SCs behave as Cooper pair reservoirs. Compared to the huge number of condensed electrons (and the number of available orbitals) in the metal, its fluctuation is negligible, which is the motivation behind the employment of a mean-field approximation derived in Eq. 2.2.11. The picture changes qualitatively if the size of the SC is finite, which we briefly review below.

2.3.1 Canonical ensemble & ultra small superconductors

Coulomb repulsion becomes significant with scaling down the dimension penalizing the charging with U per electron. Furthermore, for ultra-small SC grains, the average level spacing δ (see Eq. 2.1.3) takes a finite value. The grand-canonical description of Eq. 2.2.11 is no longer valid, the particle number becomes a conserved quantity, and the SC itself acts as a QD, which we refer to as a superconducting island (SCI) from now on. With the number of electrons fixed at N_0, the electrostatic contribution is constant, and the SCI must be discussed in the canonical ensemble[131]. One such way is conducted by the Richardson model, which assumes inter-site pairing on the SCI orbitals. The Richardson Hamiltonian[132–134] reads similarly to Eq. 2.2.3 as

$$H_{\mathrm{R}} = \underbrace{\sum_i \varepsilon_i c_{i\sigma}^\dagger c_{i,\sigma}}_{H_0} \underbrace{- V \sum_{i,j\in S} c_{i\uparrow}^\dagger c_{i\downarrow}^\dagger c_{j\downarrow} c_{j\uparrow}}_{H_{\mathrm{int}}} . \tag{2.3.1}$$

Here H_0 describes the kinetic energy with the discerete orbitals separated by δ and the summation goes over them, while H_{int} expresses the superconducting correlations on these orbitals. $c_{i\sigma}^{(\dagger)}$ is the annihilation (creation) operator of an electron in orbital i with spin σ. S labels the set of orbitals participating in the pair scattering, whereas V is its amplitude, which can be expressed as $V = \lambda\delta$, where λ is a dimensionless constant and δ is the level spacing, the inverse of the DOS at the Fermi level $\delta \approx \rho_{\mathrm{N}}(0)^{-1}$.

In Eq. 2.3.1, the ground state of H_0 is the Fermi-sea, Ψ_{FS}, which is the leftmost state in Figs. 2.3.1**a-b**. H_{int} scatters pairs of electrons between the sites and mixes the eigenstates of H_0, where orbitals above the Fermi energy is doubly occupied, while orbitals below it are empty. Although the kinetic energy increases with filling higher-lying levels, the system gains potential energy from the redistribution of the electron pairs, thus the orbitals around the Fermi energy become partially occupied. If N_0 is even, which we parametrize as $N_0 = 2n_0,\ n_0 \in \mathbb{N}$, the new ground state $\Psi_{\mathrm{G}}^{2n_0}$ is the coherent superposition of these eigenstates of H_0, which is illustrated in Fig. 2.3.1**a**. For $N_0 = 2n_0 + 1$ odd filling ($n_0 \in \mathbb{N}$ again), an orbital is occupied with a single electron (see Fig. 2.3.1**b** of $\Psi_{\mathrm{G}}^{2n_0+1}$), which blocks the level from being involved in any pair scatterings because H_{int} only transforms between empty or doubly occupied sites. As a result, the exclusion of that specific orbital weakens the amount of total correlations and so lowers the energy gain compared to the case of even filling.

As Δ characterizes the pairing energy in the bulk, BCS limit, one can introduce a similar

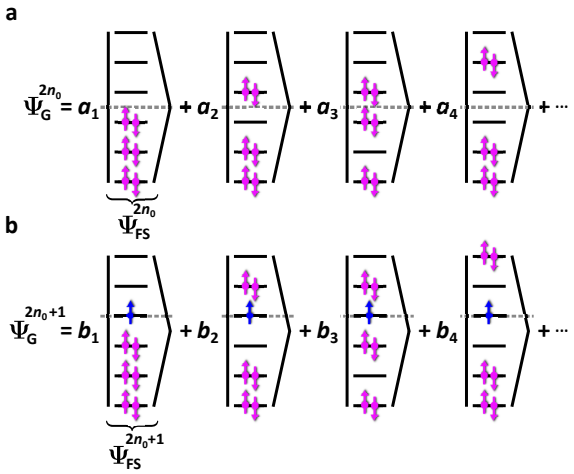

Figure 2.3.1: **Wave function of a SCI. a** Ground state wave function with even number of electrons ($2n_0$) on the island. The orbitals around the Fermi energy (gray dashed line) are partially filled due to H_{int} in Eq. 2.3.1. $\Psi_{\text{G}}^{2n_0}$ is a linear combination H_0 eigenstates by amplitudes a_i. **b** Similar to panel **a**, but with odd electron ocupation ($2n_0 + 1$). An unpaired electron (colored in blue) excludes one orbital from the pair scatterings, which decreases the total strength of superconducting correlations of the odd state. $\Psi_{\text{G}}^{2n_0+1}$ is again the superposition of H_0 eigenstates with amplitudes b_i.

quantity, Δ_{can}, measuring the overall strength of pair correlations in the canonical ensemble as well, or in other words, the energy window within the levels are partially doubly occupied and empty. Since Eq. 2.2.12 ultimately gives zero in the canonical ensemble, therefore Δ_{can} has to be defined differently. A natural choice[135] is

$$\Delta_{\text{can}} = V \sqrt{\sum_{i,j\in S} \langle c_{i\uparrow}^\dagger c_{i\downarrow}^\dagger c_{j\downarrow} c_{j\uparrow}\rangle - \langle c_{i\uparrow}^\dagger c_{j\uparrow}\rangle \langle c_{i\downarrow}^\dagger c_{j\downarrow}\rangle}, \tag{2.3.2}$$

which is appealing in the sense that $C_{ij} = \langle c_{i\uparrow}^\dagger c_{i\downarrow}^\dagger c_{j\downarrow} c_{j\uparrow}\rangle$ measures the pairing nature of the electrons and compares it to the uncorrelated state of levels i, j by subtracting $\langle c_{i\uparrow}^\dagger c_{j\uparrow}\rangle \langle c_{i\downarrow}^\dagger c_{j\downarrow}\rangle$. We note that $\mathcal{O}\left(\sum_{i,j\in S}\right) = N^2$, i.e. the number of non-zero correlators C_{ij} scale with N^2, where $N = |S|$ is the number of orbitals involved in the pair scatterings. Superconductivity breaks down at $\delta \gtrsim \Delta_{\text{can}}$, since $\mathcal{O}(N) = 1$, thus no correlation of Cooper pairs is observed anymore.

Besides the size of the pair correlations, Δ_{can} is also related to a gap in the excitation spectrum of an ultra-small SCI. In Refs 136 and 137, single-electron tunneling spectroscopy has been studied on nm-scale Al grains. It has been found that a spectroscopic gap in the order of $\sim \Delta_{\text{can}}$ exists between the first and second excited states if the ground state of the SCI has $2n_0 + 1$ and the excited states have $2n_0$ electrons (o$\longrightarrow$e transition with "o" and "e" labeling the odd and even parity states). This gap, which is significantly larger than the spacing between the subsequent excitations, is absent for the even $2n_0$ ground state and the odd $2n_0 + 1$ excited state characters (e$\longrightarrow$o transition). The phenomenon can be interpreted in the view of superconducting pairing correlations. By performing an o$\longrightarrow$e transition, the first excitation corresponds to the addition of an electron to the unpaired one, hence they can condense as a Cooper pair, while the rest of the excitations involve more quasi-particles with much higher energies. In contrast, after an e$\longrightarrow$o excitation, all odd states have at least one quasi-particle providing blocking effects. Consequently, the lowest and higher-lying excitations are not distinguished by any pair correlation effects and they stay gapless[131].

2.3.2 Electrostatic model

Now we focus on the limit of SCIs where the governing energy scale is the charging energy, U. It is typical for a few 100 nm long, a few 10 nm thick, and wide Al ribbons. We assume $\delta \longrightarrow 0$ such that $\delta \sum_i = N\delta = \int d\varepsilon = \text{const.}$, which simplifies the picture with the $\Delta_{\text{can}} \approx \Delta$ approximation.

The addition of a Cooper pair to the SCI costs $2U$, while it gains 2Δ energy, hence the charging and pairing as competitive effects are present simultaneously. The energy of the SCI develops quadratically in N_0 analogously to Eq. 2.1.1 and yields

$$E(N_0) = \left(\frac{N_0}{2} - \frac{C_{\text{G}} V_{\text{G}}}{e}\right) N_0 U + \Delta(N_0 \bmod 2). \tag{2.3.3}$$

The first term of Eq. 2.3.3 describes charge parabolas centered to the integer N_0 values, which is the standard behavior of a normal QD. The second term shifts the parabolas with $2n_0 + 1$ occupation up in energy with Δ since a single electron can enter the SCI only as a quasi-particle. This even-odd asymmetric of the SCI is characterized by the ratio of Δ/U which we clarify below.

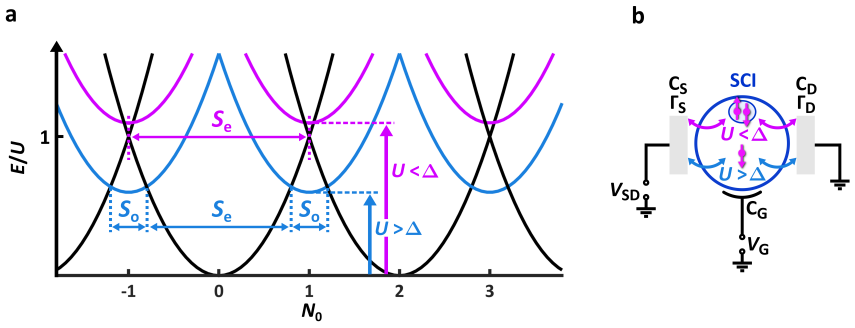

Figure 2.3.2: **Constant interaction model of a SCI. a** Energy of the SCI versus N_0 in the constant interaction picture. The black charge parabolas belong to $2n_0$, the blue ones to $2n_0 + 1$ electron fillings. Since one electron must exist as a quasiparticle in the odd state, the blue parabolas have an offset energy Δ. If $U < \Delta$ holds (purple), the ground state always has an even parity. For $U > \Delta$, the odd sector exists in $S_0 < S_e$ energy window. **b** Sketch of direct transport via a SCI. $U < \Delta$ implies the charging of Cooper pairs, while for $U > \Delta$ single charging is preferred. Standard quantities $(C_{\text{S(D)}}, C_{\text{G}}, \Gamma_{\text{S(D)}})$ can be treated similarly to normal QDs.

For $\Delta > U$, the ground state always has an even number of electrons conserved in Cooper pairs. The charge parabolas with even, $2n_0$ filling are illustrated by the black curves in Fig. 2.3.2**a**, whereas the odd $2n_0 + 1$ parabolas are depicted in purple. In this limit, the degeneracy of the even $2n_0$ and $2n_0 + 2$ states takes a lower energy than the $2n_0 + 1$ odd state, therefore the SCI is charged by 2 electrons when coupled to a source and a drain as shown in Fig. 2.3.2**b** (purple arrows). However, $\Delta < U$ predestinates odd occupation with one quasi-particle being unpaired at energy Δ because the double charging of $2U$ is less favorable than breaking a Cooper pair requiring 2Δ energy. This is manifested by the blue parabolas with odd parity intersecting the black ones below their degeneracy in Fig. 2.3.2**a**, where the Coulomb blockade is lifted and single electron transport can occur (see the blue lines in Fig. 2.3.2**b**). Consequently, an odd ground state sector with a width of S_0 is opened, while the even one of S_e is reduced from $2U$ [138–142]. The size of the Coulomb diamonds alternates with the ground state parity [141] as

$$\frac{S_o}{S_e} = \frac{U - \Delta}{U + \Delta}, \tag{2.3.4}$$

which is called the even-odd effect. We remark that if a sub-gap state exists in the vicinity of the SCI, its energy E_0 governs the lowest energy state instead of Δ as reported in several previous works [143–148]. The contraction of the odd state in the SCI, S_o, is similar to behavior of the ABS

discussed in the Anderson model previously, where the competition of the superconductivity and the finite U restricted the energy window of the doublet ground state. We note that the $\Delta \ll U$ limit restores the normal QD behavior, and the sketch of Fig. 2.3.2**b** can be replaced by Fig. 2.1.1**a**.

2.3.3 Coulomb-aided Yu-Shiba-Rusinov states

Previously we have seen that a grounded SC can hybridize with a single QD level via tunnel coupling and LAR. Even though 3 different limits have been discussed (Andreev, Shiba, intermediate), a very similar message has been concluded for all of them: a tunable bound state appears inside the superconducing gap as shown in Fig. 2.3.3**a**, where Δ_{YSR} reflects the excitation energy of the YSR state in question. Here we study how a SCI assists the formation of such sub-gap states.

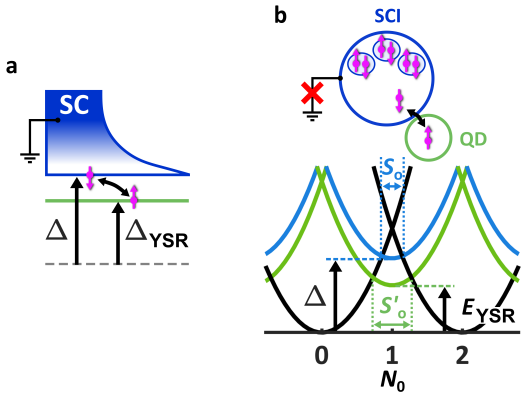

Figure 2.3.3: **Energy schemes of standard and Coulomb-aided YSR states. a** Excitation energy diagram of a single YSR state hosted by a grounded SC. The effective coupling between a magnetic impurity and a quasi-particle allows an excitation with energy Δ_{YSR} below the bulk gap Δ. **b** Energy relations of a SCI-QD hybrid as a function of N_0 induced on the SCI near the $\Delta \approx U$ limit. The Δ offset of the odd parabola (blue) is lowered by an effective coupling to a single electron thus creating a YSR-like singlet (green) with energy E_{YSR}. This effect also expands the size of the odd state ($S'_{\mathrm{o}} > S_{\mathrm{o}}$).

Let us consider a SCI and normal QD in series as sketched on the top of Fig. 2.3.3**b** with $\Delta \lesssim U_{\mathrm{SC}} < U_{\mathrm{QD}}$ superconducting gap, SCI, and QD charging energies, respectively. In this limit, changing the number of charges on the SCI by $2e$ is unfavorable, hence the LAR-related processes between the SCI and the QD are heavily suppressed. Nevertheless, if both the SCI and the QD have a single, unpaired electron of opposite spins (i.e. the fillings in the SCI and the QD are $2n_0 + 1$ and 1, respectively), they can tunnel couple via an effective exchange interaction. The SCI-QD hybrid gains energy and they constitute a so-called Coulomb-aided YSR singlet by sharing the electrons[149,150]. This effect can be visualized by comparative charge parabola plots of the SCI from Fig. 2.3.2**a**. In Fig. 2.3.3**b** the $2n_0 + 1$ odd parabolas are depicted in blue and green for 0 and 1 electron in the QD, respectively. As visible, S_o extends to a higher value of S'_o by changing the occupation of the QD from even to odd, and thus, the energy of the odd SCI state is decreased. In this case, the even-odd spacing ratio is given by

$$\frac{S'_o}{S'_e} = \frac{U_{\mathrm{SC}} - E_{\mathrm{YSR}}}{U_{\mathrm{SC}} + E_{\mathrm{YSR}}}, \tag{2.3.5}$$

where E_{YSR} is the minimal bound state energy of the odd state. We emphasize that E_{YSR} highlights the ground state energy of the system in contrast to Δ_{YSR} in Fig. 2.3.3**a** where the excitation energy was regarded.

Now we try to catch the peculiarities of the Coulomb-aided YSR states in a SCI-QD hybrid

in a frame of a minimal model as shown in Fig. 2.3.4**a**. The system can be described similarly to H_{ABS} in Eqs. 2.2.35 and 2.2.36 by replacing H_{SC} with a Richardson-like Hamiltonain. Assuming 2 pair-correlated sites on the SCI in the ZBA with energy Δ and a 2-level Anderson QD (with a finite level spacing of δ_{QD}), the Hamiltonian of the system is written as

$$H_{\mathrm{SCI-QD}} = H_{\mathrm{QD}} + H_{\mathrm{SCI}} + H_{\mathrm{T}}, \tag{2.3.6}$$

where

$$\begin{aligned}
H_{\mathrm{QD}} &= \varepsilon_{\mathrm{QD}} \sum_{\alpha} n_{\mathrm{QD}\alpha} + \left(\sum_{\alpha} n_{\mathrm{QD}\alpha} \right) \left(\sum_{\beta} n_{\mathrm{QD}\beta} - 1 \right) \frac{U_{\mathrm{QD}}}{2} + \sum_{\alpha} n_{\mathrm{QD}\alpha} \epsilon_{\mathrm{QD}\alpha} \\
H_{\mathrm{SCI}} &= \left(\varepsilon_{\mathrm{SC}} + \frac{\Delta}{2} \right) \sum_{i} n_{\mathrm{SC}i} + \left(\sum_{i} n_{\mathrm{SC}i} \right) \left(\sum_{j} n_{\mathrm{SC}j} - 1 \right) \frac{U_{\mathrm{SC}}}{2} + \sum_{i} n_{\mathrm{SC}i} \epsilon_{\mathrm{SC}i} \\
&\quad - \frac{\Delta}{N} \underbrace{\sum_{i,j} c^{\dagger}_{\mathrm{SC}i\uparrow} c^{\dagger}_{\mathrm{SC}i\downarrow} c_{\mathrm{SC}j\downarrow} c_{\mathrm{SC}j\uparrow}}_{W} \\
H_{\mathrm{T}} &= t \left(\sum_{\alpha i \sigma} d^{\dagger}_{\alpha\sigma} c_{\mathrm{SC}i\sigma} + c^{\dagger}_{\mathrm{SC}i\sigma} d_{\alpha\sigma} \right),
\end{aligned} \tag{2.3.7}$$

and

$$\begin{aligned}
n_{\mathrm{QD}\alpha} &= \sum_{\sigma} d^{\dagger}_{\alpha\sigma} d_{\alpha\sigma} \\
n_{\mathrm{SC}i} &= \sum_{\sigma} c^{\dagger}_{\mathrm{SC}i\sigma} c_{\mathrm{SC}i\sigma}.
\end{aligned} \tag{2.3.8}$$

Here $n_{\mathrm{QD}\alpha}$ is the particle number operator of orbital α in the QD with $d^{(\dagger)}_{\alpha\sigma}$ being the annihilation (creation) operator of an electron with spin σ, $\varepsilon_{\mathrm{QD}}$ is the QD on-site energy, and ϵ_{α} is the energy of orbital α, analogously to 2.1.4. Very similarly, $n_{\mathrm{SC}i}$ is the particle number operator of orbital i in the SCI with $c^{(\dagger)}_{\mathrm{SC}i\sigma}$ being the annihilation (creation) operator of an electron with spin σ, $\varepsilon_{\mathrm{SC}}$ is SCI on-site energy, and ϵ_i is the energy of orbital i. A uniform coupling t between any orbitals α of the QD and i of the SCI is assumed. W in the last term of H_{SCI} expresses the Richardson-like pair interaction, where $N = \sum_i$ is the number of sites in the SCI, which is 2 in our case.

We briefly comment on the combinatorial source of the Δ/N normalization prefactor there. According to Eq. 2.3.4, the even-odd effect vanishes, when $\Delta = U_{\mathrm{SC}}$ is satisfied. Even so, the $N_0 = 0$, $N_0 = 1$, and $N_0 = 2$ states are degenerate, which sets the

$$A\langle W \rangle = U_{\mathrm{SC}} \Big|_{\Delta = U_{\mathrm{SC}}} \tag{2.3.9}$$

condition for 2e charging, where A is the desired normalization constant. Assuming $\epsilon_i \approx \epsilon_j = \epsilon$ (negligible level spacing on the SCI), the orbitals are filled with $1/\sqrt{N}$ amplitude in the ground state. Therefore the diagonal contribution of $\langle W \rangle$ is 1 (since the 2 electrons can be annihilated and created on N orbitals), while the off-diagonal one is $(N-1)$ (as the 2 electrons can be scattered from N orbitals to $N-1$ new ones). Substituting the $\langle W \rangle = N$ result into Eq. 2.3.9, $A = \Delta/N$ is given.

Using the same methodology as for normal double QDs in Eq. 2.1.18, the stability diagram of the SCI-QD hybrid can be derived by the direct diagonalization of Eq. 2.3.6. Such map revealing

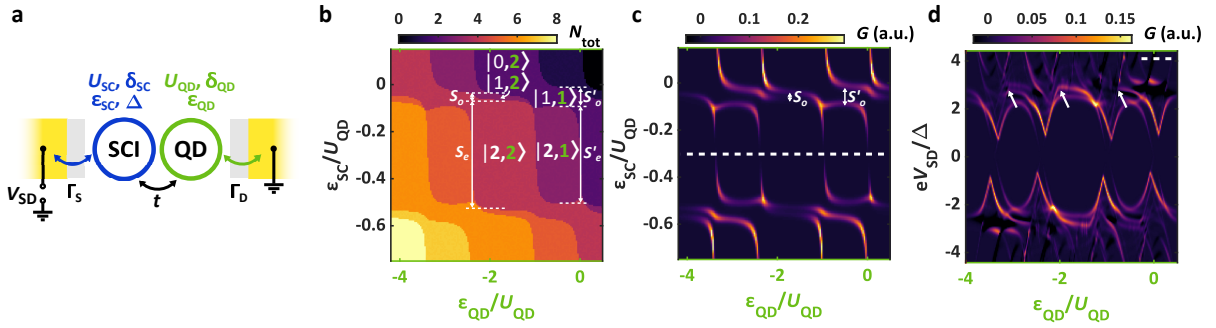

Figure 2.3.4: **Numcerical simulation of Coulomb-aided YSR states.** **a** Sketch of the simulated junction. The charge stability map and the current via normal leads of the SCI-QD hybrid was calculated. **b** Ground state stability diagram of ($N_{\rm tot}$) as a function of $\varepsilon_{\rm QD}$ and $\varepsilon_{\rm SC}$ normalized with $U_{\rm QD}$. The width of the charge sectors of the SCI is described by S_e, S_o, S'_e, and S'_o belonging to the $|2n_0, 2\rangle$ (even-even), $|2n_0+1, 2\rangle$ (odd-even), $|2n_0, 1\rangle$ (even-odd), and $|2n_0+1, 1\rangle$ (odd-odd) states. $S_o < S'_o$ suggests a state being present below Δ as explained by Fig. 2.3.3**b**. **c** Calculated differential conductance based on panel **a**. G is maximal around the triple points, however, it is still finite in the blockaded regions too as cotunneling takes place either via the SCI or the QD. The extension of S'_o compared to S_o is visible again. **d** Calculated transport spectrum of the system along the white dashed line in panel **b**. The white arrows show the distortions and discontinuities coming from breaking of the electron-hole symmetry by the finite $U_{\rm SC}$. The simulations were performed by the Author.

the expectation value of the total charge in the ground state, $\langle\Psi_{\rm G}|\sum_{i,\alpha}\left(n_{{\rm SC}i}+n_{{\rm QD}\alpha}\right)|\Psi_{\rm G}\rangle = N_0 + N_{\rm QD} = N_{\rm tot}$, is shown as a function of $\varepsilon_{\rm QD}$ and $\varepsilon_{\rm SC}$ in Fig. 2.3.4**b**. The stability diagram resembles the one in Fig. 2.1.4**c**, however, here we considered two orbitals on both the QD and the SCI. In the simulation, $U_{\rm QD} = 1$, $U_{\rm SC} = 0.2$, $\delta_{\rm QD} = \epsilon_{\rm QD2} = 0.4$, $\delta_{\rm SC} = \epsilon_{\rm SC2} = U_{\rm SC}/100$, $\Delta = 0.18$, and $t = 0.04$ units have been used, typical for a semiconducting QD attached to a thin, few 100 nm long Al island. The honeycomb structure exhibits the even-odd alternation of the SCI Coulomb blockade indicated by the arrows of S_e and S_o along they vertical axis. Nonetheless, the odd diamond is wider along $\varepsilon_{\rm SC}/U_{\rm QD}$ in the $|1,1\rangle$ sector than in the $|2,1\rangle$ (or $|0,1\rangle$) sector, indicated by $S_o < S'_o$, where $|m,n\rangle = |m\rangle_{\rm SC} \otimes |n\rangle_{\rm QD}$ denotes the occupation of the SCI and the QD. This is the main feature of our simple model proving the Coulomb-aided YSR theory. Applying a similar rate equation model of the normal double QD system in Fig. 2.1.4**d**, zero-bias transport through the SCI-QD hybrid coupled to metallic leads with $\Gamma_{\rm S}$ and $\Gamma_{\rm D}$ can be calculated as demonstrated in Fig. 2.3.4**c**. Besides the conductance G is enhanced around the triple points as both the QD and the SCI are resonant there, it is also finite deeper in the blockades where either the SCI or the QD serves as a cotunneling probe. The details of the calculation are presented in Appendix A.1.

The excitation spectrum of a Coulomb-aided YSR singlet also develops unusally compared to an ordinary one of a grounded SC-QD introduced in Fig. 2.2.5**e**. The finite $U_{\rm SC}$ breaks the electron-hole symmetry and the energy cost for the addition or the removal of an electron turns out to be different. Correspondingly, the excitations of the system become distorted, which our model can also reproduce. Fig. 2.3.4**d** shows the calculated transport spectrum ($G = dI/dV_{\rm SD}$) along the white dashed line in panel **b** keeping the SCI doubly occupied. One can see that the "eye-shaped" curves typical for bound states are multiplied and asymmetric for $\varepsilon_{\rm QD}$ (highlighted by the white arrows) as outlined above.

Experimental signature of a Coulomb-aided YSR state has been reported very recently. In Ref. 150, the interaction of an Al island and a QD formed in a single InAs nanowire was studied via transport measurements. The false-colored SEM image of the two-terminal device is shown in Fig. 2.3.5**a**. Panel **b** demonstrates the stability diagram (differential conductance G) of the system controlled by the QD gate $V_{\rm N}$ and the SCI gate $V_{\rm S}$. In the measurements, when the QD is occupied with 0 or 2 electrons ($V_{\rm N} < -171\,{\rm mV}$ and $V_{\rm N} > -168\,{\rm mV}$ values) the SCI is always

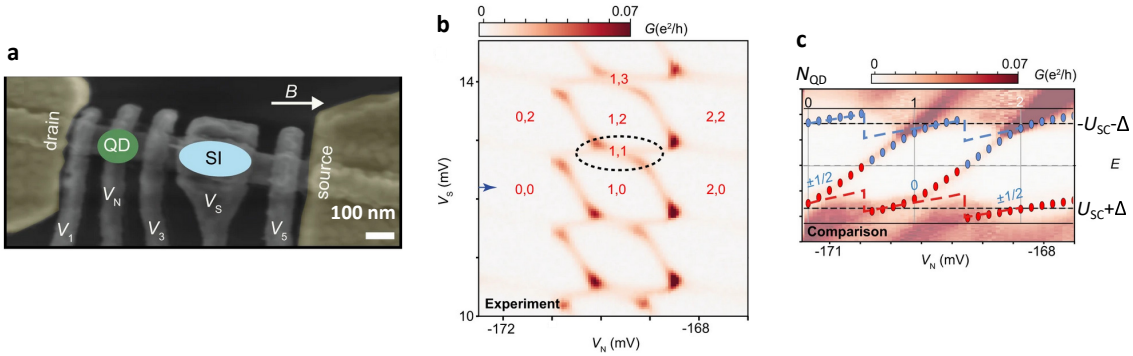

Figure 2.3.5: **Experimental realization of a Coulomb-aided YSR state. a** SEM image of an InAs nanowire attached to metallic leads (yellow). A QD was electrostatically formed in the vicinity of an Al islands that were tuned by V_N and V_S, respectively. **b** Zero-bias conductance (G) vs V_N and V_S indicating the SCI and QD charge configurations (N_0, N_{QD}). The $n_0 = 1$ sector of the SCI is only resolved at $\nu = 1$ suggesting a YSR singlet existing there. **c** Finite-bias spectroscopy vs V_N along the blue arrow in panel **b**. The excitations develop in a distorted way from zero to $U_{SC} + \Delta$ energy. The blue and red dots are theoretical curves tagged by the spin character of the excited states. The figures are adapted from Ref. 150.

charged with 2e and the odd sector is absent suggesting $U_{SC} \geq \Delta$. As the electron number in the QD is tuned to 1 ($V_N = -170.5\,\text{mV}$), the odd filling of the SCI is revealed indicated by the 1,1 sector (with the N_0, N_{QD} notation) inside the blue dashed circle. This finding confirms the assumption of a YSR singlet residing in the SCI-QD hybrid since Δ is effectively reduced to E_{YSR} based on Eq. 2.3.5. The Authors performed bias spectroscopy along the horizontal blue arrow in panel **b**, which is shown in panel **c**. The distorted sub-gap excitation lines they observed were fitted by a theoretical curve (blue and red dots) derived from Ref. 149. These lines follow the development of a single Coulomb-aided YSR state matching well to the experiments. Although the spectrum of Fig. 2.3.5**c** looks rather different than our one demonstrated previously in Fig. 2.3.4**d**, the deformed YSR states are captured in both of them.

Next, we review how the ABSs and YSR states can be utilized in novel SC circuits and qubit concepts.

2.4 Majorana fermions, the Kitaev chain & outlooks

The main concern of the common, superconductivity-based qubits is their susceptibility to external noises, leading to computational errors and decoherence. The application of MFs, as exotic, non-Abelian excitations, proposes a suitable solution for the problem since their quantum states are topologically protected [44–47]. Now we discuss how MFs can be represented, and more importantly, realized.

2.4.1 Theory of the Kitaev chain

Let us consider a 1D array of atomic sites, where the adjacent sites are coupled by a tight-binding hopping t (assumed to be real) and a pairing potential $\Delta = |\Delta|e^{i\Phi}$. Selecting only one spin flavor, the Hamiltonian of this so-called Kitaev chain [151] reads as

$$H_{\text{Kitaev}} = -\sum_j \left(\mu c_j^\dagger c_j + t\left(c_j^\dagger c_{j+1} + c_{j+1}^\dagger c_j\right) - \left(\Delta c_j c_{j+1} + \Delta^* c_{j+1}^\dagger c_j^\dagger\right)\right) \tag{2.4.1}$$

where μ is the chemical potential and $c_j^{(\dagger)}$ is the annihilation (creation) operator of an electron at the j-th lattice site. By introducing the Majorana operators

$$\begin{aligned} \Upsilon_{2j-1} &= e^{i\frac{\Phi}{2}} c_j + e^{-i\frac{\Phi}{2}} c_j^\dagger \\ \Upsilon_{2j} &= -ie^{i\frac{\Phi}{2}} c_j + ie^{-i\frac{\Phi}{2}} c_j^\dagger, \end{aligned} \tag{2.4.2}$$

and their inverse as

$$c_j^{(\dagger)} = \frac{1}{2} e^{\mp i\frac{\Phi}{2}} \left(\Upsilon_{2j-1} \pm i\Upsilon_{2j} \right), \tag{2.4.3}$$

Eq. 2.4.1 is rewritten in a fashion of

$$H_{\text{Kitaev}} = \frac{i}{2} \sum_j \left(-\mu \Upsilon_{2j-1}\Upsilon_{2j} + \left(|\Delta| + t\right) \Upsilon_{2j}\Upsilon_{2j+1} + \left(|\Delta| - t\right) \Upsilon_{2j-1}\Upsilon_{2j+2} \right). \tag{2.4.4}$$

We note that Majorana operators have the identities

$$\begin{aligned} \Upsilon_\alpha &= \Upsilon_\alpha^\dagger \\ \Upsilon_\alpha^2 &= 1, \end{aligned} \tag{2.4.5}$$

and they obey the anti-commutation relation

$$\{\Upsilon_\alpha, \Upsilon_\beta\} = 2\delta_{\alpha\beta}. \tag{2.4.6}$$

According to Eq. 2.4.3, intuitively, a Majorana can be considered as "half" of an electron. Eq. 2.4.4 has 2 special phases: the trivial one with $t = |\Delta| = 0,\ \mu < 0$ yielding

$$H_{\text{triv}} = \frac{-i}{2} \mu \sum_j \Upsilon_{2j-1}\Upsilon_{2j} \tag{2.4.7}$$

and the topological phase with $t = |\Delta| > 0,\ \mu = 0$ condition leading to

$$H_{\text{top}} = it \sum_j \Upsilon_{2j}\Upsilon_{2j+1}. \tag{2.4.8}$$

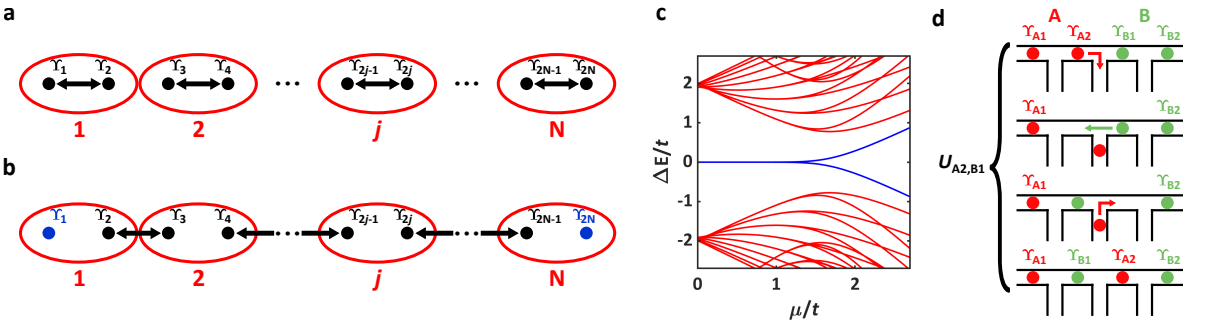

Figure 2.4.1: **Features of the Kitaev chain.** **a** Cartoon of the Kitaev chain with N atomic sites in the trivial and **b** in the topological phase. The j-th site (red) is represented by Υ_{2j-1} and Υ_{2j} Majorana modes. In the trivial phase, intra-site pairing (black arrows), in the topological one, inter-site pairing occurs leaving Υ_1 and Υ_{2N} (blue) unpaired. **c** Simulated excitation energy spectrum ($\Delta E/t$) of the Kitaev chain with $N = 10$ sites and $|\Delta| = 0.95t$ along μ/t. For $\mu/t \ll 1$, the bulk gap is $\sim 2t$. The Majorana zero modes (blue) only split when the bulk gap with the rest of the excitations (red) closes ($\mu/t \approx 1.5$). **d** Schematics of Majaroana braiding using T-junctions. As the MFs Υ_{A2} and Υ_{B1} belonging to chains A and B, respectively, are interchanged, the output is a non-trivial superposition of the fermion modes on sites A and B.

The trivial phase of Eq. 2.4.7 induces the pairing of Majoranas on-site as shown in Fig. 2.4.1**a**. In the topological phase, the Majoranas pair up from different sites as illustrated in Fig. 2.4.1**b**. If the total number of lattice sites is N, since the summation goes over j from 1 to $N-1$ in Eq. 2.4.8, the two Majoranas at the end of the chain remain unpaired, therefore the commutators

$$\{\Upsilon_1, \Upsilon_{2N}\} = \left[H_{\text{top}}, \Upsilon_1\right] = \left[H_{\text{top}}, \Upsilon_{2N}\right] = 0, \tag{2.4.9}$$

convey zero-energy states localized at the end of the wire. Analogously to Eq. 2.4.3 a non-local, zero-energy fermion operator can be assigned to them

$$c_{\text{end}}^{(\dagger)} = \frac{1}{2}\left(\Upsilon_1 \mp i\Upsilon_{2N}\right). \tag{2.4.10}$$

The two-fold degenerate ground state encodes a qubit with basis states

$$|1\rangle = c_{\text{end}}^{\dagger}|0\rangle, \tag{2.4.11}$$

where the information is stored in the fermion parity of the system. While the bulk is gapped, $c_{\text{end}}^{(\dagger)}$ does not enter H_{top}, thus the movement of the unpaired Majorana energy levels is forbidden if they are separated ($N \gg 1$), providing the topological protection we desired. Even if $\mu \neq 0$ and $t \neq |\Delta|$ hold, the overlap of the Majorana zero modes is negligible as long as the gap is finite. The energy spectrum of Eq. 2.4.4 as a function of the chemical potential for $N = 10$ is calculated in Fig. 2.4.1**c**, demonstrating the presence of a finite gap even if the detuning of μ is considerable ($|\Delta| = 0.95t$ was assumed).

One can also show that exchange of MFs α and β can be expressed by the unitary operator

$$U_{\alpha\beta} = e^{\frac{\pi}{4}\Upsilon_\alpha \Upsilon_\beta}. \tag{2.4.12}$$

Rotation between MFs do not only acquires a phase factor in the wavefunction, but it can result in a non-trivial superposition of states, e.g. if Υ_α and Υ_β are shared with other chains. This kind of braiding of a Majorana network can be represented by the sequential movements of MFs in a series of T-junctions[46]. Fig. 2.4.1**d** shows and example of interchanging 2 MFs,Υ_{A2}, Υ_{B1}, belonging to Kitaev chains A and B. This minimal system sets up 2 qubits with 2 fermionic modes. The operator $U_{\text{A2,B1}}$ transforms the basis states into a highly entangled one, which reveals the non-Abelian statistics of MFs. Therefore a sufficiently large network is convenient to perform protected quantum algorithms, where the fermion parity degrees of freedom are shared between the MFs. Since $U_{\alpha\beta}$ does not even depend on the trajectory or any other details of the swap, the results of the algorithms are very accurate.

We note that even MFs can be generalized further by the identity of

$$\begin{aligned} \Upsilon_\alpha \Upsilon_\alpha^\dagger &= \Upsilon_\alpha^\dagger \Upsilon_\alpha e^{-\frac{2\pi i}{n}},\ n \in \mathbb{Z},\ n > 2 \\ \Upsilon_\alpha^n &= 1, \end{aligned} \tag{2.4.13}$$

where $\Upsilon_\alpha^{(\dagger)}$ is a parafermion annihilation (creation) operator[152–154]. As a versatile tool beyond MFs, parafermions offer the topologically protected implementation of more universal quantum gates, e.g. a CNOT gate[43].

2.4.2 Physical implementation

Next, we dispute the physical realization of the Kitaev chain. Associating to Eq. 2.4.1, 5 crucial requirements have to be fulfilled. First of all, the system in question must have a longitudinal structure (i) to restrict the electron propagation to close-to-1D, e.g. like a quantum wire. In the second place, μ and t must be well-controllable (ii). Since the Kiatev model is spin-

less, one has to lift the Kramer's degeneracy by the Zeeman splitting of the finite magnetic field (iii)[155]. For the spin-less electron pairing, p-wave superconductivity has to be maintained, which is managed if an s-wave SC is attached (iv) to the wire, while a strong spin-orbit interaction (v) is present to rotate the spins.

In the light of the wishlist from above, an InAs nanowire coupled to a SC seems an appropriate choice[115,156–159]. While the fulfillment of (i) is self-explanatory, InAs is a semiconductor built from heavy atoms, thus owns a strong intrinsic spin-orbit coupling, which satisfy (ii) and (v). The existence of (iii) and (iv) together is granted by the relatively large g-factor[160–163] and the proximity-induced superconductivity from the coupled s-wave SC[71,74].

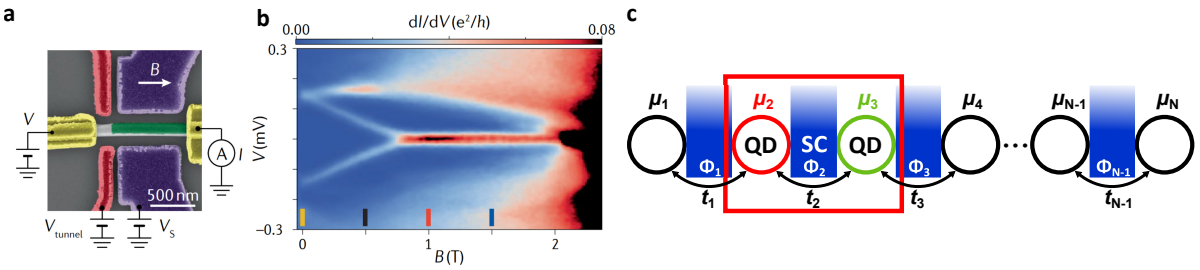

Figure 2.4.2: **Possible realization of MFs.** **a** False-colored SEM micrograph of a nanowire device designed for tunneling spectroscopy of MFs (green: SC, yellow: normal leads, red and purple: plunger gate electrodes). **b** Excitation spectrum of the Majorana wire along an axial magnetic field (B). By increasing B, the lowest energy excited states (possibly ABSs) converge to zero. At $B \approx 0.8\,\mathrm{T}$, they merge in a robust zero-bias peak speculated as a Majorana zero mode. **c** Kitaev chain built from a sequence of QDs and pieces of SCs. The individual tunability of μ_j, t_j, and Φ_j is advantageous compared to single Majorana wires. The fundamental unit of this chain is a double QD coupled via a joint SC (bordered by the red rectangle), which we study in the remaining part of the thesis.

Indeed, the experimental signature of MFs has already been reported in nanowire devices[144,158,164–168] suggested by the literature[156,157]. As an example, Figs. 2.4.2**a-b** show a MF tunneling spectroscopy accomplished in an InAs nanowire coupled to a SC and a normal probe[115,166]. Panel **b** shows the development of the excitation spectrum as a function of an axial magnetic field, typical for MF experiments. Above a certain field, the zero-bias peak is attributed to MFs (as introduced in Fig. 2.4.1**c**), however, an irrefutable proof is not given[169], and the presence of Majoranas in similar geometries is still under debate in the community since various other effect can provide such zero-bias anomalies. We also stress out that Majorana zero modes appear in pairs at the end of the wires, which have not been detected simultaneously. Another troublesome side of the nanowire-based Majorana proposal is the poor control of μ and t violating condition (ii). Moreover, to obtain a stable topological phase, the disorders coming from the random electron potential along the wire should be suppressed.

The question arises of how the difficulties outlined above can be resolved and whether there is a practical realization of the Kitaev chain. Let us put together what we have reviewed in the previous Sections. One can suppose a system with QDs coupled to each other via SCs in a linear array, illustrated in Fig 2.4.2**c**, which resembles the original model from Eq. 2.4.1[48], thus, from now, we refer to it simply as the Kitaev chain. The huge advantage here is that the chemical potential is well-defined and controlled by the QD level positions (μ_j). Furthermore, the electron hopping between the neighboring QDs (t_j) sets a lot softer condition to maintain the topological phase compared to the completely ballistic nature of transport required in a Majorana wire. The superconducting phases of each SC (Φ_j) provide another degree of freedom to tune the system (e.g. to get rid of random π junctions)[48], but the spin-orbit interaction and the Zeeman field are still necessary. We remark that, although the Kitaev chain is eventually a non-interacting electron lattice (except the superconducting pairing), the effective behavior does not change if a weak electron-electron interaction is included[151]. In other words, a term

with four fermionic operators added to Eq. 2.4.1 only counts as a perturbation. Due to this fact the SCs drawn in Fig. 2.4.2**c** might be replaced with superconducting grains or SCIs, which we have just reviewed in the frame of the canonical ensemble in Eq. 2.3.1. These benefits raise the Kitaev chain superior to any traditional single-wire Majorana devices.

If we take a look at the Kitaev chain, it is obvious that its fundamental building block is a parallel double QD coupled to a SC (designated by the red rectangle in Fig. 2.4.2**c**)[170–172]. This is such a minimal chain where a SC can yet assist the inter-site coupling (red and green QDs), expressing the non-local peculiarities of ABSs in two QDs and the main idea of the Kitaev chain[173–176]. Ref. 172, also highlights that this double QD system can possess the Majorana statistics if the parameters are tuned properly, even though the predicted zero modes are not topologically protected yet. Therefore discovering the effects of LAR, CAR, EC[177], and the Coulomb repulsion as resources of the interaction is the main interest of the thesis. We investigate the minimal Kitav chain block in different geometries, limits, and aspects: we examine the CPS (weak coupling limit), the hybridization of two ABSs (or YSRs) resulting in a 2-atomic so-called Andreev molecule (strong coupling limit), and the formation of a 3-atomic (or polyatomic) Andreev molecule rooting from YSR states binding to unpaired electrons of a SCI (Coulombic limit). With the desired interaction of the QDs, one can obtain longer chains by copying the blocks next to each other as in Fig. 2.4.2**c** opening up the possibility to realize topologically protected MFs.

Experimentalwise, the realization of CPS, a 2-atomic, or a polyatomic Andreev molecule imposes a set of challenging constraints: the QDs must be decently coupled to the SC, and their distance should be minimized while preventing direct tunneling between them[96,178]. To satisfy these requirements we construct our artificial atoms in a novel superconducting hybrid nanostructure, where double InAs nanowires are grown in close vicinity and are connected by an epitaxial SC Al shell[148,150,179–182]. Whereas two QDs can be formed in separate wires thereby excluding the direct tunneling between them, the epitaxial Al shell yields a high-quality, defect-free SC-semiconductor interface ensuring the strong proximity[183,184] and SC-QD coupling as used in various hybrid quantum devices. Z3 parafermions are also theorized to appear in a pair of tightly placed wires with a joint SC by exploiting the CAR and the Coulomb interaction[75–77].

We note that as a result of the minimal distance between the QDs preferred for CPS and the Andreev molecule, the inter-dot Coulomb repulsion also becomes significant. One has to be cautious since this parasitic effect competes with the SC-induced inter-wire transport processes, where two electrons are transmitted through the adjacent QDs. Therefore the impact of the Coulomb repulsion is studied thoroughly in all Chapters 3, 4, and 5. For the next step, we discuss sample fabrication and measurement techniques.

2.5 Sample fabrication & measurement technique

We go through the sample fabrication process from the growth of the parallel nanowires via standard nanofabrication techniques (electron beam lithography, EBL) to the cooldown of the devices.

2.5.1 Growth & manipulation of parallel InAs nanowires

InAs is a III-V type semiconductor that can be synthesized as a heterostructure with many different vapor deposition techniques. The parallel nanowires of our interest are grown by molecular beam epitaxy (MBE) with in-situ epitaxial Al deposition, whose procedure is illustrated in Fig. 2.5.1**a**. MBE is a crystal formation procedure where an ordered layer of atoms is imposed upon an existing one. The pure elements are stored in separate effusion cells (Knudsen cells), where the materials are heated to a base temperature generating a flux (red and green beam in

Fig. 2.5.1**a**). Shutters are used to block the molecular beams when they are out of operation. The target is positioned in the middle of an ultra-high vacuum (UHV) chamber preventing the infiltration of any contamination. On a substrate, a pair of Au catalyst droplets, as the "seeds" of the parallel nanowires are pre-defined by EBL. In the growth chamber, as the In and As enter the Au, it oversaturates and the components nucleate on the substrate. Au droplets continue to assist the growth in the wurtzite phase of the $\langle 0001 \rangle$ crystallographic direction and more layers are formed at the growth interface thereby elevating the Au ball. The growth rate is monitored with reflection high-energy electron diffraction (RHEED, see panel **a**).

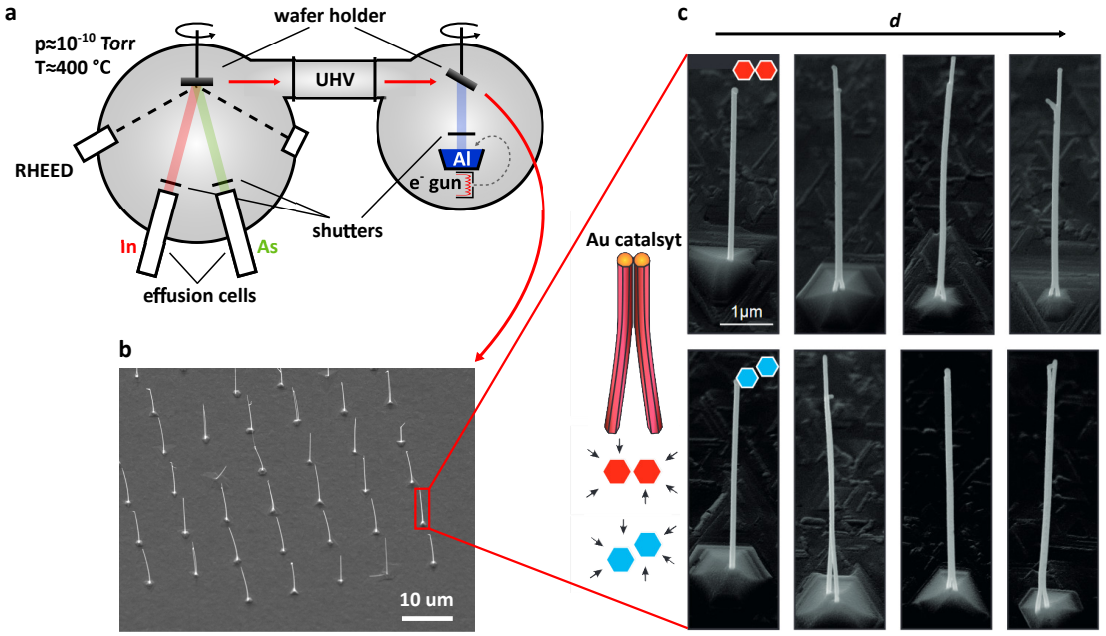

Figure 2.5.1: **Growth of parallel InAs nanowires with Al shell. a** Schematic of a MBE chamber with in-situ metal deposition. The In and As atoms coming from an effusian cells in a beam enter pre-defined Au catalyst on a wafer, where the nanowires are grown. The wafer is then transferred to another chamber without breaking the vacuum, where the Al is deposited by a slow e-beam evaporation. **b** SEM image of as-grown nanowires arranged in a square lattice. **c** High-resolution SEM of double nanowires with full-shell Al. Top row: edge-to-edge orientation, bottom row: facet-to-facet. The diameter of the nanowires increase from the left to the right.

After the InAs nanowires are grown, the substrate is rapidly transferred to the metallization chamber via a trolly rail without breaking the UHV (along the red arrows in panel **a**). The Al target is heated with an electron beam, which evaporates and precipitates on the wafer in angle. The deposition rate is kept as low as Al atoms can relax on the surface thereby matching the lattice of the InAs without any crystal defects. The slow rotation of the substrate allows the Al to cover the InAs selectively on the desired facets and thickness. In the experiments, we used nanowires with the Al covering either 2 facets (half-shell), or completely surrounding them (full-shell).

As a result of the growth, a batch of parallel InAs nanowires with Al shell is produced, with an example shown in Fig. 2.5.1**b**. By varying the size and the distance of the pre-defined Au droplets (even within a single wafer), the diameter and the spatial separation of the nanowires are engineered at will during the MBE. High-resolution SEM images of parallel nanowires with $\sim 20\,\text{nm}$ full-shell Al (a zoom of nanowires from panel **b**) are demonstrated in Fig. 2.5.1**c**. Due to the polygonal cross-section, even the orientation of the wires is maintained, i.e. whether the adjacent wires face each other by edge-to-edge (red) or facet-to-facet (blue) as shown in the top and bottom rows of panel **c**. Here the diameter of the nanowires, d, increases from the left column ($\sim 50\,\text{nm}$) to the right one ($\sim 90\,\text{nm}$). We note that these parameters are critical

regarding our double QD devices: if the seeds of the wires are too close to each other, they might merge during the growth constituting a single wire instead of a double one, whereas if the separation is too large, the thin Al layer does not connect them. In general, thinner wires are preferred for the experiments, however, they are prone to break in the manipulation process, and difficult to define the normal contacts during the EBL (see the next Subsection). Based on all of these constraints, we chose nanowires with $\sim 20\,\mathrm{nm}$ Al shell (half- or full-shell), a diameter of $\sim 80\,\mathrm{nm}$, and a final separation of $< 10\,\mathrm{nm}$ to build nanocircuits.

The nanowires are deposited onto a Si/SiO_2 substrate from the growth wafer with a micromanipulator built into an optical transfer microscope. The wires are extracted at their roots by a glass needle with a tip radius of a few 10 nm and laid on the substrate, where they can be roughly localized with high-magnification optical images.

2.5.2 Wet chemical etching & electron beam lithography

To realize the double QDs in the InAs, the Al shell has to be partially removed, which can be achieved by wet chemical etching. To etch the Al in a given geometry, the etchant (selective to the Al) has to access to the wires locally, while the rest of it has to be protected by a mask. Opening such etching windows is achieved by EBL, whose main steps are depicted in Fig. 2.5.2**a**. A resist layer composed of long-chain organic polymers is spin-coated to cover the substrate with a certain thickness (1). The resist is selectively exposed with a high-energy, focused electron beam along the designed patterns (2), which breaks the bonds of the organic chains and cuts them into smaller ones. The exposed resist is then dissolved with a developer (3), which leaves the unexposed area intact thereby creating the desired etching windows. The sample is then put into the etchant for the required time, which mostly depends on the type of the shell (half or full). As the final step of the etching, the masking layer is removed with an appropriate solvent. To check the quality of the etching and localize the nanowires with $< 10\,\mathrm{nm}$ precision, SEM imaging is performed. An example of Al etching in full-shell, parallel nanowires is demonstrated in Fig. 2.5.2**b**.

As the next step, one has to install the metallic electrodes to build the nanocircuits. EBL steps (1)-(3) from panel **a** are repeated with a high precision of alignment, which is followed by metallization (4). In UHV, the surface of the nanowires is cleaned by Ar plasma, which is followed by metal deposition. The target is heated by an electron beam until the metal evaporates and the atoms traveling toward the sample condense on the surface. As a result, the metal (pink in panel **a** step 4) covers the whole sample. The excess metal above the resist is lifted off by removing the masking layer (5), similar to the last step of the etching. The details of the fabrication (e.g. etching and electrode geometries, metal thickness, etc.) are different for each nanocircuit and experiment design (CPS, 2-atomic, and polyatomic Andreev molecule), which we mention in the appropriate Chapters and Appendix A.3. Once all the metallic electrodes are defined, the chips are glued and wire bonded to chip carriers or printed circuit boards (shown in Figs. 2.5.2**c-d**), which can be inserted in holders compatible with the low-temperature instrumentations.

2.5.3 Low-temperature instrumentation

Besides suppressing broadening effects from finite temperatures, the measurement of superconducting correlations requires a base temperature of $< 100\,\mathrm{mK}$ due to the $\sim 1\,\mathrm{K}$ critical temperature of the Al. Therefore we operated a dilution refrigerator to cool down all the samples presented in the rest of the thesis.

The desired ultra-low temperature is reached in a cryostat pre-cooled to 4 K with a pulse tube compressor[185] of He^4. The cryostat has two vacuum chambers, an outer vacuum chamber (OVC) serving as a temperature shielding, and an inner vaccum chamber (IVC), where to the

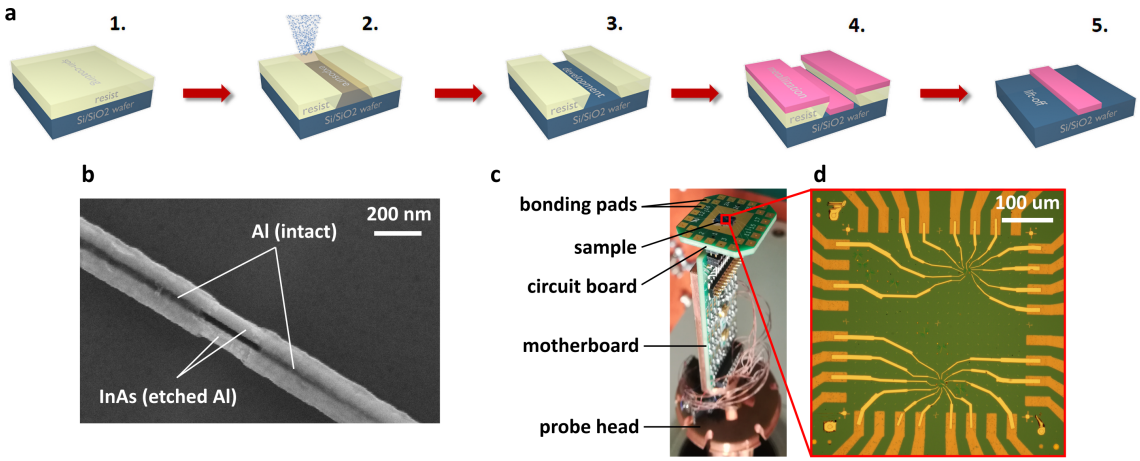

Figure 2.5.2: **Blocks of nanofabrication. a** Sketch of EBL steps. The spin-coated (1) resist is exposed partially (2), which is then dissolved (3) by a developer. The metal is deposited by e-beam evaporation (4). The residual metal is removed by the lift-off (5). **b** High-resolution SEM image of Al-etched full-shell InAs nanowires. In a $\sim 200\,\text{nm}$ window, the Al is eliminated by wet chemical etching. The etchant accessed the nanowires in a window opened in a mask by EBL (nominally 100 nm wide). **c** Sample holder head after bonding the chip to the circuit board. The chip is fixed by Ag epoxy. The cables go through the probe from the bonding pads via the motherboard to the probe top. **d** Optical image about the middle of the chip from panel **c**. The two nanowire devices with 9 contacts (light yellow) are connected to the outer bonding pads (dark yellow).

samples are loaded after pumping. The sample holder probes (main and side) are thermalized to metallic plates in the IVC, where there is a temperature gradient from the top ($\sim 3\,\text{K}$) to the mixing chamber ($\sim 10\,\text{mK}$) during operation, which we discuss next. The samples are placed in the bottom of the probes below the mixing chamber plate. The interior of the dilfridge is shown in Fig. 2.5.3**a**.

In the dilution refrigerator, such thermodynamic cycles are performed where the liquid He^3 and He^4 are diluted and separated in the circulation via a mixture line[185]. In the mixing, the He^3 is diluted in He^4 which drains heat from the environment due to the entropy production. It is possible because the spatial separation of He^3 in its pure phase is larger compared to He^4 (it also means that binding energy is smaller in case of pure He^3) resulting in a net cooling power. Nevertheless, He^3 has a finite solubility in He^4, therefore the equilibrium state has to be disturbed by extracting the He^3 circulating in the system. Considering the higher vapor pressure of He^3 compared to He^4, it can be pumped in a distiller (still). Although the more power is applied, the higher the circulation rate there is, the too high temperature in the still ends up with significant vapor pressure of He^4 decreasing the circulation efficiency. Pumping is also assisted by the gradient of the osmotic pressure created by the reduction of He^3 concentration. The temperature difference between the still and the returning He^3 to the mixing chamber is minimized by heat exchangers. The recovered He^3 is cleaned via liquid nitrogen traps and reenters the mixing chamber closing the cycle. The circulation is automatized and controlled by the gas handling system interface, which is illustrated in Fig. 2.5.3**b** with the circulation together. In practice, a standard 40 mK base temperature is reached. Additionally, superconducting magnets are also built in the cryostat, hence, a large magnetic field could be applied in different directions (see Fig. 2.5.3**a**).

Cables from the samples run up to the top of the probes via RC filters to minimize the acquired noise. The probe is connected to the electrical instruments with which the transport experiments are done. All measurements discussed in the following Chapters were performed by standard lock-in technique with the principle of phase-sensitive detection. While an AC voltage

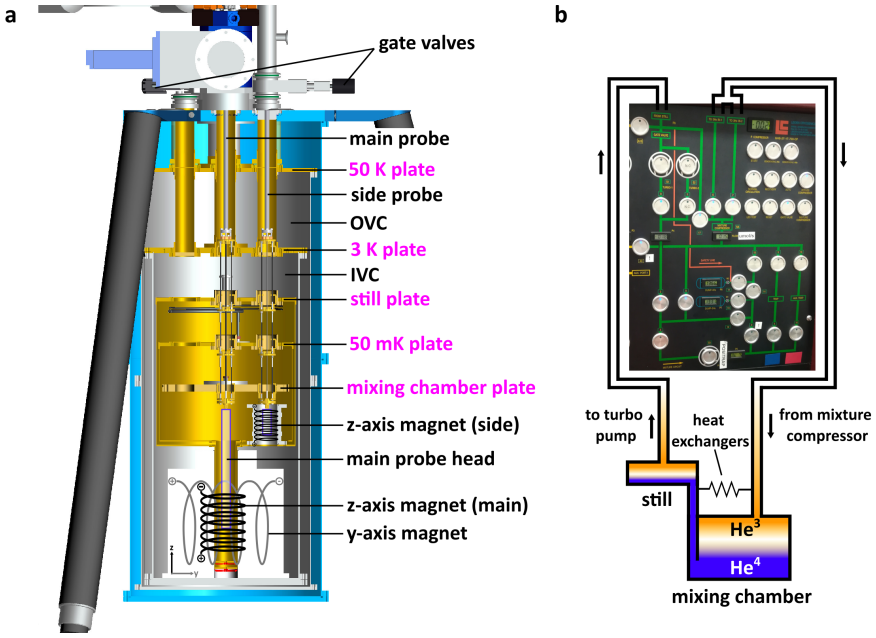

Figure 2.5.3: **Operation of a diluton refrigerator. a** Sketch of the dilfridge cryostat interior. The main and side probes are loaded into the IVC, while the OVC provides thermal shielding. The probes are thermalized to the dilfridge with direct contact to the metallic plates (highlighted in purple). The samples are aligned to the middle of superconducting solenoids (see the black and gray coils). **b** Illustration of He^3 circulation in the dilfridge. The He^3 (orange) enters the mixing chambers via the inlets, where it is mixed with He^4 (blue). It is then pumped via the still closing the loop. The photo shows the control panel of the gas handling system, where the green lines correspond to circulating tubes under vacuum.

(V_{AC}) with a driving frequency, $\mathcal{O}(\omega) = 100\,\text{Hz}$, is applied to the sample, the output current is multiplied with the input signal and its $\pi/2$ phase shifted one, and integrated over $\geq 10T = 10\frac{2\pi}{\omega}$ elapsed time. The integration averages out any current contribution, I, different in frequency from ω, thus the resistive (I_R) and capacitive or inductive (I_C) responses are given by

$$\begin{aligned} I_R &= \frac{1}{\tau}\int_0^{\tau\geq 10T} I(t)\sin(\omega t)dt \\ I_C &= \frac{1}{\tau}\int_0^{\tau\geq 10T} I(t)\sin\left(\omega t - \frac{\pi}{2}\right)dt, \end{aligned} \tag{2.5.1}$$

respectively. Differential conductance $G = dI/dV_{AC}$ was measured via I/V converters, on which the DC bias V_{SD} was adjusted by external voltage sources applied to them. The data collection was automatized with Python and Labview scripts.

By now we collected all the theoretical and technical background needed to explain our experiments and results, therefore we move to them in the next 3 Chapters.

Chapter 3

Cooper pair splitting with Coulomb repulsion

CPS is a strong indication of superconducting non-localities in electron transport[77,78,82]. To get control over this process, single-nanowire circuits have been realized with parallel QDs attached to a SC[84–89]. One primary limitation of the single-wire geometry is the finite distance between the QDs, δr, usually characterized by the superconducting electrode width (see Fig. 3.1.1**a**), which leads to an exponential decay of the CPS signal according to Eq. 2.2.26. One might expect the enhancement of CPS in an arrangement, where the two points the split electrons are injected into the parallel QDs are brought substantially closer to each other (see Figs. 3.1.1**b**)[82,98]. Parallel InAs nanowires satisfy this criterium, therefore they are promising platforms for CPS experiments as promoted earlier.

As outlined in Subsection 2.2.3, with minimizing δr the inter-dot Coulomb repulsion (U_{LR}) also takes a non-negligible measure (see Fig. 3.1.1**b**). Although previous theoretical works have investigated the mechanism of CPS in parallel double QD systems, they either neglected the impact of the inter-dot capacitance,[186–188] or focused on the regime of strong coupling to the SC (Andreev limit)[57,99,103–106,111,112,114,115,123,124], the opposite of what is desired for CPS[82,95]. Along with the idea, CPS has been examined in individual nanowires placed manually next to each other and connected via an ex-situ deposited Al contact[97,189]. Nevertheless, beyond those devices lacked the high-quality SC-semiconductor coupling expected from a minimal Kitaev block in the future, the effect of the Coulomb-repulsion has not been addressed by any means.

In this Chapter, we report a significant CPS signal observed in parallel InAs nanowires with an epitaxial Al layer. We discuss the CPS through a parallel double QD system and estimate the relative reduction of its efficiency in the presence of finite inter-dot Coulomb repulsion energy, U_{M}. Despite the strength of this capacitive coupling being comparable to the superconducting gap, Δ in our experiments, we report a higher splitting efficiency than in most preceding experiments performed in InAs nanowires. Our findings demonstrate that double nanowires with epitaxial SC are ideal for further applications[1], where the dominance of CAR is needed[152–154]. The results presented here cover the contents of Ref. 190.

[1]The sample fabrication, the measurements, and the data analysis were performed by Olivér Kürtössy. The theoretical model was developed by Dr. Zoltál Scherübl. The project was guided by Dr. Péter Makk and Dr. Szabolcs Csonka.

3.1 Device outline

The system studied here is illustrated in Figs. 3.1.1**b-e** and we shortly discuss the steps of the fabrication. Pairs of parallel InAs nanowires were grown in close vicinity as discussed in Section 2.5 and Ref. 179 (see panel **c**). An epitaxial Al layer was deposited in situ (blue in panels **d-e**) merging them by covering 2 facets as displayed by a transmission electron microscopy (TEM) image in the top right of Fig. 3.1.1**c**. After transferring a pair of wires to a substrate, the Al was partially removed from them (brown) by using a wet etch method[179] (for details, see Appendix A.3).

The most challenging part of the fabrication process was to define the two normal metal leads (Ti/Au, yellow in Fig. 3.1.1**d**) such that a single electrode contacts only one of the wires, which was necessary to measure the current in both wires independently. A further requirement from this geometry was to align these electrodes to the same distance from the SC, i.e. face to face to each other to avoid any possible asymmetry in the transport. These constraints demanded a $< 30\,\mathrm{nm}$ precision in the positioning and $\sim 80\,\mathrm{nm}$ gap between the metallic contacts. Similarly high accuracy was required to realize 3-3 side gate electrodes to create QDs electrostatically in each of the wires. To achieve $\sim 100\,\mathrm{nm}$ separation between the tip of the finger gates and $\sim 40\,\mathrm{nm}$ distance from the wires, they were defined in a different EBL step with a thinner metal layer deposited ($\sim 35\,\mathrm{nm}$) compared to the contacts ($\sim 90\,\mathrm{nm}$). After a post-selection among the devices with the defined contacts and gate electrodes in SEM, a third normal contact was evaporated on the epitaxial SC (see Fig. 3.1.1**e**) with a distance of $\sim 2\,\mu\mathrm{m}$ measured from the border of the etching. We note that this length exceeds the superconducting coherence length of the Al (ξ). In the same EBL round the metallic leads of the devices were connected with the bonding pads (visible in Fig. 2.5.2**d**). We optimized the fabrication process for this circuit structure, whose recipe is found in Appendix A.3. In total, ~ 40 chips with 2-3 samples on each were fabricated, a couple of them were studied at low temperature, and the one presented in Fig. 3.1.1**d** was characterized thoroughly regarding CPS. Another troublesome side of the double wires was to find the ideal seed separation and diameter of them. The wires grown far from each other were disconnected, while the very close ones had a finite coupling via the InAs which we wanted to exclude. To overcome the latter problem we only picked nanowires with specific grown parameters from the wafer and the devices were tested at room temperature to sort out the possible shorts between the nanowires.

With the described fabrication method, we obtained parallel SC-QD-N junctions with a joint SC (N stands for normal metal, see Fig. 3.1.1**e**). The sample was cooled down in a dilution refrigerator to a base temperature of 40 mK where the electronic transport measurements were carried out. Tunnel barriers were formed by adjusting the voltage on the outer side gates. If the coupling of the QDs is stronger to the SC than to the normal leads, sub-gap states can be formed and one enters the Andreev limit[99,103–106,111,112,114,115]. In our case, the tunnel barriers were set such that the opposite limit was reached, where the normal leads were coupled strongly. This allowed the QDs to be emptied rapidly without blocking the transport, hence making it suitable to investigate CPS[82,95]. The middle finger gate electrodes served as plunger gates to tune the level position of the left (red) and right (green) QDs by V_L and V_R, respectively (see Fig. 3.1.1**e**). Differential conductance $G_\mathrm{L} = dI_\mathrm{L}/dV_\mathrm{AC}$ and $G_\mathrm{R} = dI_\mathrm{R}/dV_\mathrm{AC}$ through the left and right QDs were recorded on the normal contacts biased by V_SD applied on the offset inputs of home-built I/V converters. With this geometry, we minimized δr to boost the superconducting inter-dot correlations as suggested in Refs. 82 and 98, since the CPS current (ΔI, discussed previously at Eq. 2.2.26) is suppressed as:

$$\Delta I \propto e^{\frac{-2\delta r}{\pi\xi}}, \tag{3.1.1}$$

however, we also introduced a finite U_LR at the same time, as shown in Fig. 3.1.1**b**.

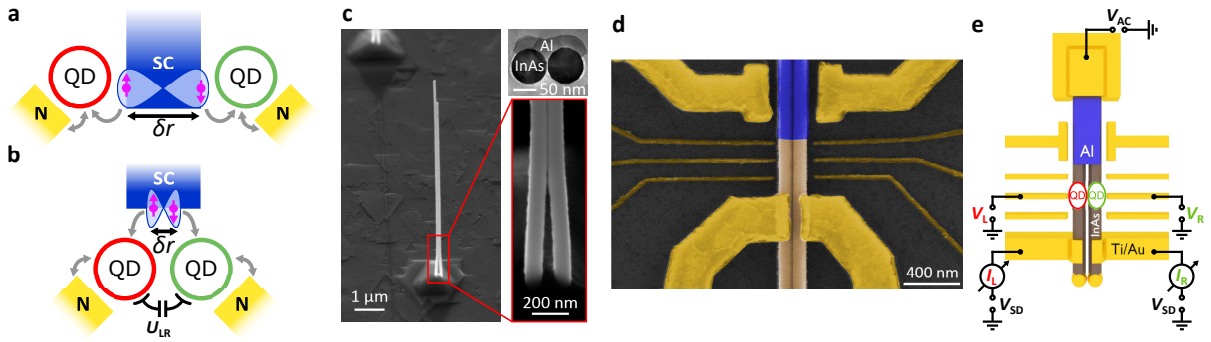

Figure 3.1.1: **Device outline.** **a** Concept of a single-nanowire-based Cooper pair splitter. The lower bound for δr is the width of the SC with negligible cross capacitance between the QDs. **b** Same as panel **a**, but in double, parallel nanowires. While δr can be minimized, U_{LR} becomes significant. **c** High-resolution SEM micrographs of the as-grown nanowires imaged from the opposite side of the Al covering. A TEM image on the top shows the cross-section of the material with the Al connecting the two InAs wires. **d** False-colored SEM image of the device. The epitaxial Al (blue) was etched away from half of the InAs nanowires (brown). Two separate and one shared Ti/Au contacts and side gate electrodes (yellow) were evaporated to control the transport. **e** Schematic illustration of the measurement setup. The left (red) and right (green) QDs were tuned by V_{L} and V_{R}, respectively, and were biased simultaneously by V_{SD}. The currents in the two arms were measured via I/V converters, yielding the differential conductance G_{L} and G_{R}.

3.2 Experiments

In the following, we discuss the spectrum of the created double QD system. Figs. 3.2.1**a-b** show the zero-bias conductance of the left and right QDs, respectively, as a function of the two plunger gate voltages in the normal state reached by a $B = 250\,\mathrm{mT}$ out-of-plane magnetic field. The finite slopes of the lines are attributed to the capacitance between the left (right) plunger gate and the right (left) QD. The resonance lines of each QD shift in the phase diagram when the other one is being charged (or discharged) due to the significant inter-dot Coulomb repulsion, resulting in an effective gating and exhibiting a honeycomb pattern, which we discussed in the theory of double QDs in Fig. 2.1.4[65]. Figs. 3.2.1**c-d** show normal-state finite-bias spectroscopy of the left and right QDs performed along the white and gray dotted line in Figs. 3.2.1**a-b**, while Figs. 3.2.1**e-f** show the same measurements in the superconducting state ($B = 0$).

The charging energies of the left and right QDs were extracted from the size of the Coulomb diamonds as $U_{\mathrm{L}} = 0.9\,\mathrm{meV}$ and $U_{\mathrm{R}} = 0.7\,\mathrm{meV}$, while the total couplings of the QDs were estimated from the level broadenings as $\Gamma_{\mathrm{L}} \approx 0.28\,\mathrm{meV}$ and $\Gamma_{\mathrm{R}} \approx 0.45\,\mathrm{meV}$, respectively. Here $\Gamma_{\mathrm{L(R)}} = \Gamma_{\mathrm{SL(R)}} + \Gamma_{\mathrm{NL(R)}}$ and $\Gamma_{\mathrm{SL(R)}}$ describes the tunnel rate between the SC and the left(right) QD, while $\Gamma_{\mathrm{NL(R)}}$ is the tunnel rate between the left (right) QD and the normal lead. The level broadening was extracted from a fitted Lorentzian curve of the Coulomb resonances as recommended by Eq. 2.1.16. The strength of the inter-dot Coulomb repulsion was found to be $U_{\mathrm{LR}} = 0.15\,\mathrm{meV}$ estimated from the relative shift of the resonance lines in Figs. 3.2.1**a-b**[65]. As the relative shift of the left (right) QD resonance in gate voltage is $m_{\mathrm{L(R)}} = \delta V_{\mathrm{L(R)}}/V_{\mathrm{L(R)}}$, the conversion of $U_{\mathrm{LR}} = U_{\mathrm{L(R)}} m_{\mathrm{L(R)}}$ has been used with regard of Eq. 2.1.19.

In Figs. 3.2.1**e-f** the Coulomb resonances split up at zero bias and a soft gap opens with 2Δ energy in the excitation spectra (with $\Delta \approx 0.15\,\mathrm{meV}$), typical for SC-QD-N junctions. The tip of the diamonds also shifts in gate voltage and the lack of sub-gap states confirms the weak coupling towards the SC ($\Gamma_{\mathrm{SL(R)}} \ll \Gamma_{\mathrm{NL(R)}}$), needed for CPS experiments.

Let us now explore the zero-bias conductance of the QDs from Figs. 3.2.1**a-b**, but in the superconducting state. The corresponding charge stability maps are shown in Figs. 3.2.2**a-**

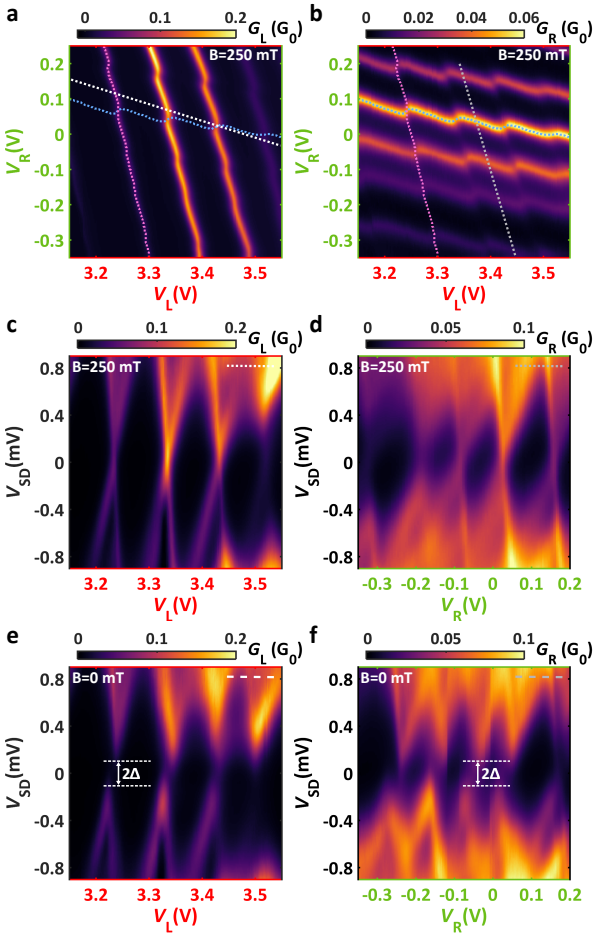

Figure 3.2.1: **QD characterization. a-b** Zero-bias stability maps of the left and right QDs in the normal state. The finite capacitance between the plunger gates to the opposite QDs with the strong inter-dot Coulomb repulsion establishes a honeycomb structure in the phase diagram. **c-d** Bias spectroscopy of the left and right QDs in the normal state and **e-f** in the superconducting state along the white and gray dotted lines in panels **a-b**. $U_{\mathrm{LR}} = 0.15\,\mathrm{meV}$ was read off from the phase diagram, while charging energies of the left and right QDs were extracted as $U_{\mathrm{L}} = 0.9\,\mathrm{meV}$ and $U_{\mathrm{R}} = 0.7\,\mathrm{meV}$, respectively, with $\Delta = 0.15\,\mathrm{meV}$ from the Coulomb-blockade spectroscopy. The couplings were estimated to be $\Gamma_{\mathrm{L}} \approx 0.28\,\mathrm{meV}$ and $\Gamma_{\mathrm{R}} \approx 0.45\,\mathrm{meV}$.

b. Here the conductance of both QDs is smaller globally compared to Figs. 3.2.1**a-b**, but non-zero due to the presence of the soft gap. In contrast to the normal-state data where the capacitive cross-talk yields minima at the intersections of the left and right QD resonances, in the superconducting state, maxima develop instead. These are manifested in Fig. 3.2.2**b** by the yellow spots at the shifting resonance lines. To prove that CPS takes place in our system and to quantify its efficiency, we focus on the evolution of the signal amplitudes along single resonance lines. In Fig. 3.2.2**c** G_{L} and G_{R} are plotted along a resonance of the right QD, whose trace is depicted with the blue dashed line in Figs. 3.2.2**a-b**. The red curve shows the resonances of the left QD, and we call this signal "local", whereas the green one shows the changes in the conductance of the right QD as a function of V_{L}, hence we denote this as the "non-local" signal. Although G_{R} is always maximal along this cut, well-pronounced peaks emerge when the left QD is also brought to resonance. Similarly, in Fig. 3.2.2**d**, where the roles of QDs are interchanged, G_{L} and G_{R} are demonstrated along the pink dashed line from Figs. 3.2.2**a-b**. Here one can see a significant increase in the left QD signal when the right QD becomes resonant as well. For example, the non-local peaks at $V_{\mathrm{L}} = 3.24\,\mathrm{V}$ and $V_{\mathrm{R}} = 0.07\,\mathrm{V}$ can be recognized in both QD signals in Figs. 3.2.2**c-d** with the equal height of ΔG indicated by the black arrows.

These non-local maxima vanish by switching off the superconductivity as shown in Fig. 3.2.2**e-f**, where the same analysis was carried out as in Figs. 3.2.2**c-d** but in the normal state along the blue and pink dotted lines in Figs. 3.2.1**a-b**. In the absence of superconductivity, the overall conductivity increases, and the non-local peaks are replaced by dips. These features are robust along each resonance in Fig. 3.2.1**a-b** (the anyalysis of another pair of resonances can be found in Appendix A.2). We emphasize that the dips are much deeper than what is expected from resistive cross-talk introduced in Ref. 84, and they are caused by the finite inter-dot capacitance, which penalizes the simultaneous electron occupation of the adjacent QDs. The strong positive correlation only existing in the superconducting state demonstrates the presence of robust CPS.

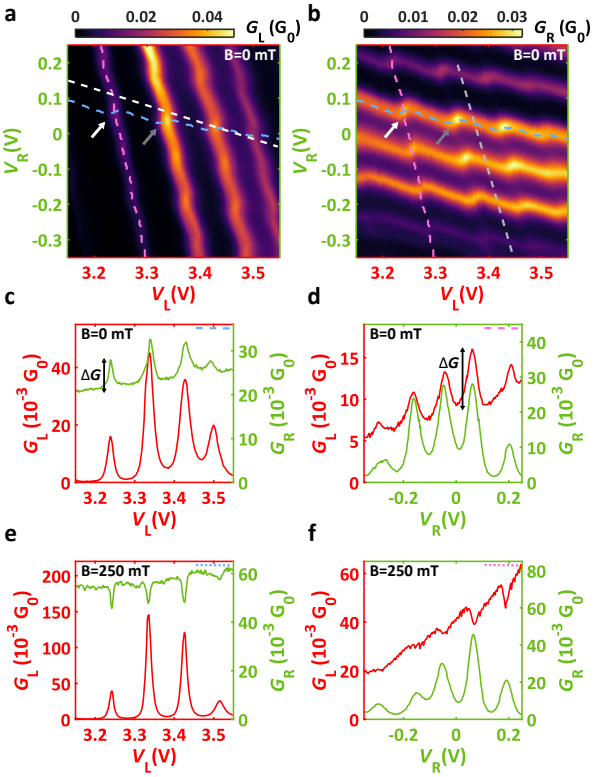

Figure 3.2.2: **CPS validation.** **a-b** Same gate stability maps as in Figs. 3.2.1**a-b**, but in the superconducting state. The white and gray arrows show the spots with the maximal splitting efficiency and maximal visibility of the non-local signal, respectively. **c** Conductance along a selected resonance of the right QD indicated by the blue dashed line in panels **a-b**. There is a strong positive correlation between G_{L} and G_{R}. **d** Similar cut to panel **c**, but along a resonance of the left QD shown by the pink dashed line in panels **a-b**. The peaks at $V_{\mathrm{L}} = 3.24\,\mathrm{V}$ match the one at $V_{\mathrm{R}} = 0.07\,\mathrm{V}$ in panel **c** with the same amplitude of ΔG. **e-f** Normal state data of the corresponding cuts in panels **c-d** (taken along the pink and blue dotted lines in Figs. 3.2.1**a-b**). Once the superconductivity is suppressed by an external magnetic field, negative correlations overtake the non-local peaks arising from the non-negligible U_{LR}.

3.2.1 Quantification of the splitting efficiency

Following Eqs. 2.2.28 and 2.2.29, the CPS efficiency can be defined as $s = 2\Delta G/(G_{\mathrm{L}} + G_{\mathrm{R}})$, while visibility of the non-local signal in the left (right) QD is $\eta_{\mathrm{L(R)}} = \Delta G/G_{\mathrm{L(R)}}$, where ΔG is the non-local signal amplitude equal in the two wires (see Figs. 3.2.2**c-d**)[84,87,96,97]. We estimated the maximal and average CPS efficiency as $s_{\max} = 29$-36% (see the white arrow in Figs. 3.2.2**a-b**) and $\overline{s} = 19$-28% in the investigated gate range, respectively. The maximal visibility was found to be $\eta_{\mathrm{L,max}} = 40$-$49\%$ and $\eta_{\mathrm{R,max}} = 29$-$40\%$ (see the gray arrow in Figs. 3.2.2**a-b**). The lower bounds of the given ranges are derived as ΔG being measured from the baseline of the resonances. More realistic estimates (used here as upper bounds) are calculated by considering the relative reduction of the conductance usually reaching 15% (see Figs. 3.2.2**e-f**), which is

always present in the system as it comes from the capacitive coupling. In this case, the CPS signals are estimated by the sum of the previously described ΔG and the expected depth of the dips in the QD with smaller average conductance in the superconducting state. Here the condition of the non-local signals being equal in G_{L} and G_{R} is still satisfied, however, these numbers could even increase ($s_{\max} = 45\%$, $\eta_{\mathrm{L,max}} = 60\%$ and $\eta_{\mathrm{R,max}} = 70\%$) if one takes into account higher-order processes, where the electrons of a Cooper pair split into different QDs finally leave to the same electrode[87,178]. We emphasize that these numbers are much higher than in previous measurements performed on single InAs nanowire-based CPS experiments[84,86], which is attributed to the short δr. In the following, we explore the relative reduction of these quantities caused by the Coulomb interaction between the QDs.

3.3 Discussion

Let us analyze of how a finite U_{LR} influence the CPS. During the pair splitting, an electron jumps from the SC to the left (right) QD, while the second electron tries entering the right (left) QD. The presence of the first electron increases the energy of the unoccupied QD by U_{LR}, therefore its filling with the second electron is penalized by U_{LR} quenching the CPS and any other transport processes where both QDs are being charged simultaneously. To confirm this assumption and quantify this effect, we developed a rate equation model to calculate the relative CPS currents in parallel QDs at different electron occupations.

3.3.1 Modeling

In our model, the QDs are treated as single sites in the frame of the Anderson model with $\delta r = 0$ geometrical separation allowing the electron numbers to be 0, 1, or 2 in each QD, in accordance with 2.1.18[55]. The SC and the normal leads are handled by individual sites that electrons can occupy with any wavenumber $\mathbf{k}$ yielding BCS DOS and Fermi distributions, respectively. All tunnel couplings are assumed to be weak compared to the governing energy scales ($U_{\mathrm{L(R)}}$, Δ)[187], and the transport is entirely described by transition rates determined by 4th order perturbation theory with Fermi's golden rule[94]. We use the notation $|j,k,l,m,n\rangle = |j\rangle_{\mathrm{NL}} \otimes |k\rangle_{\mathrm{L}} \otimes |l\rangle_{\mathrm{SC}} \otimes |m\rangle_{\mathrm{R}} \otimes |n\rangle_{\mathrm{NR}}$ to where $j,n = \{FS,\uparrow,\downarrow,2\}$, $k,m = \{0,\uparrow,\downarrow,2\}$, and $l = \{GS,\uparrow,\downarrow,2\}$ to describe the ground state electron filling in the left and right normal leads, the left and right QDs, and the SC, respectively. FS refer to the Fermi-sea, while GS indicates the BCS ground states with no quasi-particles. With this labeling, one can track electron occupations and the electron movements in the system. The net current in the left (right) lead is obtained by solving the classical master equation in the stationary limit. The sketch of the model is shown in Fig. 3.3.1.

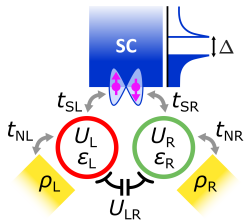

Figure 3.3.1: **Schematic of the model.** The QDs are modeled as single sites with charging energies U_{L}, U_{R}, on-site energies ε_{L}, ε_{R}, and inter-dot Coulomb repulsion U_{LR} between them. Couplings to the SC (t_{SL}, t_{SR}) and to the normal leads (t_{NL}, t_{NR}) are treated perturbatively. In the calculations, the SC with a gap of Δ is handled with a BCS DOS, while the leads are considered as Fermi-seas with ρ_{L}, ρ_{R}.

Let us now look at the model more quantitatively. The Hamiltonians read as:

$$H = \underbrace{H_{\mathrm{SC}} + H_{\mathrm{DQD}}}_{H_0} + \underbrace{H_{\mathrm{NL}} + H_{\mathrm{NR}}}_{H_{\mathrm{N}}} + \underbrace{H_{\mathrm{TSL}} + H_{\mathrm{TSR}} + H_{\mathrm{TNL}} + H_{\mathrm{TNR}}}_{H_{\mathrm{T}}}. \tag{3.3.1}$$

Here H_0 consists of the BCS mean-field Hamiltonian of the SC and the double-QD Andreson term. H_{N} describes the normal leads as Fermi-seas, while H_{TL} expresses the tunnel couplings of the QDs to the SC and the normal leads. They are constructed as

$$\begin{aligned}
H_{\mathrm{SC}} &= \sum_{k\sigma} \varepsilon_{\mathrm{S}k} c^{\dagger}_{\mathrm{S}k\sigma} c_{\mathrm{S}k\sigma} + \Delta \sum_{k} \left(c^{\dagger}_{\mathrm{S}k\uparrow} c^{\dagger}_{\mathrm{S}-k\downarrow} + c_{\mathrm{S}-k\downarrow} c_{\mathrm{S}k\uparrow} \right) = \sum_{k\sigma} E_k \gamma^{\dagger}_{k\sigma} \gamma_{k\sigma} \\
H_{\mathrm{DQD}} &= \sum_{\alpha} \left(\sum_{\sigma} \varepsilon_{\alpha} n_{\alpha\sigma} + U_{\alpha} n_{\alpha\uparrow} n_{\alpha\downarrow} \right) + U_{\mathrm{LR}} n_{\mathrm{L}} n_{\mathrm{R}} \\
H_{\mathrm{NL}} &= \sum_{k\sigma} \varepsilon_{\mathrm{NL}k} c^{\dagger}_{\mathrm{L}k\sigma} c_{\mathrm{L}k\sigma} \\
H_{\mathrm{NR}} &= \sum_{k\sigma} \varepsilon_{\mathrm{NR}k} c^{\dagger}_{\mathrm{R}k\sigma} c_{\mathrm{R}k\sigma} \\
H_{\mathrm{TSL}} &= \sum_{k\sigma} t_{\mathrm{SL}} \left(c^{\dagger}_{\mathrm{S}k\sigma} d_{\mathrm{L}\sigma} + d^{\dagger}_{\mathrm{L}\sigma} c_{\mathrm{S}k\sigma} \right) \\
&= \sum_{k\sigma} t_{\mathrm{SL}} \left(\left(u_k \gamma^{\dagger}_{k\sigma} - \sigma v_k \gamma_{-k\bar{\sigma}} \right) d_{\mathrm{L}\sigma} + d^{\dagger}_{\mathrm{L}\sigma} \left(u_k \gamma_{k\sigma} - \sigma v_k \gamma^{\dagger}_{-k\bar{\sigma}} \right) \right) \\
H_{\mathrm{TSR}} &= \sum_{k\sigma} t_{\mathrm{SR}} \left(c^{\dagger}_{\mathrm{S}k\sigma} d_{\mathrm{R}\sigma} + d^{\dagger}_{\mathrm{R}\sigma} c_{\mathrm{S}k\sigma} \right) \\
&= \sum_{k\sigma} t_{\mathrm{SR}} \left(\left(u_k \gamma^{\dagger}_{k\sigma} - \sigma v_k \gamma_{-k\bar{\sigma}} \right) d_{\mathrm{R}\sigma} + d^{\dagger}_{\mathrm{R}\sigma} \left(u_k \gamma_{k\sigma} - \sigma v_k \gamma^{\dagger}_{-k\bar{\sigma}} \right) \right) \\
H_{\mathrm{TNL}} &= \sum_{k\sigma} t_{\mathrm{NL}} \left(c^{\dagger}_{\mathrm{L}k\sigma} d_{\mathrm{L}\sigma} + d^{\dagger}_{\mathrm{L}\sigma} c_{\mathrm{L}k\sigma} \right) \\
H_{\mathrm{TNR}} &= \sum_{k\sigma} t_{\mathrm{NR}} \left(c^{\dagger}_{\mathrm{R}k\sigma} d_{\mathrm{R}\sigma} + d^{\dagger}_{\mathrm{R}\sigma} c_{\mathrm{R}k\sigma} \right).
\end{aligned} \tag{3.3.2}$$

Here $n_{\alpha\sigma} = d^{\dagger}_{\alpha\sigma} d_{\alpha\sigma}$ is the number of electrons with spin σ on QD_{α}, with $d^{(\dagger)}_{\alpha\sigma}$ being the annihilation (creation) operator of electrons with spin σ on QD_{α} and $\alpha = \mathrm{L,R}$ denotes the left, right QD. Similarly, $c^{(\dagger)}_{\mathrm{S}k\sigma}$ and $c^{(\dagger)}_{\mathrm{L(R)}k\sigma}$ are the annihilation (creation) operator of electrons on the SC and the left (right) Fermi-seas with momentum k and spin σ, respectively. $t_{\mathrm{SL(R)}}$ and $t_{\mathrm{NL(R)}}$ are the hopping amplitude of the left (right) QD to the SC and the left (right) QD to the left (right) normal leads, respectively. In the calculations $U_{\mathrm{L}} = U_{\mathrm{R}} = 1\,\mathrm{meV}$, and $\Delta = 0.15\,\mathrm{meV}$ were used roughly matching the experimental values. All hopping amplitudes were chosen as $t_{\mathrm{SL(R)}} = t_{\mathrm{NL(R)}} = 0.01\,\mathrm{meV}$. By applying a Bogoliubov-transformation [70,122]:

$$c_{k\sigma} = u_k \gamma_{k\sigma} - \sigma v_k \gamma^{\dagger}_{k\bar{\sigma}}, \tag{3.3.3}$$

where $|u_k|^2 + |v_k|^2 = 1$, H_0 becomes diagonal.

Since the current is driven from the SC towards the leads, we are interested in sequences of events, where 2 extra electrons are created in any of the normal leads with momentum k and k' at the end of a transport cycle. Formally, transitions between the eigenstates of $H_0 + H_{\mathrm{N}}$ are induced by H_{T}. We distinguish LPT and CPS in the calculations. A sequence of electron

tunnelings is treated as LPT if the electrons constituting the Cooper pair leave the SC to the same QD, while the transport is considered to be CPS if the split electrons exit to separate QDs. However, various transport processes are allowed depending on the initial QD occupations, i.e. the on-site energy settings, $\varepsilon_R, \varepsilon_L$.

As an example, let us examine the relevant transport processes starting from the $|FS, \uparrow, GS, 0, FS\rangle$ state along the degeneracy line of $|FS, 1, GS, 0, FS\rangle$ and $|FS, 0, GS, 1, FS\rangle$ sectors. In this case, 8 final states are accessible with different spin configurations distributed on the QDs and on the leads, which are listed in Table 3.1. These states can be categorized either as a result of LPT or CPS relying on whether the split electrons leave the SC towards the same or separate QDs, respectively. 1 LPT process and 3 precedent processes titled CPS with distinct outcomes are demonstrated in Fig. 3.3.2, where the order of the events in the sequence is indicated by black arrows and numbers.

final state	process
$\|2, \uparrow, GS, 0, FS\rangle$	LPT (depicted)
$\|FS, \uparrow, GS, 0, 2\rangle$	LPT
$\|\uparrow, \uparrow, GS, 0, \downarrow\rangle$	CPS (**I.**)
$\|\downarrow, \uparrow, GS, 0, \uparrow\rangle$	CPS
$\|\uparrow, 0, GS, \uparrow, \downarrow\rangle$	CPS
$\|2, 0, GS, \uparrow, FS\rangle$	CPS ("singlet", **II.**)
$\|\uparrow, \downarrow, GS, 0, \uparrow\rangle$	CPS ("triplet", **III.**)
$\|\uparrow, 0, GS, \downarrow, \uparrow\rangle$	CPS ("triplet")

Table 3.1: **Table of possible transport processes.** List of possible final states of a transport cycle starting from $|FS, \uparrow, GS, 0, FS\rangle$. 3 sequences titled CPS with different final spin configurations are depicted in Fig. 3.3.2.

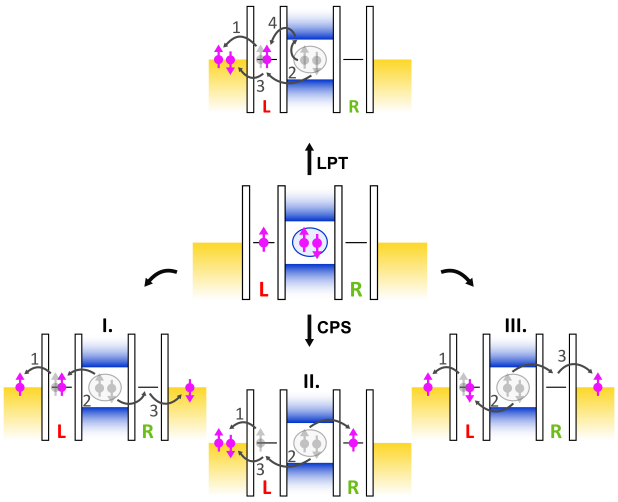

Figure 3.3.2: **CPS and LPT processes.** Transport cycles with the same initial, but different final states. The arrows with the numbers indicate the event order in the sequence. Electrons in gray symbolize the initial occupations, while the purple ones belong to the final states. At the top, a LPT, and at the bottom, 3 CPS processes are depicted. Although they are considered as CPS, in scenario **II.** in a common lead a spin singlet, in scenario **III.** in separate leads a triplet is created.

In all depicted transport cycles, the sequence starts with a single electron jumping from the left QD to the normal lead followed by splitting a Cooper-pair, but the final states deviate due to the different spin tunnelings. In scenario **I.**, the QDs have the same characters in the initial and final states, and electrons with opposite spins appear in separate leads at the end of the cycle, as in a regular CPS. In scenario **II.**, the split electrons tunneling to the QDs have the opposite spins compared to the one in **I.**. In this particular case, the opposite spins in the left arm originate from different Cooper pairs unlike in LPT and the final state is $|\uparrow\downarrow, 0, GS, \uparrow, FS\rangle$. We note that despite a singlet-like state being formed in the left lead, the right QD with an electron stuck there can be emptied in the following transport cycle effectively providing an ordinary CPS. Scenario **III.** resembles **II.**, nevertheless, double tunneling occurs on the right QD instead of the left one bringing the system into $|\uparrow, \downarrow, GS, 0, \uparrow\rangle$. Surprisingly, two electrons with the same spins are established in the two Fermi-seas, but the transport is still considered as CPS regarding the fact that electrons tunnel to separate QDs from the SC.

Once the corresponding transport cycles are sorted out, one can calculate the transition rates between the initial and final states in question. Technically two different schemes are possible: either both QDs are in blockade, or at least one of them is in resonance with the normal lead. In the former case, all intermediate states are virtual and the transport mechanisms are 4th order processes. Transition rates can be expressed by 4th order perturbation theory using Fermi's golden rule[94]:

$$w_{fi}^{(4)} = \frac{2\pi}{\hbar}\left|\sum_{pqr}\frac{\langle f|\,H_{\mathrm{T}}\,|r\rangle\,\langle r|\,H_{\mathrm{T}}\,|q\rangle\,\langle q|\,H_{\mathrm{T}}\,|p\rangle\,\langle p|\,H_{\mathrm{T}}\,|i\rangle}{\left(E_i-E_p\right)\left(E_i-E_q\right)\left(E_i-E_r\right)}\right|^2\delta\left(E_f-E_i\right), \tag{3.3.4}$$

where i and f stand for the initial and final states, respectively, and E_α denotes the total energy of the state $|\alpha\rangle$ ($\alpha=\{i,j,p,q,r\}$).

However, in the latter case, e.g. in the triple points, the transport cycles are composed of a sequential combination of 1st and 3rd-order elementary processes:

$$\begin{aligned} w_{fi}^{(3)} &= \frac{2\pi}{\hbar}\left|\sum_{pq}\frac{\langle f|\,H_{\mathrm{T}}\,|q\rangle\,\langle q|\,H_{\mathrm{T}}\,|p\rangle\,\langle p|\,H_{\mathrm{T}}\,|i\rangle}{\left(E_i-E_p\right)\left(E_i-E_q\right)}\right|^2\delta\left(E_f-E_i\right), \\ w_{fi}^{(1)} &= \frac{2\pi}{\hbar}\left|\langle f|\,H_{\mathrm{T}}\,|i\rangle\right|^2\delta\left(E_f-E_i\right). \end{aligned} \tag{3.3.5}$$

Processes depicted in Fig. 3.3.2 are such examples, where the first electron tunneling from the left QD to the lead (1) is a 1st order process. The pair splitting inside the SC and the rest of the tunneling events (2, 3) make up a 3rd order process, and the transition rate in question becomes the sum of $w_{fi}^{(1)}$ and $w_{fi}^{(3)}$. So far we only considered the transition rates of creating electrons with a specific k and k' momentum. To obtain the total transition rates one has to sum up all possible states available in the normal leads. In a 1st or 3rd order process, one can derive them as:

$$W_{fi}^{(1-3)}=\sum_k w_{fi}^{(1-3)}=\int d\xi\rho_{\mathrm{L(R)}}(\xi)w_{fi}^{(1-3)}(\xi), \tag{3.3.6}$$

where $\rho_{\mathrm{L(R)}}$ is the DOS of the left (right) lead considered to be constant ($T=0$ temperature is assumed). According to Eq. 3.3.5, $w_{fi}^{(1-3)}\propto\delta(E_f-E_i)$, therefore

$$W_{fi}^{(1-3)}\propto\int d\xi\rho_{\mathrm{L(R)}}(\xi)\delta(\xi)=\rho_{\mathrm{L(R)}}(0). \tag{3.3.7}$$

Similarly, in a 4th order process (see Eq. 3.3.4) the total transition rates read as:

$$W_{fi}^{(4)}=\sum_{kk'}w_{fi}^{(4)}=\int d\xi\rho_\alpha(\xi)\int d\xi'\rho_\beta(\xi')w_{fi}^{(4)}(\xi,\xi'), \tag{3.3.8}$$

where $\alpha,\beta=\{\mathrm{L},\mathrm{R}\}$. 4th order transition rates of any LPT or CPS creating electrons in the leads with momentum k and k' are proportional to a small bias, which was assumed to be

$V_{\mathrm{AC}} = 10\,\mu\mathrm{V}$, in agreement with the experiments:

$$W_{fi}^{(4)} \propto \int d\xi \rho_\alpha(\xi) \int d\xi' \rho_\beta(\xi') \delta(\xi + \xi') = \int d\xi \rho_\alpha(\xi) \rho_\beta(-\xi) = \rho_\alpha(0)\rho_\beta(0) V_{\mathrm{AC}}. \tag{3.3.9}$$

Based on the corresponding transition rates, one can solve the classical master equation in the stationary limit:

$$\frac{dP_q}{dt} = 0 = \sum_{p \neq q} \left(W_{qp} P_p - W_{pq} P_q \right), \tag{3.3.10}$$

where P_q is the occupation of the state $|q\rangle$ with the constriction of $\sum_q P_q = 1$. As LPT creates 2 electrons in either the left or the right lead and CPS does 1-1 in both of them, the total current in the left (right) normal lead is:

$$I_{\mathrm{L(R)}} = \frac{e}{\hbar} \sum_{pq} \left(2 \cdot W_{qp}^{\mathrm{LPT,L(R)}} + 0 \cdot W_{qp}^{\mathrm{LPT,R(L)}} + 1 \cdot W_{qp}^{\mathrm{CPS}} \right) P_p. \tag{3.3.11}$$

Here $W_{qp}^{\mathrm{LPT,L(R)}}$ and W_{qp}^{CPS} include the transition rates of all LPT and CPS processes creating electrons in the left (right) leads, respectively, and the summation goes over all possible initial and final states.

3.3.2 Interpretation of the results

Intuitively, one expects the CPS efficiency to be maximal when both QDs are close to their resonances[82]. This condition is satisfied in the vicinity of the degeneracy line of the $|FS, 1, GS, 0, FS\rangle$ and $|FS, 0, GS, 1, FS\rangle$ sectors in the phase diagram, i.e. at $-1 < \varepsilon_{\mathrm{L}}/U_{\mathrm{LR}} = \varepsilon_{\mathrm{R}}/U_{\mathrm{LR}} < 0$ on-site energy settings (brown line connecting the triple points in Fig. 3.3.3**a**). Therefore we studied the CPS efficiency $s = 2\Delta I/(I_{\mathrm{L}} + I_{\mathrm{R}})$ as a function of the inter-dot Coulomb repulsion at different locations in the charge stability map assigned by the markers in Fig. 3.3.3**a**, which are plotted in Fig. 3.3.3**b**. We remind that ΔI is the current contribution of CPS in any of the leads as in Eq. 2.2.26. For simplicity, the charging energies were chosen as $U_{\mathrm{L}} = U_{\mathrm{R}} = U = 1\,\mathrm{meV}$ and $\Delta = 0.2\,\mathrm{meV}$ has been used.

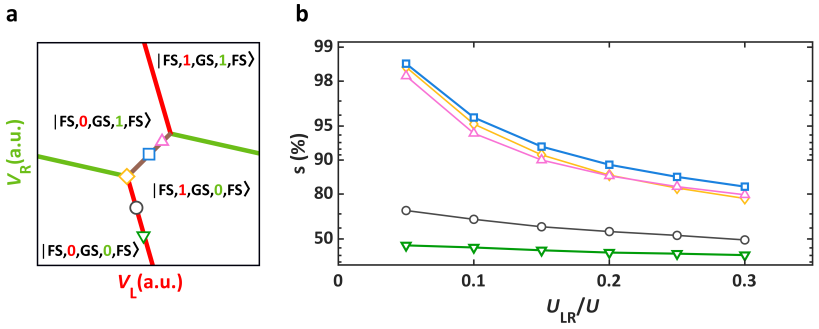

Figure 3.3.3: **Simulated CPS efficiencies.** **a** Sketched phase diagram of the honeycomb presenting the border of ground state occupations of both QDs simultaneously. By crossing the red (green) line, the electron number is changed on the left (right) QD. **b** U_{LR}/U dependence of s calculated in different points of the stability diagram, indicated by markers in panel **a**. While a decreasing tendency of the CPS contribution to the total current can be observed throughout the phase diagram, the efficiency is maximal in the middle of the $|FS, 1, GS, 0, FS\rangle$ and $|FS, 0, GS, 1, FS\rangle$ degeneracy line.

As visible in Fig. 3.3.3**b**, s is significantly higher along the degeneracy line of the $|FS,1,GS,0,FS\rangle$ and $|FS,0,GS,1,FS\rangle$ sectors (pink triangle, blue square, yellow diamond) than anywhere else in the stability diagram (agreeing with Eq. 2.2.26), and maximal at $\varepsilon_{\mathrm{L}}/U_{\mathrm{LR}} = \varepsilon_{\mathrm{R}}/U_{\mathrm{LR}} = -0.5$ ($\varepsilon_{\mathrm{L(R)}} \sim -V_{\mathrm{L(R)}}$), i.e. in the middle of the degeneracy line (blue square). This result is consistent with our experimental data where the non-local peaks were positioned to the center of the crossing resonance lines. By moving towards either of the triple points (pink triangle at $\varepsilon_{\mathrm{L}}/U_{\mathrm{LR}} = \varepsilon_{\mathrm{R}}/U_{\mathrm{LR}} = -0.8$), s decreases slightly. This small effect originates from the fact that any of the CPS cycles that involve both the $|FS,0,GS,0,FS\rangle$ and the $|FS,1,GS,1,FS\rangle$ configurations as intermediate states (see the CPS process step (1) and (3) depicted in Fig. 3.3.2 scenario **I.**) are penalized by $\sim U_{\mathrm{LR}}$. Obviously, by increasing U_{LR} the triple points separate further, hence suppressing s. We note that the calculations were performed at fixed $\varepsilon_{\mathrm{L(R)}}/U_{\mathrm{LR}}$ ratios compensating the change of the length of the brown degeneracy line in Fig. 3.3.3**a**. Once one of the QDs is detuned from the resonance (at the gray circle and the green triangle with fixed $\varepsilon_{\mathrm{L(R)}}$), s drops significantly in accordance with the expectations as LPT starts to dominate the transport. Altogether, $U_{\mathrm{LR}} \approx \Delta < 0.2\,\mathrm{meV}$ relevant for our experimental values, the reduction of s does not exceed 10% compared to the non-interacting case. We note that similar results can be obtained at other on-site energy settings (e.g. in the vicinity of the $|FS,1,GS,1,FS\rangle, |FS,2,GS,1,FS\rangle, |FS,1,GS,2,FS\rangle$ and $|FS,2,GS,1,FS\rangle, |FS,1,GS,2,FS\rangle, |FS,2,GS,2,FS\rangle$ triple points) due to the symmetry of the stability diagram.

As a simple analysis, one can derive the maximal efficiency attainable in single-nanowire-based CPS by assuming the typical values of $\delta r \approx 300\,\mathrm{nm}$ (see Fig. 3.1.1**a**) and $U_{\mathrm{LR}} = 0$ (**A**), and compare it to the calculation performed $U_{\mathrm{LR}} = 0.15\,\mathrm{meV}$ by assuming $\delta r = 30\,\mathrm{nm}$, reasonable for our setup (**B**, see Fig. 3.1.1**a**). According to Eq. 3.1.1, in the former case, $s^{\mathrm{A}}_{\mathrm{max}} \approx 82\%$, while in the latter one $s^{\mathrm{B}}_{\mathrm{max}} \approx 89\%$ in principle. By using these values, the geometry exhibiting a minimal δr, yet a finite U_{LR} turns out to be beneficial regarding the CPS efficiency. Naively one can argue it as $U_{\mathrm{LR}} \propto 1/\delta r$ while s decays exponentially in δr as outlined in Eq. 3.1.1. This consideration with the relatively high CPS efficiency reported here despite the parasitic inter-dot Coulomb repulsion confirms the merits of parallel InAs nanowires in future SC-semiconductor hybrids.

3.4 Conclusions

In summary, we have demonstrated significant CPS signals realized in parallel InAs nanowires connected by an epitaxial Al shell. The behavior of the coupled parallel SC-QD-N junctions was analyzed by spectroscopic measurements in both the superconducting and normal states. Owing to the geometrical properties, strong capacitive interaction was found between the QDs whose effect on the CPS was thoroughly studied. Due to the high-quality interface between the SC and semiconductor and the controlled QD formation, s_{max} = 29-36% CPS efficiency was achieved larger than previously reported in parallel-wire-based experiments, which lacked these features[97]. Our theoretical model also proved that, regarding s_{max}, the small spatial separation of the QDs outgrows the drawbacks of the inter-dot Coulomb repulsion, which causes $\sim 10\,\%$ relative reduction in s. The strong CAR makes the double-wire system with an epitaxial shell a promising platform to develop quantum circuits designed to realize Majorana bound states[172] or such exotic states as parafermions[152].

Chapter 4

Andreev molecule

Based on BCS mean-field theory[69], the superconducting vacuum only allows the addition of individual electrons with energy above the superconducting gap, however, it serves as a free source and of Cooper pairs. The interplay between a QD and the BCS vacuum was studied intensively as we reviewed before, contributing to the formation of YSR states or ABSs[99,102–106,111,112,114,115,119–121]. Two of such sub-gap states formed in the spatially separated QDs could be hybridized by the common SC lead, which we call an Andreev molecule[191]. While in a conventional molecular state, like the H_2, electrons tunnel through the vacuum (see Fig. 4.0.1**a** top), in an Andreev molecule the coupling mechanism is either the CAR or the EC via a SC (Fig. 4.0.1**a** bottom left and right panel, respectively). A CPS favors weak SC-QD couplings as we saw in the previous Chapter, nevertheless, an Andreev molecule requires the opposite limit. Several theoretical works investigated how two bound states localized on separated QDs effectively couple via the SC[48,57,123,170,171,191–196], i.e. as a minimal Kitaev chain[172]. Hybridization of YSR states was studied recently in scanning tunneling microscopy measurements placing different dimers on a SC surface[197–201]. Moreover, ABSs were also investigated in a SC coupled to QDs in series[202]. However, none of them has realized the strong hybridization of the artificial atoms needed for the realization of the Andreev molecular state, the elementary building block of the Kitaev chain from Fig. 2.4.2**c**[172].

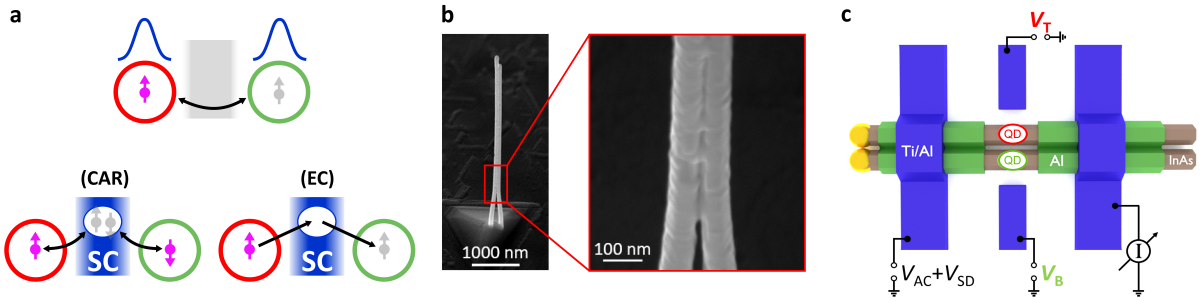

Figure 4.0.1: **Idea of the Andreev molecule.** **a** General concept of a molecular state formed by tunneling via a barrier between two atomic sites (top). In our case, the interaction between the QDs is mediated by CAR (bottom left) or EC (bottom right) via a SC. **b** High-resolution SEM of the as-grown parallel wires. The epitaxial Al connects the two InAs nanowires. **c** Schematic illustration of the device. The QDs are tuned by the two side gates with gate voltages V_T and V_B, while the differential conductance $G = I_{AC}/V_{AC}$ is measured in two-terminal measurements via superconducting contacts.

In this Chapter, we report the signature of an Andreev molecule in parallel InAs nanowires. In favor of the maximal proximity, we construct our minimal Kitaev block in nanowires covered with full-shell Al as shown in Fig. 4.0.1**b**. We explore the Andreev molecule excitation

spectrum[191] as a function of the QD level positions, for the first time in the literature, in the arrangement introduced in Fig. 4.0.1**c**. Since the measurements are rather complex, we build up the presented work deductively. We discuss the case of uncoupled YSR states and then compare it to the strongly interacting system involving the hybridization via SC and the Coulomb repulsion, both experimentally and theoretically[1]. The results of this Chapter is an extended version of Ref. 180.

4.1 Device outline

The details of the specific system studied here (Fig. 4.0.1**c**) are illustrated in Fig. 4.1.1. A parallel double QD was formed in a pair of InAs nanowires merged by epitaxial full-shell Al (briefly introduced in Section 2.5)[203]. The Al was removed on a $\sim$ 250 nm long segment in the middle of both nanowires by wet chemical etching, which was the most critical step of the fabrication process. In general, the shorter junctions are desired to obtain strong proximity, small QDs, and to avoid any serial resistive elements. Nevertheless, the reliability of the etching drops significantly if the window where the etchant can access to the Al is too narrow. As a compromission, the Al was etched in a nominally 150 nm wide rectangular shape providing a final width of 250 nm as a result of the underetching (for details see Appendix A.3). Two common superconducting (Ti/Al) electrodes were attached to epitaxial Al on the nanowires forming parallel SC-QD-SC junctions in the two wires, while 1-1 side gate electrodes were defined in the same EBL step. $\sim$ 10 chips with 5-6 devices on each were fabricated and 2 of them were studied in details which we present below.

The samples were cooled down to a base temperature of 40 mK inside a dilution refrigerator where electronic transport measurements were accomplished. In two-terminal sub-gap spectroscopy, the differential conductance $G = dI/dV_{\mathrm{AC}}$ was measured with the tuning of the QDs by individual plunger gates, as depicted in Figs. 4.0.1**c** and 4.1.1 (V_{T} corresponds to the top, V_{B} to the bottom gate voltage). The source terminal biased with V_{SD} was found to be coupled strongly to the QDs, whereas the other one worked as a superconducting tunnel probe leading to a parallel SC-QD-I-SC junction, where I stands for insulator. With this technique we recorded the single-electron excitation spectrum of the two QDs simultaneously as illustrated in Figs. 4.1.1**b** and **d**.

We present the behavior of two different devices. One of them (device A) did not show strong coupling between nanowires, and thus, serves as a reference junction, which is depicted in Figs. 4.1.1**a-b**. Careful SEM analysis revealed that the wires had separated and become disconnected, thus they were only linked by the Ti/Al contacts (blue) established at a distance of $\sim$ 400 nm far from the QDs. In this device we expect to see the physics of two, isolated YSR states lacking the SC-induced hybridization[82,204]. In the other sample (device B) shown in Figs. 4.1.1**c-d**, the Al shell remained intact, and the hybridization of YSR states was exhibited.

In the following, we review the spectrum of the parallel double QD structure in three steps: i) two independent, uncoupled YSR states, ii) adding inter-dot Coulomb repulsion, and iii) including the superconducting coupling while we discuss the measurements of both devices A and B. We label the QDs and their features as top (T) and bottom (B) ones, marked with red and green as in Fig. 4.1.1, respectively, supposing only a single YSR state residing in each QD ($\mathrm{YSR_T}$ and $\mathrm{YSR_B}$).

[1]The sample fabrication, the measurements, and the data analysis were performed by Olivér Kürtössy. The theoretical model was developed by Dr. Zoltál Scherübl. The project was guided by Dr. Péter Makk and Dr. Szabolcs Csonka.

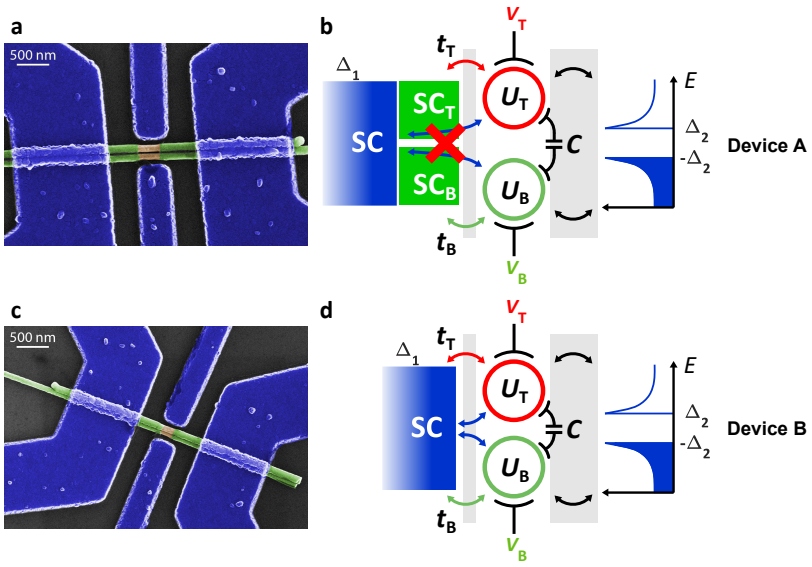

Figure 4.1.1: **Device outline.** **a** False-color SEM and **b** schematic illustration of device A. The epitaxial Al shell (green) is etched in the middle where the QDs are formed in the two InAs wires (brown). Only the ex-situ evaporated Al contacts (blue) connected the nanowires. **c-d** Similar to **a-b**, but illustrating device B. Here the epitaxial Al also couples the separate wires.

4.2 Uncoupled Yu-Shiba-Rusinov states

The parallel YSR states in uncoupled wires are discussed in Fig. 4.2.1 (top row: expectations, bottom row: measurements). Panel **a** illustrates the zero-bias conductance of the two wires as a function of the two plunger gate voltages in the normal state. Here the inter-dot capacitance is negligible, however, there is a finite cross capacitance between the top (bottom) plunger gate and the bottom (top) QD, resulting in the tilted lines in the phase diagram[65]. Panels **b** and **c** illustrate the finite-bias spectrum along the pink and blue dashed line in panel **a** parallel to the top QD resonances as a function of V_B. Asymmetric coupling of the wires, $t_T > t_B$ and different superconducting gaps of Δ_1 and Δ_2 for the strongly coupled electrode and the SC probe are considered, respectively, to reproduce the experimentally observed features. The spectroscopy yields the sum of an "eye-shaped" excitation (green) typical for YSR systems (see the simulated curve form Subsection 2.2.5 Fig. 2.2.5**e**) and an excitation line at constant energy (red). The green YSR patterns belong to the bottom QD (YSR_B), while the red ones can be identified as YSR_T since the on-site energy of the top QD is kept constant due to the parallel slicing in both panels. The excitations do not touch at zero V_{SD} but stay always at finite energy originating from the SC tunnel probe, which introduces a $\pm\Delta_2$ gap in the excitation spectrum. These minima correspond to the ground state transitions of the QD addressed also in the figure. Depending on the position of the slice, the energy of the constant line can vary between Δ_2 and $\Delta_1 + \Delta_2$. Obviously, the YSR_T excitation can occupy the lowest energy Δ_2 when the corresponding (top) QD is close to resonance (panel **c**, the blue line in panel **a**), while moving deeper in the blockade brings its energy towards the gap edge $\Delta_1 + \Delta_2$ regardless of the parity of the ground state. The movement of the signal while approaching a resonance is indicated with red arrows in panel **c**. For clarity, inset **I.** in panel **a** depicts YSR_T as the function of its own plunger gate (V_T), in which the markers assign the actual excitation energies considered in panels **b** and **c**.

The measurements of device A follow well our basic predictions outlined above. The stability map in the normal state, which was recorded by applying a 250 mT out-of-plane magnetic field, is shown in Fig. 4.2.1**d**. Two different bias cuts parallel to the top QD resonance in panels **e** and **f** reveal the movement of YSR_T (red arrow) while the development of YSR_B remains intact.

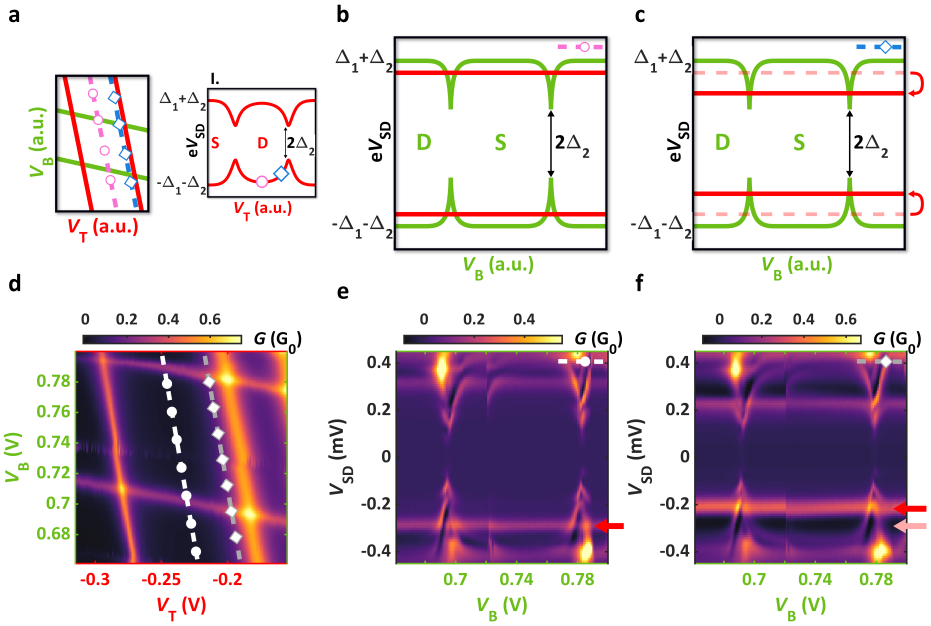

Figure 4.2.1: **Uncoupled parallel YSR spectra along V_B (device A).** **a** Schematic illustration about the stability map of parallel QDs with joint electrodes. Resonances of the top and bottom QDs are depicted in red and green, respectively. The lever arms refer to a finite cross capacitance of each gate to the opposite QDs. Inset **I.** depicts the YSR spectrum residing in the top QD ("S" and "D" refer to singlet and doublet ground states, respectively). Δ_1 and Δ_2 are the superconducting gaps of the strongly coupled electrode and the SC probe. The pink circle and the blue diamond indicate the energy of YSR_T along the cuts taken in the stability map. **b** Expected excitation spectrum of YSR states along the pink line shown in panel **a**. Whereas YSR_B (green) evolves along the cut since it is sensitive to its gate (V_B), the YSR_T state (red) stays on constant energy as the slice is parallel to the red resonances. **c** Bound state spectrum along the blue line in panel **a**. The excitation of the YSR_T state moved to lower energy compared to the one in panel **b** (the original energy is depicted with pink dashed lines) as the charge degeneracy of the top QD was approached (see the blue diamond in inset **I.** of panel **a**). **d** Measured conductance as a function of gate voltages for device A in the normal state. **e** Finite-bias spectroscopy measurement along the white dashed line depicted in panel **d** (superconducting state). Panel **b** illustrates well the experimental findings. The red arrows mark the excitations of YSR_T. **f** Finite-bias spectroscopy measurement along the gray dashed line with a diamond in panel **d**, closer to the resonance of the top QD matching to panel **c**. The pink arrow indicates the position of the YSR_T signals in panel **e**.

The latter one is identified as the dispersive line in the spectra which is crossed by the constant energy lines of YSR_T. The spectrum of panel **e** is measured along the white dashed line in panel **d** where the top QD is deep in the blockade, therefore YSR_T lies at high energy energy. In panel **f**, its original position (pink arrow) is pushed to lower energy since the spectrum is captured closer to the charge degenracy of the QD (gray dashed line from panel **d**). By a careful inspection of the data, one can identify an additional excitation line at higher energy, which can be attributed to another orbital of the bottom QD or to a higher-lying transition.

Now let us explore the spectra along the other gate direction, V_T, where a similar, but a more complicated behavior of the bound states was observed. The data are shown in Fig. 4.2.2 where the movements of multiple YSR_B states are trackable. Similarly to Fig. 4.2.1, panel **a** illustrates the conductance as a function of the top and bottom plunger gate voltages in the normal state. Here the spectra are examined parallel to the bottom QD resonances, therefore bias slices along the pink and blue cuts are taken. In panels **b** and **c**, the spectra along line cuts are presented off and close to resonance, respectively, with the "eye-shaped" YSR_T (red, similar to Fig. 2.2.5**e**) and the movement of YSR_B (green) depicted. We emphasize that YSR_B is less strongly coupled, thus its excitation energy is expected to be at $\Delta_1 + \Delta_2$ except in the close vicinity of the resonances where it drops continuously to Δ_2. The weak coupling also implies

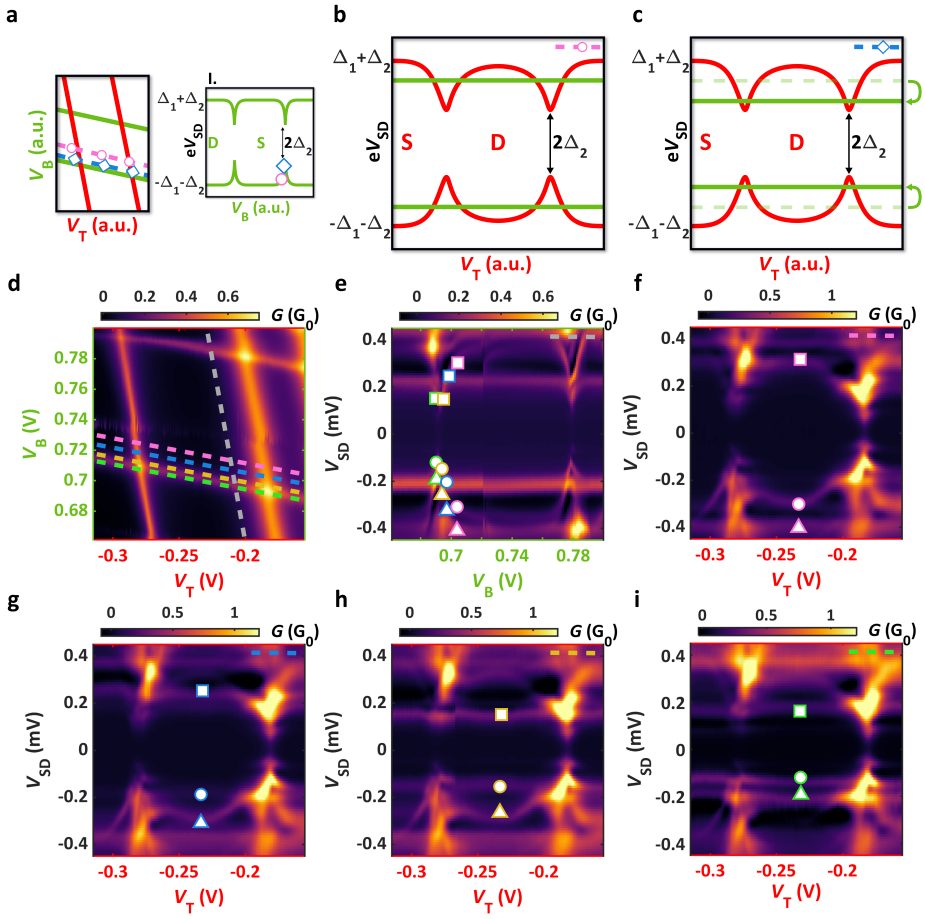

Figure 4.2.2: **Uncoupled parallel YSR spectra along V_T (device A). a** Sketch of the gate stability map as a function of V_T and V_B. The pink and blue lines indicate the line cuts along the spectra were studied. YSR_B spectrum with the markers upon is shown in inset **I.** to identify the corresponding energies along the cuts. **b** Predicted excitation spectrum along the pink line in panel **a**. YSR_T (red) is tuned by its own plunger gate and develops accordingly, while YSR_B (green) is kept on constant energy. **c** Similar spectrum as in panel **b**, but taken along the blue line, closer to the bottom QD resonance. The reduction of YSR_B excitation energy is expected (see green arrows) compared to the one in panel **b**. **d** Measured conductance as a function of the plunger gate voltages (same map as in Fig. 4.2.1**d**). **e** Measured excitation spectrum of the YSR_B states. The squares and circles indicate the dominant YSR_B, while the triangles indicate a more weakly coupled one. **f-i** Spectra along the lines shown in panel **d**. By moving closer to the bottom QD resonances, both YSR_B state energies are lowered providing double lines together with the unaffected YSR_T state. The low visibility of YSR_B comes from their low conductance compared to the "eye-shaped" YSR_T.

the small conductance and the reduced visibility of YSR_B in the measurements compared to the much stronger features of YSR_T, which makes the tracking of its movements rather difficult. Moreover, in the experiments, besides the dominant YSR_B highlighted by the square and circle symbols in panel **e**, the line of an additional YSR excitation can be observed. This state perhaps originates from another orbital of the bottom QD due to the finite level spacing and is marked by triangles in panel **e**. Nevertheless, the movements of both YSR_B states, which can be followed in panels **f-i**, are consistent with the green curves in panels **b** and **c**. The normal state gate stability map with dashed lines indicating where the spectra were taken is shown in panel **d**. When the line cuts are taken relatively far from the bottom QD resonance (panels **f-g**), the weakly coupled YSR_B marked with the triangles is barely visible and in energy is close to the gap edge. By approaching the resonances (panels **h-i**), both YSR_B excitations are lowered resulting in doubled constant energy lines crossing the "eye-shaped" YSR_T, whose conductance is sufficiently higher.

All the individual symbols in panel **e** indicating the development of the YSR_B states can be assigned to their pairs in panels **f-i** consistently describing the movements. Based on the two dominant lever arms in the stability sweep and the fact that different YSR states were captured by tuning either V_T or V_B confirmed the model of having YSR states in both QDs.

We note that the Kondo effect[105,205,206] was suppressed in most of the gate settings in both device A and B since the Kondo temperature did not exceed the superconducting gap ($k_B T_K < \Delta_1$). As the QDs enter a more open regime, Kondo correlations appear to compete with the superconductivity, which reduces the visibility of the outlined YSR behaviors.

4.3 Inter-dot Coulomb repulsion

The question arises of how the spectrum is modified compared to the uncoupled case if there is significant inter-dot capacitance. The normal state stability map turns into the honeycomb pattern (see Fig. 4.3.1**a**) well known for double QDs[65] as we discussed in Subsection 2.1.4. Hence, slicing parallel to any resonances along a straight line in the gate map gives no longer a constant-energy YSR state, but a charge state-dependent one. For example, along the pink dashed line, the top YSR state develops according to the symbols in inset **I.**, where YSR_T is depicted as a function of its own plunger gate, V_T. For small V_B values, the line cut is off-resonance and YSR_T is in the doublet ground state (diamond symbol). By increasing V_B the bottom QD is brought to resonance which leads to an effective gating of the top QD. This shifts the top QD closer to its resonance and lowers the energy of YSR_T (circle symbol). Going through another resonance of the bottom QD (by further increasing V_B) displaces the top QD resonance again and its YSR state ends up in the singlet ground state (square symbol). These jumps of the signal at the charge degeneracy points, where the on-site energy of the QD changes abruptly, imply "step-like" excitations in total (see the red lines in panel **d**). Analogously, a similar spectrum (shown in panel **h**) is obtained along the blue line in panel **a** with the symbols in inset **II.**.

Whereas the uncoupled YSR states described well the behavior of device A, they clearly can not match the measurements on device B, shown in Figs. 4.3.1**g** and **k**. Therefore we now compare them to the simple case of having capacitive coupling between the two QDs and then to a fully interacting one, where EC and CAR are present between YSR_B and YSR_T. Fig. 4.3.1**c** shows the measured normal state map providing qualitatively the same honeycomb structure (illustrated with black dashed lines) as the one in panel **a**. Sub-gap spectroscopy was performed along the white and gray dashed lines. Similarly to device A, in the measurements of device B, the conductance of YSR_T (red) was found to be larger than YSR_B (green) fulfilling the assumption of $t_T > t_B$ already mentioned. In panel **g**, the spectrum is presented as a function of V_B exhibiting similarities to panel **d**. The YSR_B state is mostly bound to the gap edge and develops rapidly at the ground state transitions matching the green curve in panel **d**. The YSR_T state (marked by the pink symbols at negative bias) also provides "step-like" features resembling to the red curve in panel **d** as e.g. the vertical position of the pink circle change compared to pink diamond. Nonetheless, clear discrepancies emerge between the experiemnts and our expectation close to the charge degeneracy points ($V_B = 1.91\,V$ and $V_B = 2\,V$). As the YSR_B and YSR_T excitations approach each other, they anti-cross, and YSR_T bends towards zero energy (indicated by white arrows) suggesting the hybridization of the states, which is unexpected in a simple capacitive picture.

The discrepancy between the predicted sketch and the measured data is more obvious for cuts along the other gate direction as the comparison of panels **h** and **k** shows. Assuming only capacitive coupling between QDs (panel **h**), YSR_T is expected to take the red, "eye-shaped" curve as a function of V_T like in Fig. 2.2.5**e** from Subsection 2.2.5. Such excitation is measured when YSR_B is far off-resonance (see the white dashed line in panel **k** and Appendix A.2).

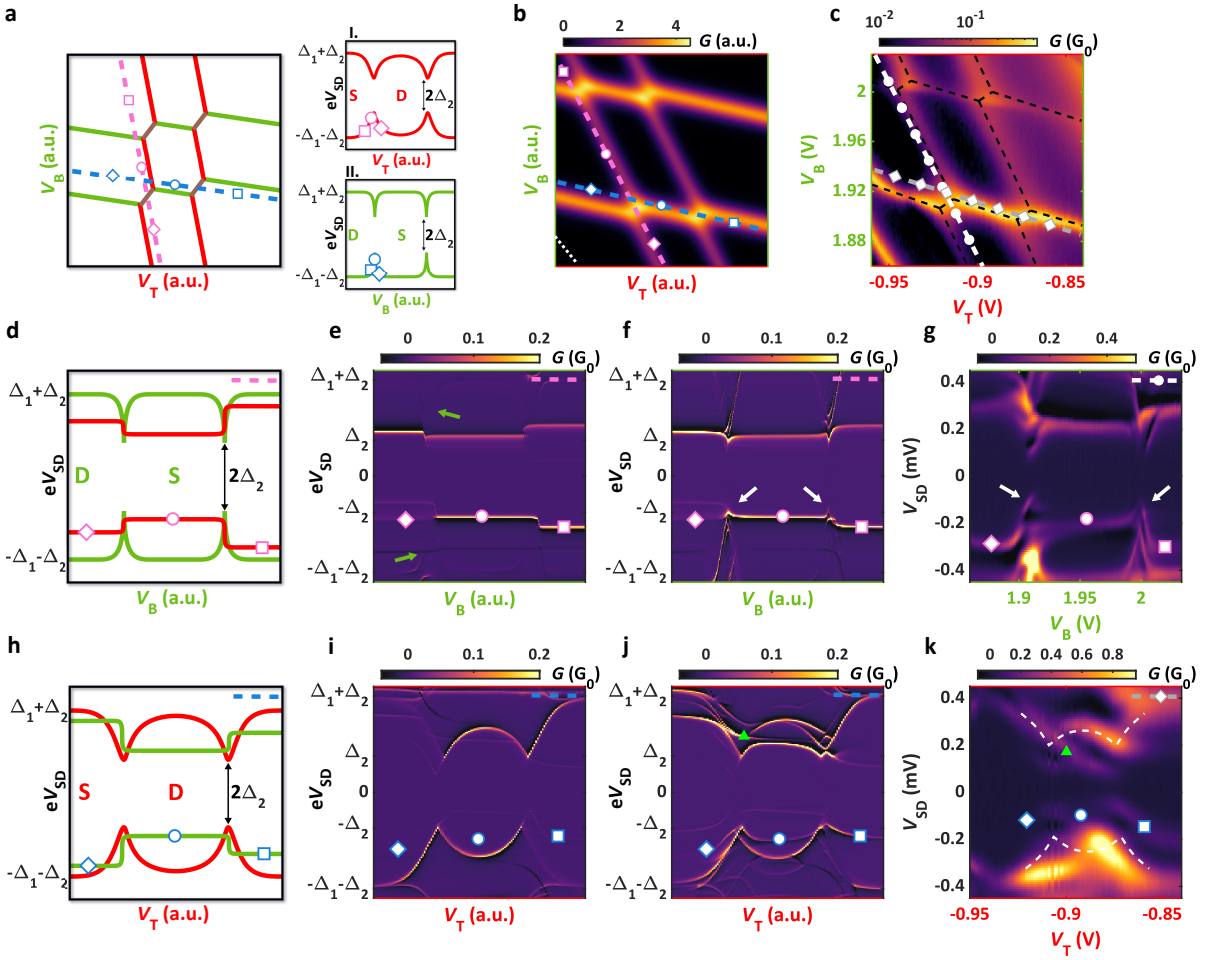

Figure 4.3.1: **Coupled YSR states (device B). a** Stability map of parallel QDs with strong inter-dot capacitance. Despite the pink and blue cuts being parallel to the resonances of the top and bottom QDs, respectively, the excitation energies of the neighboring YSR states shift while crossing the triple points. Markers in the insets indicate the corresponding YSR state energies along the cuts. **b** Simulated normal state stability map reproducing the experimental data and panel **a**. **c** Normal state conductance as a function of the plunger gates on device B. The black dashed line illustrates the honeycomb structure attributed to the parallel QD system. **d** Predicted spectrum along the pink line (tuning the bottom QD) from panel **a** by considering the Coulomb interaction. Steps in the energy of YSR_T are expected. **e-f** Numeric simulation of panel **d** with **e** only capacitive interaction and with **f** full hybridization via the SC along the pink lines of panel **b**. The superconductivity induces bendingss, anti-crossings, and conductance enhancement in YSR_B. **g** Bias spectroscopy measurement along the dashed line with circles depicted in panel **c**. Anti-crossings and bendings towards zero energy occur at the charge degeneracy points marked by the white arrows showing resemblance to panel **f**. **h** Similar spectrum to the one in panel **d**, but along the blue line in panel **a** resulting in the tuning of the top QD. **i-j** Similar simulation as panels **e-f**, but along the blue line in panel **b**. The enhanced YSR_B in panel **j** develops distinctly from the capacitive model in panel **i** and leads to distortions in YSR_T. The excitation lines are multiplied and not even symmetric in bias. **k** Measured spectrum along the other dashed line with diamonds from panel **c**. The white dashed line shows the "eye-shaped" YSR_B doublet when it is recorded off-resonance. Additional excitation lines, such as the one marked by the green triangle, also appear in accordance with panel **j**.

However, the spectrum captured close to the resonance of YSR_B (along the gray dashed line in panel **c**) strongly deviates from the expectation of simple capacitive coupling as the comparison of panels **k** and **h** demonstrates. The unusual evolution of the signals was quite robust along any cuts taken in the vicinity of the charge degeneracies.

4.4 Superconducting coupling

For the next step, we introduce two numerical models to describe the transport in the system using Eqs. 2.1.18, 2.2.35 and 2.2.36 as a starting point. In the first model, we only allow the capacitive interaction between the two QDs by assuming two separate SCs disconnected from each other (see Fig. 4.1.1**b**). In the second one, we consider a single SC connecting the QDs via CAR and EC (see Figs. 4.0.1**a** and 4.1.1**d**). Direct tunnel coupling between the QDs is forbidden in both cases (i.e. $t = 0$ from Eq. 2.1.18). The comparison of these two simulations and the measurements of device B allows us to address the peculiarities in the spectra and separate the impact of the capacitive interplay and superconducting hybridization (both CAR and EC) of the QDs. As shown below, the capacitively interacting model mimics the sketched spectrum in Figs. 4.3.1**d** and 4.3.1**h**, while our fully interacting two-QD simulation reproduces all the main features of the unique experimental spectra in Figs. 4.3.1**g** and 4.3.1**k**.

4.4.1 Modeling

In both theories, the QDs are modeled as capacitively interacting single sites (see Figs. 4.1.1**b** and 4.1.1**d**) coupled to the SC with tunnel amplitudes t_T and t_B. This restricts the electron number on the QDs between 0 and 2 like in the single impurity Andreson model of Eq. 2.1.6. The left SC(s) in Figs. 4.1.1**b** and 4.3.1**d** is handled in the ZBA[112,116–118] with energy gap Δ_1. The right superconducting probe with Δ_2 gap is treated perturbatively with Dynes-like DOS[207,208], effectively embodying a soft gap of Eq. 2.2.13. By allowing only a limited number of quasi-particles to be present in the system, the energy spectra and the eigenstates can be derived with exact diagonalization of the Fock-space Hamiltonians, similarly to Eq. 2.2.35. Transition rates between the states, involving the processes of adding and removing an electron to the Andreev molecule in the fully interacting case, are expressed by Fermi's golden rule[94]. The transport (net current) is obtained by solving the classical master equation in the stationary limit, which governs the time evolution of the QD occupations.

Let us now discuss the fully-interacting QD model in detail, and then return to the only capacitively coupled case. The total Hamiltonian of the system is

$$H = H_\mathrm{DQD} + H_\mathrm{SC1} + H_\mathrm{SC2} + H_\mathrm{T1} + H_\mathrm{T2}, \tag{4.4.1}$$

The first term constructs the double QD

$$H_\mathrm{DQD} = \sum_{\alpha=\mathrm{T,B}} \left(\varepsilon_\alpha n_\alpha + U_\alpha n_{\alpha\uparrow} n_{\alpha\downarrow} \right) + C n_\mathrm{T} n_\mathrm{B}, \tag{4.4.2}$$

where $n_{\alpha\sigma} = d^\dagger_{\alpha\sigma} d_{\alpha\sigma}$ is the electron number operator with spin σ in QD_α. $d^{(\dagger)}_{\alpha\sigma}$ is the annihilation (creation) operator of electrons with spin σ in QD_α and $\alpha = \mathrm{T,B}$ denotes the top and bottom QDs. The parameters, ε_α and U_α are the level position and the charging energy of QD_α, respectively, and C is the inter-dot Coulomb repulsion.

As the strongly coupled SC (SC1) is described on the level of the ZBA, the $\mathrm{QD_T}$–SC1–$\mathrm{QD_B}$ subsystem Hamiltonian can be diagonalized exactly to obtain the energy spectrum of the Andreev molecule. The ZBA SC Hamiltonian is

$$H_\mathrm{SC1} = \Delta_1 \left(c^\dagger_{\mathrm{SC1}\uparrow} c^\dagger_{\mathrm{SC1}\downarrow} + c_{\mathrm{SC1}\downarrow} c_{\mathrm{SC1}\uparrow} \right), \tag{4.4.3}$$

where $c^{(\dagger)}_{\mathrm{SC1}\sigma}$ is the annihilation (creation) operator of an electron with spin σ in the SC and Δ_1 is the superconducting gap. This Hamiltonian can be diagonalized by a Bogoliubov-transformation,

$c_{\mathrm{SC1}\sigma} = \frac{1}{\sqrt{2}}\left(\gamma_\sigma - \sigma\gamma_{\bar{\sigma}}^\dagger\right)$ which we introduced in Eq. 2.2.37, obtaining

$$H_{\mathrm{SC1}} = \Delta_1 \sum_\sigma \gamma_\sigma^\dagger \gamma_\sigma. \tag{4.4.4}$$

The tunnel coupling between SC1 and the QDs is written as

$$H_{\mathrm{T1}} = \sum_{\alpha=\mathrm{T,B}} t_\alpha \sum_\sigma \left(d_{\alpha\sigma}^\dagger c_{\mathrm{SC1}\sigma} + c_{\mathrm{SC1}\sigma}^\dagger d_{\alpha\sigma}\right), \tag{4.4.5}$$

where t_α is the tunneling amplitude. Applying the Bogoliubov transformation for this Hamiltonian leads to

$$H_{\mathrm{T1}} = \frac{1}{\sqrt{2}} \sum_{\alpha\sigma} t_\alpha \left(d_{\alpha\sigma}^\dagger \left(\gamma_\sigma - \sigma\gamma_{\bar{\sigma}}^\dagger\right) + \left(\gamma_\sigma^\dagger - \sigma\gamma_{\bar{\sigma}}\right) d_{\alpha\sigma}\right), \tag{4.4.6}$$

just like in Eq. 2.2.39. We emphasize that EC and CAR processes are hidden in this tunneling term.

$H_{\mathrm{DQD}} + H_{\mathrm{SC1}} + H_{\mathrm{T1}}$ is numerically diagonalized from which the spectrum and the wavefunction of the Andreev molecular state are extracted directly.

In Eq. 4.4.1 H_{SC2} and H_{T2} describes the second superconducting lead (SC2) and its weak tunnel coupling to the QDs, respectively. The SC2 is described by the BCS Hamiltonian,

$$H_{\mathrm{SC2}} = \sum_{\mathbf{k}\sigma} \varepsilon_{\mathrm{SC2}\mathbf{k}} c_{\mathrm{SC2}\mathbf{k}\sigma}^\dagger c_{\mathrm{SC2}\mathbf{k}\sigma} + \Delta_2 \sum_{\mathbf{k}} \left(c_{\mathrm{SC2}\mathbf{k}\uparrow}^\dagger c_{\mathrm{SC2}-\mathbf{k}\downarrow}^\dagger + c_{\mathrm{SC2}-\mathbf{k}\downarrow} c_{\mathrm{SC2}\mathbf{k}\uparrow}\right), \tag{4.4.7}$$

where $c_{\mathrm{SC2}\mathbf{k}\sigma}^{(\dagger)}$ is the annihilation (creation) operator for electrons with momentum $\mathbf{k}$ and spin σ in the SC2, $\varepsilon_{\mathrm{SC2}\mathbf{k}}$ is normal state dispersion and Δ_2 is the superconducting gap. We note that both Δ_1 and Δ_2 are assumed to be real, while the possible effects originating from the superconducting phase difference are neglected. The tunnel coupling Hamiltonian is

$$H_{\mathrm{T2}} = t_{\mathrm{SC2}} \sum_{\alpha\mathbf{k}\sigma} \left(d_{\alpha\sigma}^\dagger c_{\mathrm{SC2}\mathbf{k}\sigma} + c_{\mathrm{SC2}\mathbf{k}\sigma}^\dagger d_{\alpha\sigma}\right), \tag{4.4.8}$$

where t_{SC2} is tunneling amplitude, for simplicity, assumed to be the same for the two QDs.

The tunnel coupling to SC2 is treated perturbatively by using Fermi's golden rule[94], which induces transitions between eigenstates of the $\mathrm{QD_T}$–SC1–$\mathrm{QD_B}$ system. The time evolution of the occupation of the eigenstate $|\chi\rangle$, P_χ, is governed by a master equation together with the normalization condition $\sum_\chi P_\chi = 1$,

$$\frac{dP_\chi}{dt} = \sum_{\chi'\neq\chi} \left(W_{\chi\chi'} P_{\chi'} - W_{\chi'\chi} P_\chi\right). \tag{4.4.9}$$

Here $W_{\chi\chi'}$ is the total transition rate from $|\chi'\rangle$ state to $|\chi\rangle$. The rates are the sum of two processes, when an electron is added to the Andreev molecule and when one is removed, i.e. $W_{\chi\chi'} = W_{\chi'\chi}\left(d_{\alpha\sigma}^\dagger\right) + W_{\chi'\chi}\left(d_{\alpha\sigma}\right)$. These two contributions are expressed as

$$\begin{aligned} W_{\chi'\chi}\left(d_{\alpha\sigma}^\dagger\right) &= \pi t_{\mathrm{SC2}}^2 \left|\langle\chi'|\, d_{\alpha\sigma}^\dagger \,|\chi\rangle\right|^2 \rho_{\mathrm{SC}}\left(E_\chi - E_{\chi'} - \mu_{\mathrm{SC2}}\right) f\left(E_\chi - E_{\chi'} - \mu_{\mathrm{SC2}}\right) \\ W_{\chi'\chi}\left(d_{\alpha\sigma}\right) &= \pi t_{\mathrm{SC2}}^2 \left|\langle\chi'|\, d_{\alpha\sigma} \,|\chi\rangle\right|^2 \rho_{\mathrm{SC}}\left(E_\chi - E_{\chi'} + \mu_{\mathrm{SC2}}\right) \left(1 - f\left(E_\chi - E_{\chi'} - \mu_{\mathrm{SC2}}\right)\right), \end{aligned} \tag{4.4.10}$$

where $\rho_{\mathrm{SC}}(E) = \rho_0 \mathrm{Re}\left(\frac{E+i\gamma}{\sqrt{(E+i\gamma)^2-\Delta_2^2}}\right)$ is the Dynes-like DOS in SC2[207,208], with γ being the Dynes-parameter and ρ_0 is the normal state DOS, assumed to be constant, $f(E)$ is the Fermi function, E_χ denotes the energy of the $|\chi\rangle$ state and $\mu_{\mathrm{SC2}} = eV_{\mathrm{SD}}$ is the electrochemical potential difference of the two superconducting leads as a result of the applied bias voltage V_{SD}.

To derive the current flowing from SC1 to SC2, the master equation Eq. 4.4.9 is solved in the stationary limit, namely $dP_\chi/dt = 0$. The current is written as

$$I = \frac{e}{\hbar} \sum_{\alpha\chi\chi'\sigma} \left(W_{\chi'\chi}\left(d_{\alpha\sigma}\right) - W_{\chi'\chi}\left(d^\dagger_{\alpha\sigma}\right)\right) P_\chi. \tag{4.4.11}$$

The differential conductance is obtained as the derivative of the current, i.e. $G = e\frac{dI}{d\mu_{\mathrm{SC2}}}$.

For the case, when only capacitive coupling is assumed between the QDs, one has to exclude the SC-mediated tunneling processes that couple the states of the two QDs, i.e. EC and CAR. One can formally remove them by coupling the QDs to two separate SCs. This can be formulated in the following Hamiltonians:

$$H_{\mathrm{SC1}} = \Delta_1 \sum_{\alpha=\mathrm{T,B}} \left(c^\dagger_{\mathrm{SC1}\alpha\uparrow} c^\dagger_{\mathrm{SC1}\alpha\downarrow} + c_{\mathrm{SC1}\alpha\downarrow} c_{\mathrm{SC1}\alpha\uparrow}\right), \tag{4.4.12}$$

$$H_{\mathrm{T1}} = \sum_{\alpha=u,l} t_{\mathrm{SC1}\alpha} \sum_\sigma \left(d^\dagger_{\alpha\sigma} c_{SC1\alpha\sigma} + c^\dagger_{SC1\alpha\sigma} d_{\alpha\sigma}\right). \tag{4.4.13}$$

The difference compared to Eqs. 4.4.3 and 4.4.5 is that SC1 is split into two parts, which are only coupled to one of the QDs. This way the electron tunneling hybridizes the QD and SC states to local YSR states, but the further coupling of the YSR states into molecular states is prevented. The rest of the transport calculation is the same as above.

In both models, we have used charging energies $U_{\mathrm{T}} = 1.2\,\mathrm{meV}$ and $U_{\mathrm{B}} = 2.2\,\mathrm{meV}$, off-site repulsion energy $C = 0.1\,\mathrm{meV}$ (derived based on Fig. 2.1.4**d** and similarly to the CPS experiments from Chapter 3), and superconducting gaps of $\Delta_1 = 200\ \mu\mathrm{eV}$ and $\Delta_2 = 120\ \mu\mathrm{eV}$, which were directly extracted from the experimental data. Tunnel amplitudes were estimated as $t_{\mathrm{T}} = 0.15\,\mathrm{meV}$ and $t_{\mathrm{B}} = 0.05\,\mathrm{meV}$ based on the shape of the YSR states, thus the models have no fitting parameters.

4.4.2 Discussion

The simulated normal-state honeycomb diagram for both models is depicted in Fig. 4.3.1**b** matching qualitatively to the experiment in Fig. 4.3.1**c**. The spectra calculated along the pink line from panel **b** in the capacitively interacting QD model and in the fully interacting model are shown in Figs. 4.3.1**e** and 4.3.1**f**, while the ones along the blue line are in Figs. 4.3.1**i** and 4.3.1**j**, respectively. After a quick comparison of the sketched spectra (Figs. 4.3.1**d** and 4.3.1**h**) with Figs. 4.3.1**e** 4.3.1**i** one can see that the capacitive model qualitatively gives back the expected spectra (compared to Fig. 2.2.5**e**). We note that $\mathrm{YSR_B}$ is hardly visible in panel **e** (indicated by the green arrows) due to its weak coupling to the leads and its disjuncture from $\mathrm{YSR_T}$.

The results of the fully interacting model in panels **f** and **j** differ from the simple capacitive picture in many aspects and they suggest that the hybridization via the SC strongly restructures the spectra. Let us now carefully compare the measurements in panels **g** and **k** with the calculated fully-interacting spectra in panels **f** and **j**, and show that they qualitatively match well. (i) The anti-crossings and the bendings of $\mathrm{YSR_T}$ observed particularly in Fig. 4.3.1**g** are restored in the numerical results (see white arrows in Fig. 4.3.1**f**). As a result of using a superconducting

tunnel probe, negative differential conductance around the YSR signals also appears in both the experiments and the simulations.

In general, there are several characteristic features in Fig. 4.3.1**f**, which strongly deviate from the capacitive picture in panel **i**, nevertheless, they are qualitatively recovered in the interacting spectra in panel **j**, therefore we now focus on the comparison of panels **k** and **j**. First of all, (ii) the "eye-shaped" YSR_T resonance is completely distorted in the measurement as well as in the numerical data. Moreover, (iii) the expected horizontal YSR_B signal does not stay flat in the doublet region of YSR_T (indicated by the blue circle between $V_T = -0.92\,V$ and $V_T = -0.87\,V$), rather follows the curvature of YSR_T similarly in the simulation. Though well-pronounced anti-crossings are absent, (iv) extra dispersive lines (one example is marked by the green triangle) arise between the YSR_T and YSR_B signals, likewise in the interacting theoretical curves. These extra excitations are completely missing from the capacitive model. (v) It is also remarkable that the measured spectrum is asymmetric for the sign of the bias, which is also established in panel **j**. It is notable that (vi) the conductance of the YSR_B, whose coupling is three times weaker than YSR_T in the model, is greatly enhanced and reaches $\sim 80\,\%$ of the strongly coupled YSR_T near the charge degeneracy points, in agreement with the fully-interacting QD spectra and contrary to panel **e**. Besides the good agreement in the listed properties (i-vi), the theory of coupled YSR states does not match the measurements in a few aspects. On one hand, the discrepancies originate from the several simplifications the models take. The calculations neglect the presence of multiple QD orbitals and exclude the relaxation from excited states, hence allowing arbitrary high-energy virtual states, which are usually not visible in a bias spectroscopy measurement. On the other hand, further limitation comes from the broad linewidth of the measured YSR states smearing the neighboring excitation lines. Overall, despite the theory being simplified, many prominent features of the measured data were captured in the simulation qualitatively by assuming hybridization via the SC, which supports our interpretation of an observed Andreev molecule.

4.4.3 Additional data

To strengthen our arguments that the observed spectra in Fig. 4.3.1 originate from a global Andreev molecule and not local anomalies at a specific gate setting, here we provide additional spectra of the same gate region, but along different traces in the stability map. The data is shown in Fig. 4.4.1.

In panel **a**, the honeycomb structure as a function of the plunger gate voltages is sketched with the pink and blue lines parallel to the resonance lines but positioned differently than in Fig. 4.3.1**a**. Therefore the YSR states occupy different energies along these cuts again, which are demonstrated by the markers in inset **I.** and inset **II.**. Panel **b** consists of the measured gate stability map in the normal state in a larger window compared to the one Fig. 4.3.1. Panels **c** and **d** show large bias spectroscopy measurements accomplished in the normal state along the dotted lines in panel **b** exhibiting the Coulomb diamonds.

In panels **e** and **f** the expected and numerically simulated spectra of the capacitively interacting bound states along the pink cut from panel **a** are illustrated. As the distance between the trace and the top QD resonance increases with V_B (due to effective gating of the Coulomb interaction) in panel **a**, YSR_T jumps from $\sim \Delta_2$ to higher energies when the bottom QD resonances are crossed (see the pink circle and square). Nonetheless, the spectrum changes drastically if the superconducting coupling between the QDs is involved, similarly to Fig. 4.3.1 (see panel **g**). Anti-crossings between YSR_B and YSR_T are induced and thus, the latter bends to lower energy in the vicinity of the charge degeneracy points. The conductance of the weakly coupled YSR_B state (marked by the green arrows) is also enhanced in panel **g** compared to panel **f**. The corresponding experimental data (panel **h**) is in much better agreement with the spectrum de-

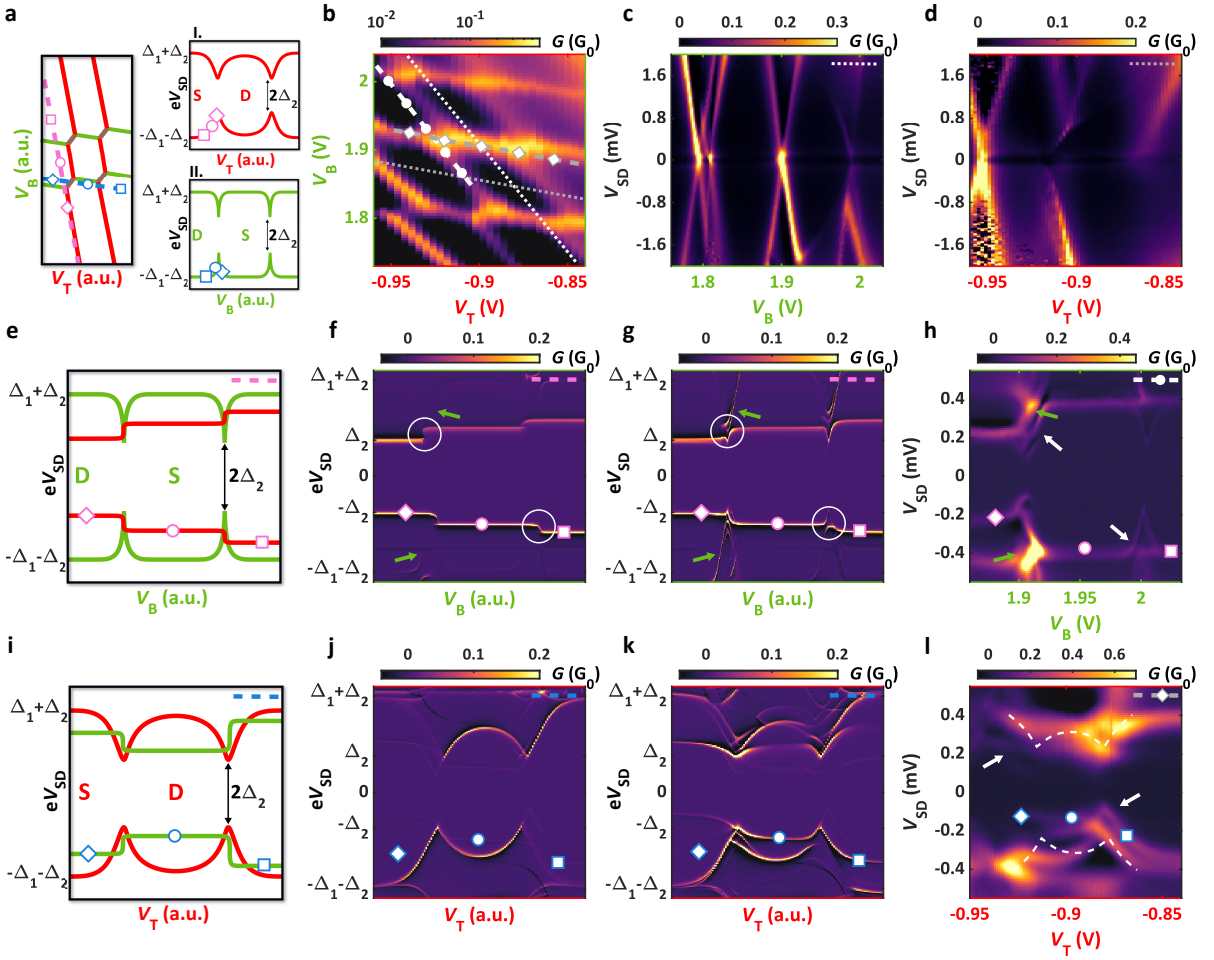

Figure 4.4.1: **Additional data for the interacting YSR states (device B). a** Sketch of the gate stability map as a function of V_{T} and V_{B} in the presence of strong Coulomb interaction. Similarly to Fig. 4.3.1**a**, the pink and blue lines indicate the line cuts along the spectra that were studied. Markers in the inset spectra guide identifying the bound state energies again. **b** Measured gate stability map in the normal state in a larger window compared to the one in Fig. 4.3.1. **c-d** Large-bias spectroscopy of the QDs in the normal states along the dotted lines in panel **b**. **e-f** Predicted and simulated spectra along the pink line in panel **a** without and **g** with superconducting coupling introduced in the model. The superconducting coupling induces anti-crossings (white circles) and conductance enhancement (green arrows) as seen in the data of Fig. 4.3.1. **h** Corresponding spectrum captured along the white dashed line in panel **b**. The highlighted anti-crossings (white arrows) and conductance enhancements (green arrows) are recovered in panel **g**, in the simulation of the fully interacting model. **i-k** Similar to panels **e-g**, but along the blue cut in panel **a**. Completely different development of the $\mathrm{YSR_B}$ signal is expected as the superconducting hybridization is turned on from the purely capacitively interacting case (panel **j**). **l** Finite-bias spectroscopy along the gray dashed line in panel **b**. The white dashed line shows the undisturbed $\mathrm{YSR_T}$ doublet measured far from the bottom QD resonances. All the key features, including the asymmetry in bias, doubling of the excitation lines, and their dispersive evolution are in good agreement with the theory in panel **k**.

rived from the fully interacting model. (i) Besides the anti-crossings being dominant (indicated by the white arrows), (ii) the conductance is greatly enhanced at $V_{\mathrm{B}} = 1.91\,\mathrm{V}$ predicted by the numerical simulation in panel **g**.

The hybridization is even more manifest in the slice parallel to the bottom QD resonances. Panel **i** in Fig. 4.4.1 illustrates the naive expectation of the capacitively interacting spectra along the blue cut in panel **a**. The numerical simulation in panel **j** qualitatively agrees with the sketch, nevertheless, we note that the shifts in the $\mathrm{YSR_B}$ excitation energies at the ground state

transitions are smooth and continuous, and not abrupt. This phenomenon can be attributed to the number of electrons not being quantized in the singlet state since the ground state is the superposition of empty and doubly occupied states in a standard YSR or Andreev picture. Panels **k** and **l** show the simulation of the fully interacting model and the relevant bias spectroscopy measurement along the gray dashed line in panel **b**, respectively. In resemblance to the data shown in Fig. 4.3.1, (iii) bias asymmetry, (iv) distortions, and (v) the doubling of the excitation lines with their dispersive evolution (see white arrows in panel **k**) are observed matching the theory well in panel **j**.

4.4.4 Detailed spectrum

To get a deeper insight into the structure of an Andreev molecular spectrum, here we give a short analysis to identify most of the excitation lines in the simulation of the hybridized YSR states shown in Fig. 4.3.1**j**. For simplicity, in the slice taken along Fig. 4.4.2**a**, we only focus on the positive bias features which are highlighted in Fig. 4.4.2**b**.

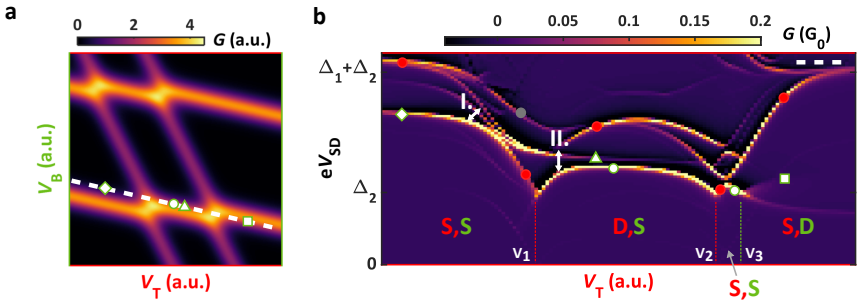

Figure 4.4.2: **Deatiled spectrum of the fully-interacting model.** **a** Stability map of Fig. 4.3.1**b** and **b** the zoomed positive-bias excitation spectrum of Fig. 4.3.1**j**. The red and green markers indicate the single-electron excitations of $\mathrm{YSR_T}$ and $\mathrm{YSR_B}$. They hybridize via EC and CAR at the white arrows I. and II., respectively. Triplet-singlet splitting of $\mathrm{YSR_B}$ is also visible at $V_1 < V_\mathrm{T} < V_2$ (see the green triangle and circle).

The dominant ground state settings of the top and bottom QDs in the Shiba picture are assigned by the red and green S/D letters, respectively. The red circles mark the signal originating from $\mathrm{YSR_T}$, while the green symbols are attributed to $\mathrm{YSR_B}$. At small V_T values, both QDs are in the singlet ground states with a $|0,0\rangle$ kind of configuration, where the two numbers give the electron occupiation of the two QDs as $|m,n\rangle = |m\rangle_\mathrm{T} \otimes |n\rangle_\mathrm{B}$. The bottom YSR state excitation resides at relatively high energy marked by the green diamond, in accordance with panel **a**. At $V_\mathrm{T} = V_1$ and V_2 gate voltage values, $\mathrm{YSR_T}$ reaches the minimum energy, which is given by Δ_2 due to the SC probe. Below $V_\mathrm{T} < V_1$, the excitation lines of $\mathrm{YSR_T}$ and $\mathrm{YSR_B}$, corresponding to the $|1,0\rangle$ and $|0,1\rangle$ states approach each other and they bend as highlighted by the white arrow (I.). This level repulsion (regarding of the inclusion of the $|1,0\rangle$ and $|0,1\rangle$ sectors) is induced by the EC between the QDs. For $V_1 < V_\mathrm{T} < V_2$ the ground state of the top QD becomes a doublet, while the bottom one remains singlet with a $|1,0\rangle$-like character. In this region, the single "eye-shaped" curve typical for a YSR doublet (see Fig. 2.2.5**e**) is discontinuous and distorted (red circle) when the $\mathrm{YSR_B}$ gets close to it. This level repulsion is particularly strong in the vicinity of the white arrow (II.) slightly above V_1. Since the single-electron excitation lines with the red and green circles belong to the $|0,0\rangle$ (or $|2,0\rangle$ as V_T is increased towards V_2) and $|1,1\rangle$ singlet states, respectively, they hybridize via CAR. Besides the two dominant curves, an additional line is also observable indicated by the green triangle, which is the triplet of the $|1,1\rangle$ configuration not affected by the CAR. This feature was also captured in the measurement of Fig. 4.3.1**j**. As the bottom QD changes character at $V_\mathrm{T} = V_3$ voltage, there is a short section between $V_\mathrm{T} = V_2$ and V_3 where both QDs are in the singlet ground state and discontinuity of

the top YSR excitation becomes visible again. By further increasing V_T, the ground state of the top QD becomes the doublet establishing a $|2,1\rangle$ ground state character. Since the model does not include relaxation, higher-order processes are also present in the simulations, which are usually not visible in measurements. The lines not discussed here (e.g. the one with the gray circle) belong to this category, therefore they can be considered only virtual states. To summarize, all main features can be explained with the interaction of "eye-shaped" YSR_T and the shifting YSR_B states with the additional triplet sector in the middle of the map.

4.5 Conclusions

To summarize, we have found strong interactions between parallel YSR states realized in double InAs nanowires connected by an epitaxial Al shell. The small geometrical distance between the QDs resulted in capacitive coupling, while the shared epitaxial Al source contact enabled hybridization via the SC vacuum. The latter one allowed the emergence of an Andreev molecular state, whose spectrum was explored as a function of the QD level positions for the first time. The detected spectroscopic features were reproduced by our numerical calculations, where the dominance of EC and CAR was pointed out.

Since our work has been published (see Ref. 180), many researches reported the signature of an Andreev molecule realized in weak links connected by a SC[209–212]. In those articles, as suggested in Ref. 213, the phase dependent hybridization of ABSs was investigated. Engineering an Andreev molecule via the coherent coupling was managed in these studies, however, the level tunability povided by the QDs is lacking from them. These works and the huge attention they attracted proves that the Andreev molecule is a hot topic and has a lot of merits in the next generation of superconducting circuits.

Chapter 5

Superconducting island-based polyatomic molecule

Complex molecular states are natural manifestations of favorable coupling between atomic sites. Electron hoppings connecting adjacent cores contribute to stabilized chains extending the local peculiarities in the long range. Its simplest realization is the H_2 molecule, yet severely complicated structures do exist built from multiple atoms. Current studies of quantum electronics heavily focus on novel SC-QD arrays, where the controlled manipulation of the interacting sites is a cardinal question. Among these arrays, a wide range of Andreev molecule concepts can be found, which are collected in Fig. 5.0.1.

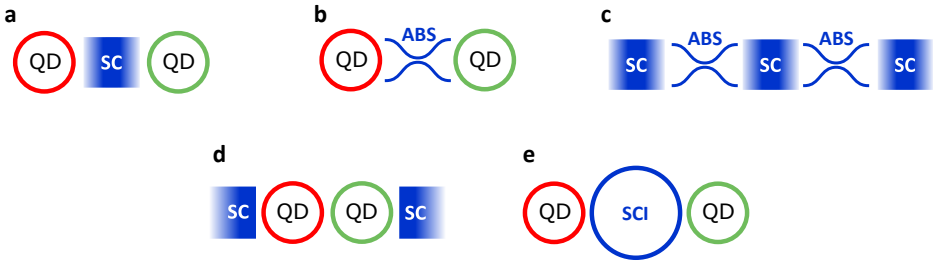

Figure 5.0.1: **Zoo of Andreev molecules.** **a** 2-atomic, QD-based Andreev molecule connected by a bulk SC and **b** a central ABS. In both systems, the CAR and EC hybridize the level-tunable states. **c** Coherent coupling of conductive channels hosting ABSs. Here the control parameter is the superconducting phase. **d** Double QDs in series attached to two SCs. The ABSs residing in the red and green QDs can couple only via electron tunneling. **e** 3-atomic Andreev molecule of a QD-SCI-QD structure as a generalization of panel **a** in the Coulombic limit.

In the previous Chapter, we have seen that a 2-atomic Andreev molecule can be constructed from the hybridization of two QDs via a bulk SC shown in Fig. 5.0.1**a**. This is what we consider the main building block of the Kiatev chain[172,180]. Other works have also reported that the coupling between the QDs can be mediated by a central ABS, which is sketched in panel **b**. In this setup, the ABS assists CAR and EC processes in a controlled, tunable manner as outlined in Refs. 175,176 and 214. A third concept of the Andreev molecule is proposed by the coherent coupling of ABSs[209–212] interpreted in the traditional approach, which we discussed in Subsection 2.2.4. Two such states can be linked through a joint SC as drawn in Fig. 5.0.1**c**, where the control parameter is the superconducting phase difference, however, the level tunability is lacking in these systems. Other alternative definitions of the Andreev molecule also exist, e.g. a SC-QD-QD-SC array with two ABSs tunnel coupled in series[202] as sketched in panel **d**, although this structure is not compatible with the Kitaev chain model. As a last candidate, we highlight a QD-SCI-QD polyatomic molecule introduced in panel **e**, whose behavior is under the scope in

this Chapter. Since it is viewed as the Coulombic limit of the Andreev molecule introduced in panel **a** and Chapter 4, next we make a quick comparison of the two systems.

In the 2-atomic Andreev molecule, when the bound states are brought close to each other in energy $\Delta_{\mathrm{YSR,L(R)}}$ as shown by the red and green lines in Fig. 5.0.2**a**, they couple via CAR or EC exhibiting bonding and anti-bonding combinations. The mixed states split up, and the one with Δ_{AM} becomes the lowest energy excitation as explained by the pink line, analogously to conventional molecules.

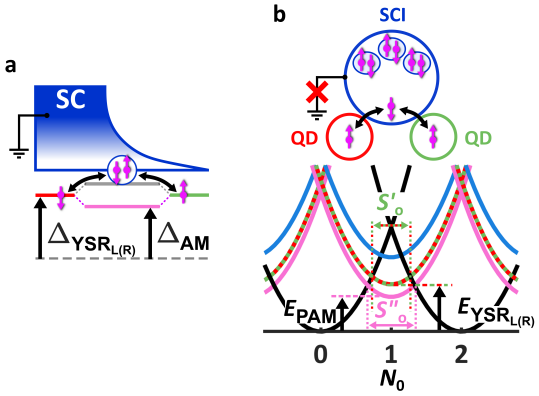

Figure 5.0.2: **Concept of different Andreev molecules. a** Excitation diagram of a 2-atomic Andreev molecule hosted by parallel YSR states (red and green) and a bulk SC. When brought to similar energies $\Delta_{\mathrm{YSR,L(R)}}$, they hybridize via EC or CAR and form a molecule (pink) accessible at energy $\Delta_{\mathrm{AM}} < \Delta_{\mathrm{YSR,L(R)}}$. **b** Energy relations of a double QD-SCI hybrid as a function of the SCI electron number, N_0 near the $\Delta \approx U_{\mathrm{SC}}$ limit (Δ is the superconducting gap, U_{SC} is the SCI charging energy). The black parabolas belong to the even ($2n_0$), the blue one ($2n_0+1$) occupations. The offset of the odd parabola is lowered if a YSR singlet is present (red-green) with energy $E_{\mathrm{YSR,L(R)}}$ as discussed in Fig. 2.3.3 **b**. The $2n_0+1$ sector is further stabilized when two such YSR states couple to an unpaired quasi-particle and constitute a 3-electron state, namely a polyatomic Andreev molecule at energy E_{PAM} (pink). The odd sector of the SCI expands to $S''_o > S'_o$ value.

Exploiting the Coulomb-aided YSR states discussed in Subsection 2.3.3, one can connect the two QDs via a SCI, which behaves as a central atom as illustrated on the top of Fig. 5.0.2**b**. In this conceptually different approach, two, separate Coulomb-aided YSR states existing with similar energies $E_{\mathrm{YSR,L(R)}}$ (red-green parabolas plotted as a function of the SCI charge N_0 in panel **b**) can couple to the same quasi-particle of the SCI thereby sharing the unpaired electron between each other. Instinctively, the YSR states are expected to hybridize and create a 3-electron Andreev molecule at energy $E_{\mathrm{PAM}} < E_{\mathrm{YSR,L(R)}}$. As a result, the $2n_0+1$ odd sector of the SCI is stabilized, which is highlighted by the pink curve in Fig.5.0.2**b** the $S''_o > S'_o$ relation, the measure of the even-odd effect strength according to Eq. 2.3.5. In the Andreev molecule family, we call this 3-particle bond as a polyatomic Andreev molecule[194]. The speciality of this artificial structure is that 3 atoms are coupled and it consists of two different classes: normal atoms and a superconducting one. In this sense, we could say that it is analogous to the H_2O. These unique, polyatomic molecules have a huge potent these days since they can be engineered to realize Kitaev chains, the highly desired topological superconducting prototype system. Beyond this, such SCI hybrid is also a fully tunable skeleton of a Majorana-box[158,215,216] or parafermionic platforms[152].

In this Chapter, we present the first realization of a polyatomic Andreev molecule in parallel InAs nanowires. We perform Coulomb blockade spectroscopy in 3 terminals to capture the ground state energies of different QD occupations. The measurement of the S_o/S_e spacing ratio from Eq. 2.3.5 is utilized as a tool to approve the presence of a polyatomic Andreev molecule and estimate its energy. We support our experimental findings with numerical simulations

qualitatively reproducing the behavior of our system[1]. Since the spins of the shared quasiparticle and on the QDs are defined by the first order exchange interaction, a ferromagnetic coupling[217] via a superexchange is expected which is deduced by our model as well.

In addition to the polyatomic Andreev molecule, we also report the hints of CPS signals in the weak coupling limit. This requires the SCI to be charged by 2e instead of single electrons, or with a different wording, the even-odd effect must vanish. Once this condition is satisfied, in principle, the circuit can operate as a regular Cooper pair splitter which we introduced in Subsection 2.2.3 and Chapter 3. We introduce this behavior in Appendix A.2.

5.1 Device outline

The investigated system is shown in Figs. 5.1.1**a-b**. The fabrication process of this device resembled the one with the CPS experiments in Chapter 3. Double, parallel InAs nanowires (brown) were grown and merged by an epitaxially evaporated Al shell (blue) covering 2 facets axially[179]. These nanowires were from the same batch as used for the device introduced in Chapter 3. The Al was partially removed by wet chemical etching both on the top and on the bottom leaving a $\sim 700\,\mathrm{nm}$ long SCI in the middle as shown by the SEM in Fig. 5.1.1**a**. To obtain such an island, 2 large, rectangular-shaped etching windows were opened with a separation of $\sim 900\,\mathrm{nm}$ to compensate $\sim 100\,\mathrm{nm}$ underetching from both sides. Difficulties similar to the ones in Chapter 3 arose during the fabrication process: 4 Ti/Au electrodes (yellow) had to be defined by EBL such that each one contacted only one nanowire segment individually. This required again $< 30\,\mathrm{nm}$ precision in the alignment of the EBL while a relatively high yield. Together with the contact electrodes, 2 wide plunger gates were deposited next to the SCI to tune its electron occupation. In a distinct EBL step, large space-periodic finger gates were installed surrounding the nanowires to control the transport. The selected devices (sorted by a SEM study) were connected to the bonding pads in a final EBL step (for further details, see Appendix A.3). Altogether, in the optimization process, ~ 30 samples (with 1-2 devices per chip) were produced, from which 2 were studied intensively. In the following, we focus on the specific sample from Fig. 5.1.1**a** featuring the polyatomic Andreev molecule.

The sample was cooled down in a dilution refrigerator to 40 mK to perform low-temperature transport measurements. In the bottom left (red), bottom right (green), and top right (purple) segments QDs were formed by adjusting the voltage on the outer finger gates, and the middle ones were used to tune their level positions as illustrated in Fig. 5.1.1**b**. The top left electrode performed as a source electrode biased with V_{AC}, while the rest 3 acted as drains biased with DC voltage V_{SD}. Differential conductances $G_{\mathrm{BL}} = dI_{\mathrm{BL}}/V_{\mathrm{AC}}$ and $G_{\mathrm{BR}} = dI_{\mathrm{BR}}/V_{\mathrm{AC}}$ in the bottom left and bottom right branches were measured simultaneously via the red and green QDs, respectively. The top right arm was floated in these experiments. In this setup, effectively 2 parallel channels were probed: one of them consisted of the the SCI and the red QD, the other one the SCI and the green QD in series. We note that the direct tunneling between the red and green QDs was excluded and they were coupled only through the SCI[190].

To characterize the SCI, first, we electrostatically decoupled it from the environment by adjusting the voltage on the finger gates between the source and the SCI in Fig. 5.1.1**a-b**. We accomplished finite-bias spectroscopy as a function of plunger gate voltage V_{SC} through the bottom right arm, which is shown in Fig. 5.1.1**c**. Here the green QD was set deep in Coulomb blockade to serve as a cotunneling probe. Within the white dashed lines, N_0 is even, while the odd states can not be resolved suggesting the close-to-2e periodic limit in the SCI diamonds with $4U_{\mathrm{SC}}$ total height[218], where U_{SC} is the charging energy. The lowest bias voltage where

[1]The sample fabrication, the measurements, and the data analysis were performed by Olivér Kürtössy. The theoretical model was developed by Dr. Zoltál Scherübl and Mihály Bodócs. The project was guided by Dr. Péter Makk and Dr. Szabolcs Csonka.

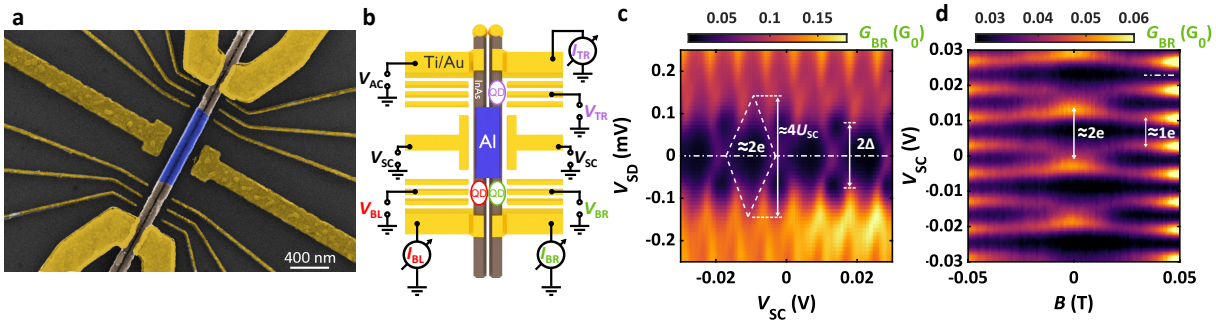

Figure 5.1.1: **Device outline & decoupled SCI. a** SEM micrograph of the device measured in multiple terminals. The epitaxial Al (blue) was etched away along the wires except the middle thereby forming an island connecting the separate InAs nanowires (brown). 4 Ti/Au electrodes as normal contacts and finger gates were installed to gain a high level of control in the transport. **b** Schematic illustration about the measurement setup. The AC source was applied to the top left contact, whereas the differential conductance was measured simultaneously on the bottom left (red) and bottom right (green) drain electrodes. While the red and green QDs were formed with the outer finger gates, their level positions were tuned by plunger gate voltages V_{BL} and V_{BR}, respectively. The SCI was gated by V_{SC}. **c** Coulomb blockade spectroscopy of the SCI through the bottom right drain. Since $\Delta \approx U_{\mathrm{SC}}$, the diamonds have an intrinsic close-to-2e periodicity yielding $4U_{\mathrm{SC}}$. 2Δ is read off from the border of the 1e periodic patterns in the energy spectrum. **d** Development of the zero-bias SCI resonances (along the white dashed line from panel **c**) in an out-of-plane magnetic field. The 2e periodic behavior excluding the odd occupations turns into 1e one as the superconductivity is destroyed.

1e periodic pattern appears is assigned to the superconducting gap with excitation energy Δ. From the spectrum $U_{\mathrm{SC}} \approx 85\,\mu\mathrm{eV}$ and $\Delta \approx 75\,\mu\mathrm{eV}$ were estimated with $\delta_{\mathrm{SC}} \approx 0$ unresolvable level spacing allowing to use the electrostatic model of Eq. 2.3.3. Applying an out-of-plain magnetic field destroys the superconductivity, hence Δ is decreased continuously, and the odd filling becomes available. The 2e charge states gain less energy from the pairing and the S_o/S_e even-odd amplitude of Eq. 2.3.5 developes from 0 to 1. This is presented in Fig. 5.1.1**d** where 2e zero-bias charging (taken along the dotted-dashed line from panel **c**) turns into 1e periodic typical for normal metallic islands[138–141].

5.2 Even-odd stabilization & polyatomic Andreev molecule

Now we explore the interaction between the SCI and the 2 QDs. Figs. 5.2.1**a-b** show the zero-bias G_{BL} and G_{BR} measured via the red ("BL") and green ("BR") QDs as a function of their plunger gate voltages, V_{BL} and V_{BR}. In the stability maps, there are several resonant lines with 3 dominant lever arms. The one indicated by the red arrows belongs to the red QD, which is mostly visible in panel **a**, where it is the local signal. The resonances marked by the green arrows are attributed to the green QD, therefore they dominate in panel **b**. The diagonal lines with the cyan arrows are the SCI resonances, which appear in both diagrams as its signal is measured in G_{BL} and G_{BR} as well. Finite-bias spectroscopies were performed along the white dashed and dotted lines in the normal state (achieved by a $B = 100\,\mathrm{mT}$ out-of-plain magnetic field) revealing the Coulomb diamonds of the red and green QDs in Figs. 5.2.1**c** and 5.2.1**d**, respectively. From the size of the diamonds in the examined range, charging energies and level spacings $U_{\mathrm{BL}} \approx 0.4\,\mathrm{meV}$ and $\delta_{\mathrm{BL}} \approx 0.1\,\mathrm{meV}$ were found for the red QD, while $U_{\mathrm{BR}} \approx 1.2\,\mathrm{meV}$ and $\delta_{\mathrm{BR}} \approx 0.35\,\mathrm{meV}$ were derived for the green one.

Due to the complexity of our system, instead of tuning both QDs together or performing bias spectroscopy in the superconducting state (for such measurement see Appendix A.2), we recorded the zero-bias conductance of the SCI and the green (red) QD controlled by their plunger gate voltages, V_{SC} and $V_{\mathrm{BR(BL)}}$, while the on-site energy of the red (green) one was fixed. This

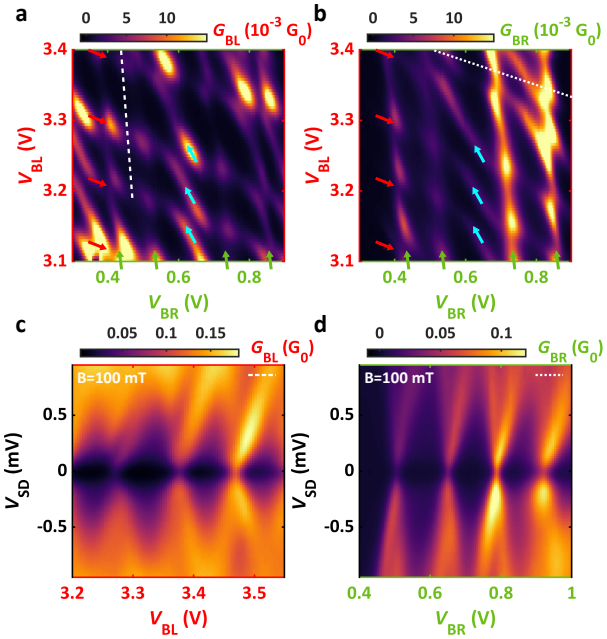

Figure 5.2.1: **Characterization of the QDs. a** G_{BL} and **b** G_{BL} versus V_{BL} and V_{BR} plunger gate voltages in the superconducting states. Resonances with 3 different slopes are present: the ones indicated by the red, green, and cyan arrows belong to the red, green QD, and the SCI, respectively. **c-d** Finite-bias spectroscopy along the white dashed and dotted line from panels **a-b** in the normal state. The charging energies of the QDs exceed the SCI's one, while there is a finite level spacing on them as well.

idea simplifies the problem to a double-QD stability diagram whose structure can be examined as a function of the occupation of the 3rd (untuned) QD. A further advantage of this routine is that the even-odd amplitude S_o/S_e of the SCI (discussed in Section 2.3) is extracted directly for a given QD configuration, which reflects the ground state energy of the system regarding of Eq. 2.3.5. Hence, the Coulomb-aided YSR states that might appear in the odd SCI electron occupation can be probed with simple Coulomb-blockade spectroscopy by measuring the distance between the subsequent resonance peaks. To maintain the level position in the 3rd, untuned QD, the gate voltage on its plunger gate was compensated while the other one was ramped. The size of the voltage compensation was defined by the lever arm ratio referring to the cross capacitance strength of the red and green QDs and their gate electrodes, which was $\alpha_{\mathrm{BL,BR}} \approx 1/6$. This quantity was $\alpha_{\mathrm{BL(BR),SC}} \approx 1/10$ for the red (green) QD and the SCI. Since V_{SC} was varied in a small window compared to $V_{\mathrm{BL(BR)}}$, its gating effect imposed on the untuned red (green) QD was neglected.

Fig. 5.2.2**a** shows G_{BR} as a function of V_{BR} and V_{SC} exhibiting a honeycomb pattern well-known for double QDs[65]. The resonance lines sensitive to V_{BR} belong to the green QD (see the gray arrows), whereas the diagonal ones correspond to the SCI charge degeneracies (see the cyan arrows). The hybridization between the SCI and the green QD is already conspicuous from the bendings and the shape of the honeycomb. Let us introduce the notation $|m, N_0, n\rangle = |m\rangle_{\mathrm{BL}} \otimes |N_0\rangle_{\mathrm{SCI}} \otimes |n\rangle_{\mathrm{BR}}$, where m, N_0, n address the electron number in the red QD, the SCI, and the green QD. We express the even electron parity of the SCI by $N_0 = 2n_0$, and the odd one with $N_0 = 2n_0 + 1$ ($n_0 \in \mathbb{N}$ for both cases) like we did in Section 2.3. In this particular measurement, the red QD was set into blockade with an even number of electrons, thus $|0, N_0, n\rangle$ states were studied as indicated by the inset. At $V_{\mathrm{BR}} \approx 0.6\,\mathrm{V}$ with $|0, N_0, 2\rangle$ even number of electrons in both QDs, the SCI shows a quasi 2e charging behavior with spacing S_e marked by the blue arrow (**I.**), similarly to Fig. 5.1.1**c**. No YSR states are formed as illustrated in Fig. 5.2.2**c I.**. Nonetheless, tuning the green QD to odd occupation at $V_{\mathrm{BR}} \approx 0.45\,\mathrm{V}$ ($|0, N_0, 1\rangle$ states), the resonance of the SCI splits and an even-odd effect is observable with S'_o and $S'_e < S_e$

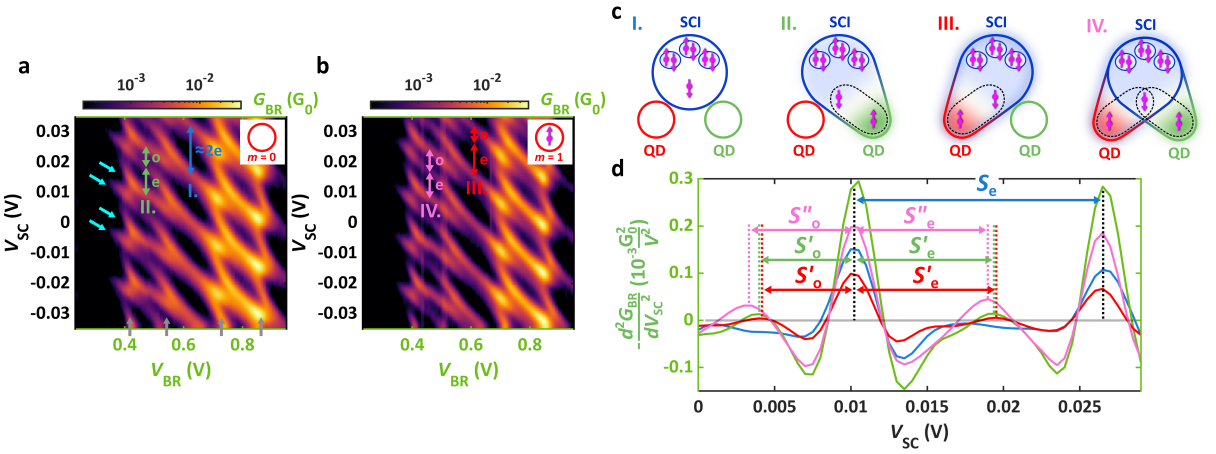

Figure 5.2.2: **Stability diagrams at different QD occupations.** **a** Zero-bias stability map vs V_{BR} and V_{SC} via the SCI-green double QD with even number of electrons in the red QD. For $|0, N_0, 2\rangle$ ($V_{\mathrm{BR}} = 0.6\,\mathrm{V}$), 2e charging, for $|0, N_0, 1\rangle$, even-odd effect is obtained on the SCI. **b** Same as **a**, but captured at odd occupation of the red QD. The $|1, N_0, 2\rangle$ state at $V_{\mathrm{BR}} = 0.6\,\mathrm{V}$ exhibits roughly the same diamond spacing as $|0, N_0, 1\rangle$ one, nevertheless, the odd state of the SCI is extended at $V_{\mathrm{BR}} = 0.45\,\mathrm{V}$ when the filling of the QDs and the SCI is $|1, N_0, 1\rangle$. **c** Illustration of the interaction between the QDs and a single quai-particle in the SCI. While scenario **I.** with $|0, N_0, 2\rangle$ represents a non-interacting picture, scenarios **II.** and **III.** with $|0, N_0, 1\rangle$ and $|1, N_0, 2\rangle$, yield distinct YSR in the red and green QDs. In the case of **IV.** with $|1, 2n_0 + 1, 1\rangle$, the two YSR states share the unpaired electron. **d** Peak analysis of SCI resonance lines taken along the colored arrows in panels **a-b**. $S''_o > S'_o$ fulfills the expectation predicting a polyatomic Andreev molecule.

spacings indicated by the green arrows (**II.**). Regarding of Eqs. 2.3.4 and 2.3.5, the effective Δ is reduced to $E_{\mathrm{YSR,R}}$ suggesting the presence of a Coulomb-aided YSR singlet composed by a quasi-particle in the SCI and the electron of the green QD as outlined in Fig. 2.3.3**b** and studied in Ref. 150. The character of this singlet can be described by the $|0, 2n_0 + 1, 1\rangle$ states. Whereas the SCI and the green QD are strongly hybridized, the red one does not interact with them as sketched in panel Fig. 5.2.2**c II.**.

We now examine how the stability diagram deviates if the red QD is filled with a single electron as well. Fig. 5.2.2**b** demonstrates the same map as in panel **a** but recorded with $|1, N_0, n\rangle$ configurations. At $V_{\mathrm{BR}} \approx 0.6\,\mathrm{V}$ the quasi 2e charging captured in panel **a** is replaced with an even-odd one with similar S'_o and S'_e highlighted by the red arrows (**III.**). The even-odd amplitude here is almost identical to the case of the $|0, N_0, 1\rangle$ filling of **II.**. We conclude that in this region a different YSR state is formed between the SCI and the red QD (see Fig. 5.2.2**c III.**) with $|1, 2n_0 + 1, 0\rangle$ character and energy $E_{\mathrm{YSR,L}} \approx E_{\mathrm{YSR,R}}$.

Bringing both QDs to odd occupations with $|1, N_0, 1\rangle$ (visible at $V_{\mathrm{BR}} \approx 0.45\,\mathrm{V}$), the size of the SCI odd state, S''_o of $|1, 2n_0 + 1, 1\rangle$, expands further revealed by the pink arrows (**IV.**). The stabilization of S''_o entails the ground state energy being below both $E_{\mathrm{YSR,L}}$ and $E_{\mathrm{YSR,R}}$, which originates from the coupling of the green and red YSR states as predicted in the introduction and by panel **c IV.**. The same tendency was captured in the stability sweeps if the role of the red and green QD was swapped, which is detailed below.

To quantify the effect presented in Figs. 5.2.2**a-c**, we plot $p = -d^2G_{\mathrm{BR}}/dV_{\mathrm{SC}}^2$ in Fig. 5.2.2**d** along the **I.-IV.** colored arrows for all 4 distinct QD parity ($m, n = \{0, 1\}$) to obtain the distance of the SCI peak positions and S_e, S_o, S'_o and S''_o precisely. All curves with a certain color belong to the cuts taken along the corresponding color of the arrows. In the analysis, we consider peaks only with the $p \geq 0$ condition satisfied, which corresponds to the position of the Coulomb resonances. As one can see the $N_0 = 0 \longleftrightarrow 1$ transitions (secondary peaks) and $N_0 = 1 \longleftrightarrow 2$ transitions (main peaks) on the SCI are strongly asymmetric in amplitude,

which we comment on later (at Fig. 5.2.6**b**). For better transparency, we center the main peaks of the curves to $V_{\mathrm{SC}} = 0.01\,\mathrm{V}$ and compare them accordingly. As visible, the blue line ($|0, N_0, 2\rangle$ states) retains only the main peaks with $S_e = 16.5\,\mathrm{mV}$ exposing the 2e charging. In the red and green curves ($|1, N_0, 2\rangle$ and $|0, N_0, 1\rangle$ states) the secondary peaks pop up at almost the same V_{SC} values providing $S'_o = 5\,\mathrm{mV}$ odd state width. Regarding of Eq. 2.3.5, the single Coulomb-aided YSR states of $|1, 2n_0 + 1, 2\rangle$ and $|0, 2n_0 + 1, 1\rangle$ reside in the QDs at energy $E_{\mathrm{YSR,L(R)}} \approx 33\,\mu\mathrm{eV}$. Compared to them, the secondary peaks of the pink line ($|1, N_0, 1\rangle$ state) have substantially higher negative shifts with $S''_o = 6\,\mathrm{mV}$. Using 1e periodicity as a reference, the relative discrepancy in the spacing of the two, coupled YSR states (case **IV.**) compared to a single one (case **II.** and **III.**) is significant, $\Delta S = 2(S''_o - S'_o)/S_e \approx 12\%$, which assumes a polyatomic Andreev molecule existing at energy $E_{\mathrm{PAM}} \approx 23\,\mu\mathrm{eV}$ ($10\,\mu\mathrm{eV}$ below the single YSR states) in the $|1, 2n_0 + 1, 1\rangle$ configurations.

5.2.1 Additional data

In the stability maps, qualitatively the same behavior as in Fig. 5.2.2 was obtained, when the red QD was tuned together with the SCI and green QD occupation was fixed instead. Fig. 5.2.3**a** demonstrates G_{BL} at zero bias as a function of V_{BL} and V_{SC} with even number of electrons in the green QD (as shown by the inset) allowing to explore the even-odd effect of the $|m, N_0, 2\rangle$ states. Here the gray arrows indicate the resonances of the red QD, while the cyan ones mark the SCI again. The vertical pattern at $V_{\mathrm{BL}} = 3.2\,\mathrm{V}$ exhibits the 2e charging of the $|0, N_0, 2\rangle$ states (**I.**) as expected from the previous results of Fig. 5.2.2**a**. At $V_{\mathrm{BL}} = 3.27\,\mathrm{V}$, one can see the splitting of the SCI resonances yielding a finite even-odd effect in the $|1, N_0, 2\rangle$ configurations (**III.**, see the red arrows), which corresponds to the signature of the Coulomb-aided YSR singlet living in the red QD. Fig. 5.2.3**b** shows the same map as panel **a** with the difference of having a single electron in the green QD, thereby mapping the $|m, N_0, 1\rangle$ sectors. Here the 2e charging of case **I.** from panel **a** turns into a single one of case **II.** ($|0, N_0, 1\rangle$) marked by the green arrows, which is the evidence of a YSR state formed in the green QD captured now in the signal of the bottom left arm. The $|1, N_0, 1\rangle$ configurations (**IV.**) have the widest odd sector gain $S''_0 > S'_0$ as depicted by the pink arrows. These observations concluded from Figs. 5.2.3**a-b** are consistent with the ones in Figs. 5.2.2**a-b**.

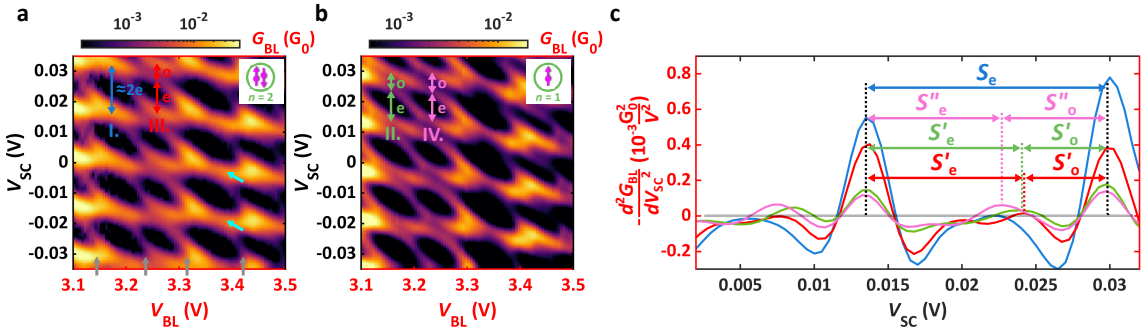

Figure 5.2.3: **Stability diagrams at different QD occupations (with swapped red and green QD roles). a** Zero-bias stability sweep as a function of V_{BL} and V_{SC} via the SCI-red double QD with even number of electrons in the green QD. The $|0, N_0, 2\rangle$ diamonds (**I.**) at ($V_{\mathrm{BL}} = 3.2\,\mathrm{V}$) reflect 2e charging, for $|1, N_0, 2\rangle$ (at $V_{\mathrm{BL}} = 3.27\,\mathrm{V}$, **III.**), the even-odd effect is recovered. **b** Same as **a**, but with $|m, N_0, 1\rangle$ configurations examined. The odd sector of the SCI, $|1, N_0, 1\rangle$, is broadened further from S'_0 (III.) to S''_o (IV.) revealed by the pink arrows. This suggests the hybridization of the YSR states captured now in both G_{BL} and G_{BR}. **d** Peak analysis of SCI resonance lines taken along the colored arrows in panels **a-b**. $S''_o > S'_o$ fulfills the expectation predicting a polyatomic Andreev molecule.

The analysis introduced in Fig. 5.2.2**d** applied for the data of G_{BL} in Figs. 5.2.3**a-b** gives the same outcome, which is shown in Fig. 5.2.3**c** for the sake of completeness. The calculated

$q = -d^2G_{\mathrm{BL}}/dV_{\mathrm{SC}}^2$ curves are taken along the colored arrows, and although the secondary peaks are rather small, $q \geq 0$ and the $S_o' < S_o''$ still hold. One can see that the highlighted odd spacings S_o', S_o'' of the pink, green, and red signals are in excellent agreement with the ones in Fig. 5.2.2**d**, and we estimate $E_{\mathrm{YSR,L(R)}} \approx 32\,\mu$eV and $E_{\mathrm{PAM}} \approx 16\,\mu$eV from this set of data. This series of measurements strengthens our hypothesis about the polyatomic Andreev molecule spatially extending over the QDs and the SCI since the modulation of the even-odd effect was captured in both G_{BL} and G_{BR}.

To summarize it so far, we claim that the states $|2m+1, 2n_0+1, 2n\rangle$ and $|2m, 2n_0+1, 2n+1\rangle$ imply a single Coulomb-aided YSR singlet residing in the hybrid (either in the red or green QDs). Moreover, the $|2m+1, 2n_0+1, 2n+1\rangle$ configuration, which we simplify to $\Psi_{\mathrm{PAM}} = |1,1,1\rangle$, belongs to the polyatomic Andreev molecule, a pair of Coulomb-aided YSR states sharing the quasi-particle of the SCI as shown in Fig. 5.2.2**c IV.** earlier.

5.2.2 Modeling

To confirm the presence of the polyatomic Andreev molecule in our system, we developed a simple rate equation model to reproduce the main experimental findings of Fig. 5.2.2. We used the draft of a single Coulomb-aided YSR singlet in Eqs. 2.3.6 and 2.3.7, which we complemented with a second QD attached to the SCI.

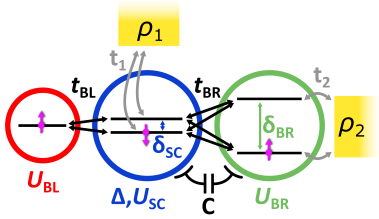

Figure 5.2.4: **Schematics of the polyatomic Andreev molecule model.** The SCI and the green QD are modeled by 2-2 orbitals, while the red QD is by a single one. All tunnel couplings are shown by the arrows between the levels. The SCI and the green QDs are connected to the environment via 1-1 normal leads with constant DOS ρ_1, ρ_2 (yellow rectangles).

The schematic of the model is illustrated in Fig. 5.2.4. The SCI consists of two orbitals in the Richardson picture with a common charging energy U_{SC} and superconducting gap Δ, exactly as H_{SCI} in Eq. 2.3.7. One of the orbital energy ϵ_{SC1} is chosen to be 0, thus the level spacing is set small $\delta_{\mathrm{SC}} = \epsilon_{\mathrm{SC2}} = U_{\mathrm{SC}}/100$ typical for metallic islands. The green QD is treated in the 2-orbital Anderson model with charging energy U_{BR} and level spacing $\delta_{\mathrm{BR}} = \epsilon_{\mathrm{BR2}}$ ($\epsilon_{\mathrm{BR1}} = 0$ applies here as well), which is effectively the same as H_{QD} in Eq. 2.3.7 or 2.1.4. The 2 orbitals on the green QD are necessary to obtain the even parity diamond size of the SCI (otherwise, two half-infinite diamonds are given) and to avoid any finite-size effects in the stability maps. The red QD is handled as a single level like in Eq. 2.1.6 to keep the model minimal. The SCI is tunnel coupled to both levels of the green QD and the single level of the red QD, however, the QDs are not connected directly as shown in Fig. 5.2.4. We also consider the mutual capacitance C between the SCI and the green QD, but the cross capacitances to the red QD are neglected. The total Fock-space Hamiltonian of the system is composed as

$$H_{\mathrm{PAM}} = H_{\mathrm{SCI}} + H_{\mathrm{BR}} + H_{\mathrm{BL}} + H_{\mathrm{TBR}} + H_{\mathrm{TBL}}, \tag{5.2.1}$$

where

$$
\begin{aligned}
H_{\mathrm{SCI}} &= \left(\varepsilon_{\mathrm{SC}} + \frac{\Delta}{2}\right)\sum_i n_{\mathrm{SC}i} + \left(\sum_i n_{\mathrm{SC}i}\right)\left(\sum_j n_{\mathrm{SC}j} - 1\right)\frac{U_{\mathrm{SC}}}{2} + \sum_i n_{\mathrm{SC}i}\epsilon_{\mathrm{SC}i} \\
&\quad - \frac{\Delta}{N}\sum_{i,j} c^{\dagger}_{\mathrm{SC}i\uparrow} c^{\dagger}_{\mathrm{SC}i\downarrow} c_{\mathrm{SC}j\downarrow} c_{\mathrm{SC}j\uparrow} \\
H_{\mathrm{BR}} &= \varepsilon_{\mathrm{BR}}\sum_\alpha n_{\mathrm{BR}\alpha} + \left(\sum_\alpha n_{\mathrm{BR}\alpha}\right)\left(\sum_\beta n_{\mathrm{BR}\beta} - 1\right)\frac{U_{\mathrm{BR}}}{2} + \sum_\alpha n_{\mathrm{BR}\alpha}\epsilon_{\mathrm{BR}\alpha} \\
H_{\mathrm{BL}} &= \varepsilon_{\mathrm{BL}} n_{\mathrm{BL}} + \frac{U_{\mathrm{BL}}}{2} n_{\mathrm{BL}}\left(n_{\mathrm{BL}} - 1\right) \\
H_{\mathrm{TBR}} &= t_{\mathrm{BR}}\left(\sum_{\alpha i\sigma} d^{\dagger}_{\mathrm{BR}\alpha\sigma} c_{\mathrm{SC}i\sigma} + c^{\dagger}_{\mathrm{SC}i\sigma} d_{\mathrm{BR}\alpha\sigma}\right) + C\left(\sum_i n_{\mathrm{SC}i}\right)\left(\sum_\alpha n_{\mathrm{BR}\alpha}\right) \\
H_{\mathrm{TBL}} &= t_{\mathrm{BL}}\left(\sum_{i\sigma} d^{\dagger}_{\mathrm{BL}\sigma} c_{\mathrm{SC}i\sigma} + c^{\dagger}_{\mathrm{SC}i\sigma} d_{\mathrm{BL}\sigma}\right).
\end{aligned}
\tag{5.2.2}
$$

In the equations above, $n_{\mathrm{BR}\alpha(\mathrm{BL})}$ is the particle number operator of orbital α in the green (red) QD with $d^{(\dagger)}_{\mathrm{BR}\alpha[\mathrm{BL}]\sigma}$ being the annihilation (creation) operator of an electron with spin σ, while $\varepsilon_{\mathrm{BR(BL)}}$ is the green [red] QD on-site energy. In addition, $n_{\mathrm{SC}i}$ is the particle number operator of orbital i in the SCI with $c^{(\dagger)}_{\mathrm{SC}i\sigma}$ being the annihilation (creation) operator of an electron with spin σ, and $\varepsilon_{\mathrm{SC}}$ is SCI on-site energy. We give a reminder that $n(m) = \langle n_{\mathrm{BR(BL)}}\rangle$ and $N_0 = \langle n_{\mathrm{SC}}\rangle$ with our previous notations. $t_{\mathrm{BR(BL)}}$ is the hopping amplitude between one of the levels of the SCI and the green (red) QD. The origin of the $N = 2$ normalization factor in H_{SCI} was explained at Eq. 2.3.9.

Direct diagonalization was performed on H_{PAM} to derive the ground state wave functions and the electron occupations as a function of $\varepsilon_{\mathrm{SC}}, \varepsilon_{\mathrm{BR}}$, and $\varepsilon_{\mathrm{BL}}$. Transport through the green QD-SCI double QD (while coupled to the red one as well) was calculated by solving the Master equation in the stationary limit, likewise we did for the 2-atomic Andreev molecule model in Chapter 4:

$$
\frac{dP_\chi}{dt} = \sum_{\chi'\neq\chi}\left(W_{\chi\chi'}P_{\chi'} - W_{\chi'\chi}P_\chi\right). \tag{5.2.3}
$$

P_χ is the occupation probability of the eigenstate χ with the constriction of $\sum_\chi P_\chi = 1$. $W_{\chi\chi'}$ declares the total transition rate from $|\chi'\rangle$ state to $|\chi\rangle$, which is calculated by Fermi's golden rule[94]. $W_{\chi\chi'}$ is the sum of the 4 components

$$
\begin{aligned}
W_{\chi'\chi}\left(c^{\dagger}_{\mathrm{SC}i\sigma}\right) &= \Gamma_1\left|\langle\chi'|\, c^{\dagger}_{\mathrm{SC}i\sigma}\,|\chi\rangle\right|^2 f\left(E_\chi - E_{\chi'} - eV_{\mathrm{AC}}\right) \\
W_{\chi'\chi}\left(c_{\mathrm{SC}i\sigma}\right) &= \Gamma_1\left|\langle\chi'|\, c_{\mathrm{SC}i\sigma}\,|\chi\rangle\right|^2\left(1 - f\left(E_{\chi'} - E_\chi - eV_{\mathrm{AC}}\right)\right) \\
W_{\chi'\chi}\left(d^{\dagger}_{\mathrm{BR}\alpha\sigma}\right) &= \Gamma_2\left|\langle\chi'|\, d^{\dagger}_{\mathrm{BR}\alpha\sigma}\,|\chi\rangle\right|^2 f\left(E_\chi - E_{\chi'} + eV_{\mathrm{AC}}\right) \\
W_{\chi'\chi}\left(d_{\mathrm{BR}\alpha\sigma}\right) &= \Gamma_2\left|\langle\chi'|\, d_{\mathrm{BR}\alpha\sigma}\,|\chi\rangle\right|^2\left(1 - f\left(E_{\chi'} - E_\chi + eV_{\mathrm{AC}}\right)\right).
\end{aligned}
\tag{5.2.4}
$$

$\Gamma_{1(2)} = \pi t^2_{1(2)}\rho_{1(2)}(0)$ is the coupling strength of the SCI (green QD) to one of the normal leads with DOS $\rho_{1(2)}(0) = \text{const.}$ as depicted in Fig. 5.2.4. The stationary current is given by solving

Eq. 5.2.3 at $dP_\chi/dt = 0$. We calculate the differential conductance at the green QD-normal lead interface as

$$G_{\mathrm{BR}} = \frac{dI_{\mathrm{BR}}}{dV_{\mathrm{AC}}} = \frac{e}{\hbar V_{\mathrm{AC}}} \sum_{\alpha\chi\chi'\sigma} \left(W_{\chi'\chi}\left(d_{\mathrm{BR}\alpha\sigma}\right) - W_{\chi'\chi}\left(d^\dagger_{\mathrm{BR}\alpha\sigma}\right) \right) P_\chi. \tag{5.2.5}$$

5.2.3 Discussion

To reproduce Figs. 5.2.2**a-b**, we followed the idea of the experiments. The stability map of G_{BR} was calculated in 2 different scenarios: once by setting red QD to empty ($m = 0$), and to single occupation ($m = 1$). These conditions were achieved by fixing the level position at $\varepsilon_{\mathrm{BL}}/U_{\mathrm{BL}} = 0.5$ and $\varepsilon_{\mathrm{BL}}/U_{\mathrm{BL}} = -0.5$, respectively. The model parameters in Eq. 5.2.2 were estimated from the measurements ($U_{\mathrm{SC}} = 0.085\,\mathrm{meV}$, $\Delta = 0.075\,\mathrm{meV}$, $U_{\mathrm{BR}} = 1\,\mathrm{meV}$, $U_{\mathrm{BL}} = 0.4\,\mathrm{meV}$, $\delta_{\mathrm{SC}} = 0.85\,\mu\mathrm{eV}$, $\delta_{\mathrm{BR}} = 0.35\,\mathrm{meV}$, $C = 0.04\,\mathrm{meV}$, $V_{\mathrm{AC}} = 10\,\mu\mathrm{eV}$, $t_{\mathrm{BR}} = 0.04\,\mathrm{meV}$, and $t_{\mathrm{BL}} = 0.03\,\mathrm{meV}$), while we applied the $\varepsilon_{\mathrm{SC}} \sim -V_{\mathrm{SC}}$ and $\varepsilon_{\mathrm{BR}} \sim -V_{\mathrm{BR}}$ relations. The result of the simulations is shown in Fig. 5.2.5.

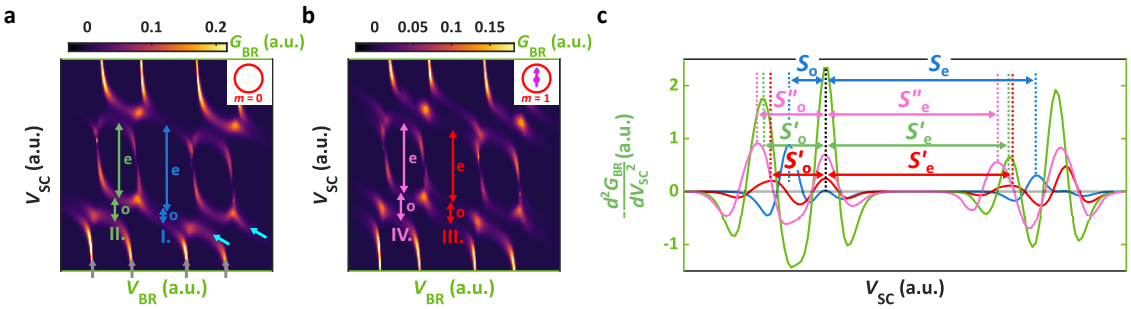

Figure 5.2.5: **Numerical simulation of the polyatomic Andreev molecule. a** Simulated zero-bias stability diagram for V_{BR} vs V_{SC} via the SCI-green double QD with the red QD being empty ($m = 0$). The sector with $n = 0$ green QD occupation of the blue arrows ($|0, N_0, 2\rangle$ states **I.**) owns a minor even-odd effect, while the $n = 1$ ones with the green arrows ($|0, N_0, 1\rangle$ states **II.**) displays an extended SCI odd state mimicing Fig. 5.2.2**a**. **b** Same as **a**, but captured at $m = 1$. The $|1, N_0, 2\rangle$ states along the red arrows (**III.**) have roughly the same diamond spacing as $|0, N_0, 1\rangle$ with green one from panel **a**. The SCI exhibits the strongest even-odd effect along the pink arrows (**IV.**) where the filling is $|1, N_0, 1\rangle$, in accordance with the experiments of Fig. 5.2.2**b**. **c** Calculated p plotted along the colored arrows in panels **a-b** providing a similar trend as in the measurement from Fig. 5.2.2**d**. The simulations were performed by the Author.

Fig. 5.2.5**a** imitates the measurement of Fig. 5.2.2**a** with the gray and cyan arrows indicating the green QD and SCI resonances, respectively. As explained above, here the red QD is empty (see the inset) and set into blockade. In the middle of the map, a pronounced even-odd effect with S_o and S_e odd and even SCI diamond sizes is visible shown by the blue arrows. They correspond to the $|0, N_0, 2\rangle$ states (labeled with **I.** previously), which exhibited quasi 2e charging in the experiments. Here the better resolution and smaller linewidth allow to distinguish the slightly split SCI resonances considered to be only a single peak in Fig. 5.2.2**a**. In the $|0, N_0, 1\rangle$ sector along the green lines (**II.**), the odd SCI diamond size S'_o is enhanced, which is attributed to a Coulomb-aided YSR singlet[149] settled between the SCI and the green QD, in accordance with the experiments.

Fig. 5.2.5**b** demonstrates the simulation with the same parameters as in panel **a**, but with the red QD being occupied with a single electron (see the inset), thus matching Fig. 5.2.2**b**. The $|1, N_0, 2\rangle$ states along the red arrows (**III.**) yield almost the same even-odd amplitudes, S'_o and S'_e, as the green ones in panel **a**. This is a signature of a YSR singlet residing in the SCI-red QD hybrid now. Nonetheless, the odd electron parity of the SCI S''_o is stabilized further in the

case of the $|1, N_0, 1\rangle$ configuration shown by the pink arrows (**IV.**) suggesting the hybridization of two Coulomb-aided YSR states.

For a quantitive analysis, we also plotted p along the colored arrows of panels **a-b** as a function of $V_{\rm SC}$, just like we did for the measured data, which is depicted in Fig. 5.2.5**c**. The curves have the same tendency as in the experiment in Fig. 5.2.2**d**, and the relative extension of the odd SCI diamond is estimated to be $\Delta S = (S''_o - S'_o)/(S_0 + S_e) \approx 10\%$. From the S'_o/S'_e (green and red curves) and S''_o/S''_e (pink curve) even odd amplitudes, we received $E_{\rm YSR,L(R)} \approx 45\,\mu$eV and $E_{\rm PAM} \approx 36\,\mu$eV single YSR state and polyatomic Andreev molecule energies slightly different from the experimental values.

In the framework of the model calculation, let us examine the spin character of the molecular state and the spin correlation between the electrons in the QDs. To comment on them, we consider a reduced version of the charge stability map by neglecting the second orbital on the green QD. Since the formation of a YSR singlet requires two electrons with opposite spins, naively, one expects that for the polyatomic Andreev molecule, $\Psi_{\rm PAM} = |1, 1, 1\rangle$, the red and green QD have parallel spins as they couple to the quasi-particle on the SCI with an anti-parallel one. To confirm this assumption, we calculated the correlator

$$\Theta = \langle \mathcal{S}^z_{\rm BL} \mathcal{S}^z_{\rm BR} \rangle, \tag{5.2.6}$$

for the reduced stability map of Fig. 5.2.4**b**, where

$$\mathcal{S}^z_{\rm BR(BL)} = n_{\rm BR(BL)\uparrow} - n_{\rm BR(BL)\downarrow} \tag{5.2.7}$$

operator measures the z-component of the spin in the green (red) QD.

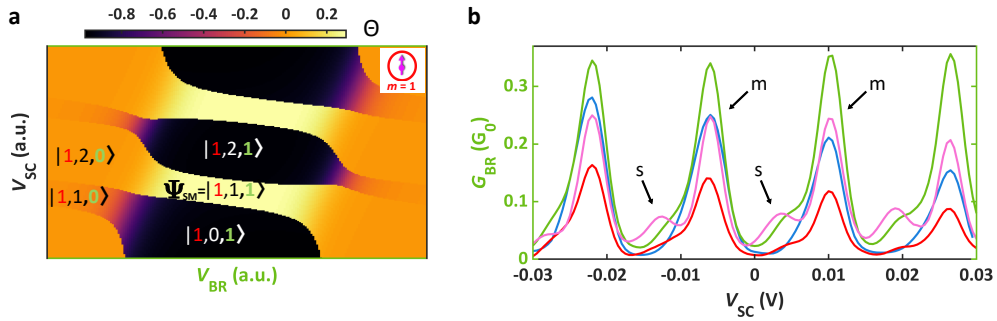

Figure 5.2.6: **Spin correlation in the QDs.** **a** Θ vs $V_{\rm BR}$ and $V_{\rm SC}$ with a single electron in the red QD. The correlator is finite when the green QD is also occupied by one electron ($|1, N_0, 1\rangle$ states). The $2n_0$ filling of the SCI induces an anti-ferromagnetic spin configuration, while the $2n_0 + 1$ does a ferromagnetic one. **b** Raw conductance curves of the SCI along the colored arrows in Figs. 5.2.2**a-b**. The Coulomb resonances have a built-in asymmetry regarding the amplitudes of the main peaks ("m") and the secondary ones ("s").

Fig. 5.2.6**a** shows the spin correlations, Θ, as a function of $V_{\rm BR}$ and $V_{\rm SC}$ while the red QD occupation was fixed at $m = 1$ by $\varepsilon_{\rm BL}/U_{\rm BL} = -0.5$ (see the inset). Obviously, the correlator gives roughly zero if the green QD has an even number of electrons, as $\mathcal{S}^z_{\rm BR(BL)} \approx 0$. This is visible in orange for small and large $V_{\rm BR}$. In the $|1, N_0, 1\rangle$ sectors, Θ takes a non-zero value. When the SCI has $2n_0$ even number of electrons (see the $|1, 0, 1\rangle$ or $|0, 2, 1$ states), the spins of the red and green QDs are perfectly anti-parallel deep in the blockade suggested by $\Theta < 0$. We note that Θ smoothly fades to zero by moving from the $|1, 2n_0, n + 1\rangle$ states to the $|1, 2n_0 + 1, n\rangle$ ones, e.g. along the transition from $|1, 0, 1\rangle$ to $|1, 1, 0\rangle$ as they are hybridized by tunneling. Nonetheless, $\Theta > 0$ is visible at the $|1, 1, 1\rangle$ polyatomic Andreev molecule sector, which corresponds to a rather parallel spin configuration. One can say that a ferromagnetic coupling between the QDs is managed by a superexchange via the SCI. This result was also confirmed by a very recent,

more elaborate model of Ref. 217.

Regarding the shape of the wave function, Ψ_{PAM} can be written as

$$\Psi_{\mathrm{PAM}} = |1,1,1\rangle = \sum_i \left(|S\rangle_{i,\mathrm{BR}} \otimes |\sigma\rangle_{\mathrm{BL}} - |S\rangle_{i,\mathrm{BL}} \otimes |\sigma\rangle_{\mathrm{BR}} \right). \tag{5.2.8}$$

Here $|S\rangle_{i,\mathrm{BR(BL)}}$ represents a singlet formed between the ith orbital of the SCI and the green (red) QD, and σ dentoes the ssame pin in the QDs. The summation indicates that both QDs retain a Coulomb-aided YSR singlet.

Finally, we comment on the asymmetry in the main and secondary SCI resonance amplitudes observed in the experiments, which was not recovered in the simulations. Fig. 5.2.6**b** reveals the raw data of the linecuts from Fig. 5.2.2 along the colored arrows (without differentiation) exhibiting the Coulomb resonances of the SCI. The colors of the curves correspond to the ones we used in Fig. 5.2.2**d**, i.e. coding the occupation of the red and green QDs. One can see that, regardless of the QD occupations, the main resonances (indicated by "m") have much higher amplitudes than the secondary ones (indicated by "s"). A possible explanation for this asymmetry is outlined in Ref. 219. In that work, the transport through a SCI and a strongly proximitized semiconducting nanowire below it is analyzed. It is argued that perhaps a robust, hardly tunable ABS exists parallel to the SCI, which governs the transport. As a result, the peak amplitudes of the $N_0 = 0 \longleftrightarrow 1$ and $N_0 = 1 \longleftrightarrow 2$ transitions differ due to the screening of the metal since they scale with u^2 and v^2 electron-hole components from Eqs. 2.2.41 and 2.2.42.

5.3 Conclusions

To conclude, we have realized a 3-atomic Andreev molecule as a result of the interplay between a SCI and two QDs. In simple transport measurements, by exploiting the even-odd effect, the character of the lowest energy states in the SCI was explored. We have found that two, single impurities residing in separate QDs can couple to the same quasi-particle and create a pair of interacting YSR states. We captured the formation of a polyatomic Andreev molecule from the YSR states step-by-step by tuning the QDs to the appropriate electron occupations. The minimal model we developed reproduced the main experimental findings and also predicted a ferromagnetic exchange between the QDs. The robust hybridization demonstrated in the molecular state is a proof of principle that strong coupling in polyatomic chains can be engineered. Regarding their diversity, SCI-QD hybrids are not only pioneers towards novel synthetic superconducting 1D crystals but also the first steps to achieving atomic level of manipulation in SCs[220] or new qubit concepts[221].

Chapter 6

Summary & outlooks

In the current work, we have studied parallel QDs coupled to a central SC in different experimental geometries, and now we summarize the results in a compressed manner.

The main purpose of the thesis was to discover the superconductivity-induced interaction between the QDs as the proposed structure was considered to be an elementary unit of a minimal Kiatev chain. After we reviewed the physical background and the sample fabrication techniques (from the simple electrostatic picture of QDs or the BCS theory of SCs to more complex systems, like ABSs, YSR states, or the behavior of superconducting grains) in Chapter 2, we moved to the characterization of the superconducting correlations governing the transport properties of the double QDs. The platform for our investigations was a pair of InAs nanowires grown in close vicinity and linked by an epitaxial superconducting Al shell[203] as a convenient material for our goals.

In Chapter 3, we reported a remarkable CPS signal in 3-terminal measurements of parallel QDs attached to a grounded SC electrode. With the application of parallel nanowires, the distance between the QDs was reduced significantly compared to single nanowire-based circuits, which was supposed to boost CPS since Cooper-pairs are separated at a shorter distance. Indeed, the maximal splitting efficiency was estimated as $s_{\max} \approx 45\%$ larger than the typical values measured in InAs nanowires from the litarature[84,86], despite the strong Coulomb repulsion between the QDs. The competition of the increased coherence factor gained from the small distance of the QDs and the parasitic capacitive coupling was analyzed, and we concluded that the parallel nanowire geometry is superior to the single one. This hypothesis was approved by the numerical simulation of a simple theoretical model. The results suggest the usage of parallel nanowires in novel superconducting circuits where the high-efficient separation of entangled electrons is desired, e.g. for coherent coupling of different qubits.

In Chapter 4, we demonstrated the experimental realization of a level-tunable, 2-atomic Andreev molecule, for the very first time in the literature. Two YSR states were hosted in separate QDs, which hybridized via a grounded SC serving as the medium for the interaction. By exploring the excitation spectra, we highlighted the spectral peculiarities of an Andreev molecule. The characteristic features were reproduced in a simple site model as well, and we distinguished the impact of EC, CAR, and the inter-dot Coulomb interaction[191]. Our result is a proof of principle that artificial atomic sites can be hybridized via a SC in a controlled way and an important milestone toward the realization of Kitaev chains[172]. Since the work has been published, the Andreev molecule has become a hot topic and intensively researched by many scientists in the field.

In Chapter 5, we constructed a polyatomic Andreev molecule in a QD-SCI-QD hybrid. Whereas the Andreev molecule discussed in Chapter 4 looked like the H_2, the polyatomic An-

dreev molecule resembles the H_2O structure among the conventional molceules, where the SCI played the role of the central oxygen atom. We utilized the strength of the even-odd effect typical for finite-size SCs to probe the ground state energies of different bound states shared between the SCI and the QDs. By adjusting both QDs to odd parity of electron occupation, we revealed that the unpaired impurities couple to the same quasi-particle of the SCI thereby establishing a bond pair of YSR states. The interpretation of the measurements was verified by a numerical model, which also predicted the ferromagnetic exchange between the QDs. These series of measurements demonstrated that polyatomic molecules with superconducting correlations involved can be tailed at will, which can have a great impact on building synthetic topological superconducting systems as a block of future quantum electronics.

All in all, we explored the interplay of a SC and a parallel double QD system in a wide variety of limits and geometries with DC transport measurement techniques. The studied molecular systems could be in the focus of other type of investigations as well, like phase-biasing of the Andreev molecule embedded into superconducting loops[209–212,222,223], or carring out spin correlation measurements with ferromagnetic electrodes. In addition, one might address the molecular states by microwave excitations, which are all within our future plans.

Chapter 7

Appendix

A.1 Numerical calculations

A.1.1 Representation of operators

To perform numerical calculations with the second quantized formalism, one has to implement the creation and annihilation operators as matrices acting on the corresponding subspace of the 2^N dimensional Fock space (assuming N different fermionic states). In the case of a single-site ($N = 1$, e.g. one electron with a specific spin) with the basis of 0 and 1 occupation, the creation and annihilation operators take the form of

$$c^\dagger = \begin{pmatrix} 0 & 0 \\ 1 & 0 \end{pmatrix}, \; c = \begin{pmatrix} 0 & 1 \\ 0 & 0 \end{pmatrix}, \tag{A.1.1}$$

with the basis of

$$|0\rangle = \begin{pmatrix} 1 \\ 0 \end{pmatrix}, \; |1\rangle = \begin{pmatrix} 0 \\ 1 \end{pmatrix}, \tag{A.1.2}$$

which is called the Jordan–Wigner transformation[224]. Now one might consider N sites and an operator acting on the m-th one. The creation operator can be obtained by a tensor product as

$$c_m^\dagger = \underbrace{\sigma_z \otimes \ldots \otimes \sigma_z}_{m-1} \otimes c^\dagger \otimes \underbrace{\sigma_0 \otimes \ldots \otimes \sigma_0}_{N-m}, \tag{A.1.3}$$

where σ_z is the Pauli-z matrix, σ_0 is the 2×2 identity matrix. The annihilation operator is given by $c_m = c_m^{\dagger T}$ as $c_m^\dagger$ being real. This composition guarantees the fermionic anti-commutation relation

$$\{c_i^\dagger, c_j\} = \delta_{ij}, \tag{A.1.4}$$

since σ_z counts the number of electrons occupying the first $m - 1$ states. The Hamiltonians in all of the numerical calculations are contructed by the composition of these N-by-N matrices, which are automatically diagonalized with an appropriate software.

A.1.2 Transition rates

To calculate the transport of any systems introduced in the thesis, the Master equation was solved in the stationary limit based on a transition rate equation model as

$$\begin{aligned} \frac{dP_i}{dt} = 0 &= \sum_{j\neq i}^{N} \left(W_{ij}P_j - W_{ji}P_i\right) \\ \sum_i P_i &= 1, \end{aligned} \tag{A.1.5}$$

where P_i is the occupation probability of state $|i\rangle$ and W_{ij} is the transition rate between states $|i\rangle$ and $|j\rangle$. Since it is an array of linear equations, Eq. A.1.5 can be rewritten in a matrix form of

$$\tilde{W}^{-1}\mathbf{Q} = \mathbf{P}, \tag{A.1.6}$$

where $\tilde{W}$ is a normalized matrix of W with the diagonal elements

$$\tilde{W}_{kk} = -\sum_{k'\neq k} W_{k'k}, \tag{A.1.7}$$

and $\tilde{W}_{Nk} = 1\ \forall k$, with N being the number of states, i.e the dimension of W. $\mathbf{P}$ is the N-dimensional vector with the unknown occupation probabilities as its elements, and $\mathbf{Q}$ is a vector with 1 in row N and 0 otherwise. Considering any site models, where the sites are coupled to normal leads, the transition rates are calculated by Fermi's golden rule[94] and they read as

$$\begin{aligned} W_{ij}\left(c_m^\dagger\right) &= \Gamma_m \left|\langle i|\, c_m^\dagger\, |j\rangle\right|^2\ f\left(E_j - E_i - \mu\right) \\ W_{ij}\left(c_m\right) &= \Gamma_m \left|\langle i|\, c_m\, |j\rangle\right|^2 \left(1 - f\left(E_i - E_j - \mu\right)\right). \end{aligned} \tag{A.1.8}$$

Here $c_m^{(\dagger)}$ is the annihilation (creation) operator of site m from Eq. A.1.3, $E_{i(j)}$ is the energy of state $|i(j)\rangle$, f is the Fermi function, μ is the chemical potential, and Γ_m is a coupling constant. The total transition rate between site m and a lead is simply the sum of $W = W\left(c_m^\dagger\right) + W\left(c_m\right)$. The current on the interface of the site and the lead is derived as

$$I = \frac{e}{\hbar}\sum_{i,j}\left(W_{ij}\left(c_m^\dagger\right) - W_{ij}\left(c_m\right)\right)P_j, \tag{A.1.9}$$

where the negative sign refers to the opposite direction of electron hopping between the on-site creation and annihilation.

A.2 Further data of measurements

A.2.1 Additional data for the analysis of Cooper pair splitting

In Chapter 3, the development of CPS signals was analyzed along single resonance lines. Here we provide additional data of other resonances exhibiting qualitatively similar behavior as discussed in Fig. 3.2.2, which is shown in Fig. A.2.1.

Figs. A.2.1**c-d** show G_L and G_R plotted along the resonance lines of the left and right QDs indicated by the blue and pink dashed lines in Figs. A.2.1**a-b**, respectively. While in Fig. A.2.1**c** the resonant right QD (green) acquires non-local peaks when the left QD is tuned to resonance too, the same applies in reverse in Fig. A.2.1**d**. At $V_\mathrm{L} = 3.45\,\mathrm{V}$ and $V_\mathrm{R} = -0.08\,\mathrm{V}$, where the QDs are resonant at the intersection of the blue and pink lines, $\Delta G \approx 8\,\mathrm{nA}$ is detected

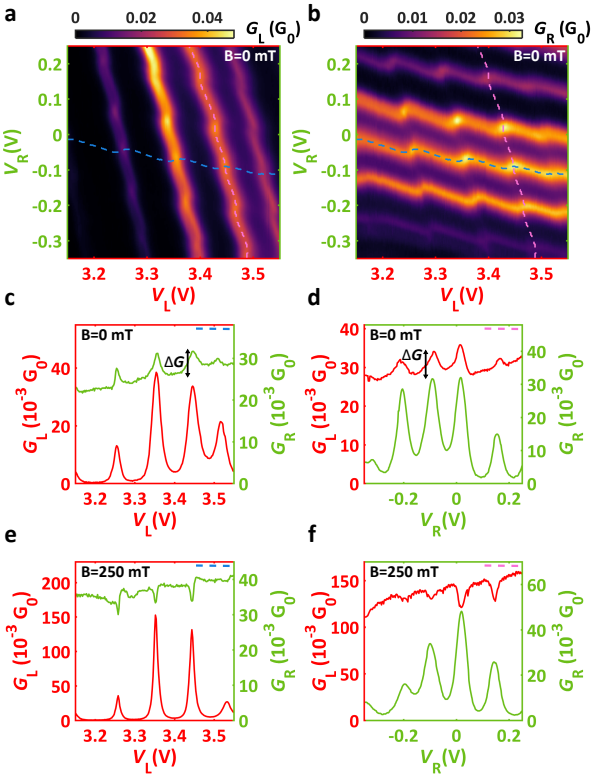

Figure A.2.1: **Supplementary analysis of CPS. a-b** Stability map of the left and right QDs in the superconducting state (same as Figs. 3.2.2**a-b**). **c-d** 1D conductance cuts taken along the blue and pink dashed lines in panel **a-b**. The non-local signals captured in both left and right QDs at $V_{\mathrm{L}} = 3.45\,\mathrm{V}$ and $V_{\mathrm{R}} = -0.08\,\mathrm{V}$ are measured by ΔG. **e-f** Same as panels **c-d**, but in the normal state. The non-local peaks are replaced by significant dips as a result of the finite U_{LR}.

equally in both cuts. In turn, these peaks vanish in the normal state and well-pronounced dips evolve instead of them (see Figs. A.2.1**e-f** for the same analysis as in panels **c-d** but without superconductivity). The depth of the dips usually exceeds 10% of the resonant signal.

As outlined in Chapter 3, we emphasize that these normal state minima originate from the shifting resonance lines as a result of the capacitive coupling between the QDs. The resistance of each line in the cryostat is $R_{\mathrm{W}} \approx 220\,\Omega$ ($1/R_{\mathrm{W}} \approx 50\,\mathrm{G}_0$), thus $R_{\mathrm{SC}} \ll R_{\mathrm{W}} \ll R_{\mathrm{L(R)}}$ is satisfied. Consequently, the same circuit model used in Ref. 84 can be applied to describe the classical resistive cross-talk. In the normal state, when the left (right) QD is on resonance, its conductance is expected to decrease ($\Delta G_{\mathrm{L(R)}}$), when the right (left, $\Delta G_{\mathrm{R(L)}}$) one also becomes resonant, since a larger current flows through the system thereby reducing the voltage drop on the SC. Quantitatively $\Delta G_{\mathrm{L(R)}} \approx \Delta G_{\mathrm{R(L)}} G_{\mathrm{L(R)}} R_{\mathrm{W}}$ is estimated, which falls in the order of $< 10^{-3}\,\mathrm{G}_0$ being negligible compared to the measured depth of the dips.

A.2.2 Standard YSR state

In Chapter 4, we mentioned that excitation spectra of $\mathrm{YSR_T}$ was examined far from any of the bottom QD resonances. Fig. A.2.2**a** shows the gate stability map and the traces of the spectroscopy recorded. As one can see, the lines are selected parallel to the bottom QD resonance, however, they are captured deep in the blockade along the entire map. This resulted in the measured spectra given in panels **b** and **c**, where the "eye-shaped" $\mathrm{YSR_T}$ state is observed without any any signals of $\mathrm{YSR_B}$ or signatures of hybridization. These excitation lines of the undisturbed $\mathrm{YSR_T}$ doublet are indicated in Figs. 4.3.1**k** and 4.4.1**l** with the white dashed lines. It is also notable that the evolution of the $\mathrm{YSR_T}$ state is insensitive to the ground state of the

YSR_B state as it is weakly coupled and evolves regardless of the parity of the electron number.

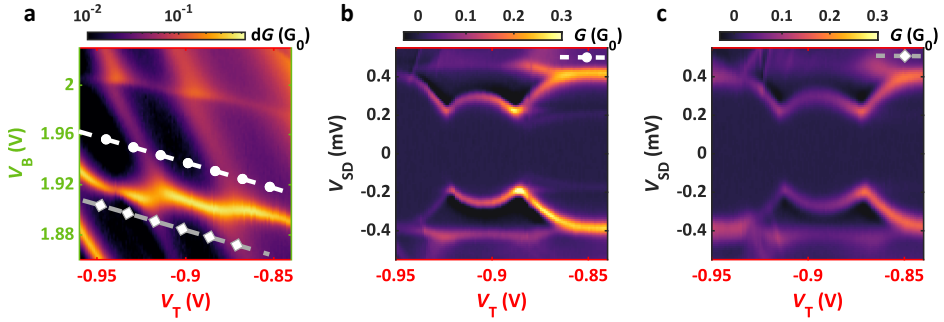

Figure A.2.2: **Undisturbed YSR state in device B**. **a** Gate stability map in the normal state (same as the one in Fig. 4.3.1). **b** Bias spectroscopy measurement along the dashed line from panel **a**. The YSR_T state is unaffected by the YSR_B one, which is bound to gap edge at $\Delta_1 + \Delta_2$ energy. **c** Similar to panel **b**, but measured along the other cut from panel **a** where YSR_B occupies different ground state parity.

The deviation of the YSR states is the strongest when the excitation energies of both YSR states are similar. However, in these particular measurements, the bottom QD is in blockade, therefore YSR_B is bound to the gap edge with the energy of $\Delta_1 + \Delta_2$. Consequently, YSR_B is screened by the quasi-particle continuum, and interaction is suppressed and undetectable[99]. Therefore the visibility of the hybridization is especially restricted in the spectroscopy measurements accomplished along YSR_T.

A.2.3 Finite-bias spectroscopy on the superconducting island-quantum dot hybrid

Here we demonstrate low-bias spectroscopy performed on the SCI-double QD hybrid device discussed in Chapter 5. The scpectra were captured with the red QD being empty ($m = 0$) and the green one being tuned, which are shown in Fig. A.2.3.

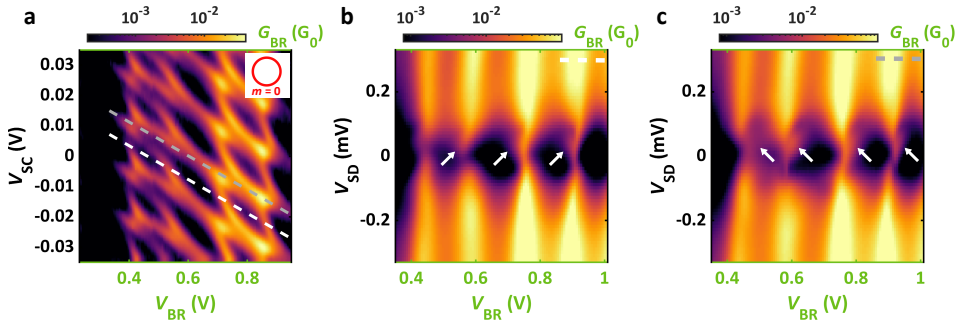

Figure A.2.3: **a** Same as Fig. 5.2.2**a** displaying the honeycomb pattern of the SCI and the green QD in G_{BR}. **b** Excitation spectra along the white (with even-occupied SCI) and **b** gray (with odd-occupied SCI) dashed lines from panel **a**. Clues of the "eye-shaped" evolution (see the white arrows) typical to YSR states are captured.

Panel **a** is the same stability map as Fig. 5.2.2**a**, where the stability diagram of the green QD-SCI hybrid was recorded locally via the green QD branch of Fig. 5.1.1**b**. Two different spectra are demonstrated: one with the SCI filled with even number of electrons ($|0, 0, n\rangle$ states along the white dashed line), and one with odd number of electrons ($|0, 1, n\rangle$ states along the white dashed line), which are shown in Figs. A.2.3**b-c**. In panel **b** the life time broadening limits the visibility of the sub-gap states, however, the signature of the distorted "eye shape"

of the Coulomb-aided YSR states can be recognized at the white arrows. This is even more manifest in panel **c**, where the YSR states seem to occupy a lower energies.

A.2.4 Cooper pair splitting via a SCI

In a completely different cooldown and settings, we captured the signature of CPS in the transport driven through the SCI-QD hybrid discussed in Chapter 5. For $U_{\mathrm{SC}} \lesssim \Delta$, the SCI is charged by 2e and the Andreev processes can dominate the transport. By coupling parallel QDs to the SCI weakly, in principle, a standard Cooper pair splitter circuit (discussed in Subsection 2.2.3 and Chapter 3) is obtained. Now we explore the clues of CPS in such circumstances.

In these particular experiments, QDs were established in the bottom right ("BR") and top right ("TR") nanowire segments as depicted in Fig. 5.1.1**b** by green and purple, respectively. Differential conductance $G_{\mathrm{BR}} = dI_{\mathrm{BR}}/dV_{\mathrm{AC}}$ and $G_{\mathrm{TR}} = dI_{\mathrm{TR}}/dV_{\mathrm{AC}}$ were measured via the "BR" and "TR" branches with the same technique as before, while the "BL" arm (previously hosting the red QD) was depleted and floated. As a result, the zero-bias current was recorded via the SCI-green QD and the SCI-purple QD hybrids simultaneously as illustrated in Fig. 5.1.1**b** with the effective circuit diagram in Fig. A.2.4**a**.

In this 3-QD system, the CPS is expected to be enhanced when both QDs and the SCI are set to resonance. While the QD level position dependence of the splitting efficiency at zero bias was discussed in Eq. 2.2.26, Cooper pairs can be transmitted through the SCI if it is resonant as well as shown in Fig. A.2.4**a**. Therefore to capture CPS signals, we performed such measurements where the green (purple) QD was kept on resonance, while the level position of the SCI and the purple (green) QD were tuned.

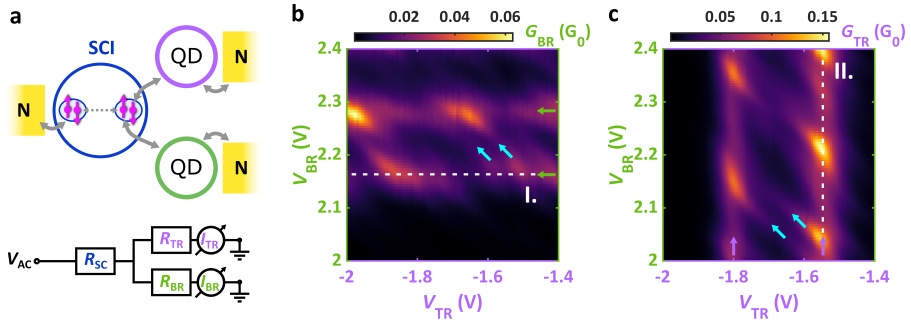

Figure A.2.4: **Setup for CPS measurements via the SCI. a** Schematic illustration of the pair splitting process via a SCI. The purple and green QDs were formed in the "TR" and "BR" nanowire segments in Fig. 5.1.1**b**. If the SCI is charged by 2e, the circuit resembles an ordinary CPS. The circuit diagram outlines the finite resistance of the SCI implying the resistive cross-talk when the QDs are tuned. **b** G_{BR} and **c** G_{TR} measured for different V_{BR} and V_{TR} plunger gate voltages. The resonances with the 3 dominant lever arms highlighted by the green, purple, and cyan arrows belong to the QDs and the SCI.

Fig. A.2.4**b** shows the zero-bias conductance measured via the green QD, G_{BR}, as a function of the QD plunger gate voltages V_{TR} and V_{BR}, while Fig. A.2.4**c** displays the same, but via the purple QD, G_{TR}. Similarly to Figs. 5.2.1**b-c**, resonance lines with 3 different slopes are present. The resonances shown by the green and purple arrows belong to the QDs with the corresponding color, while the cyan ones are attributed to the SCI again. This time the cross capacitance between the green and the purple QD is negligible.

At first, we set the green QD to the resonance at $V_{\mathrm{BR}} = 2.17\,\mathrm{V}$ marked by the **I.** dotted line in A.2.4**b**. Then we recorded the stability diagram of the purple QD and the SCI, i.e. measured the conductance as a function of V_{TR} and V_{SC} while keeping the QD resonant. The corresponding gate maps are shown in Figs. A.2.5**a-b**. Panel **a** demonstrates G_{TR}, considered to be the "local" signal, and panel **b** shows G_{BR}, the "non-local" one of the untuned green QD. In

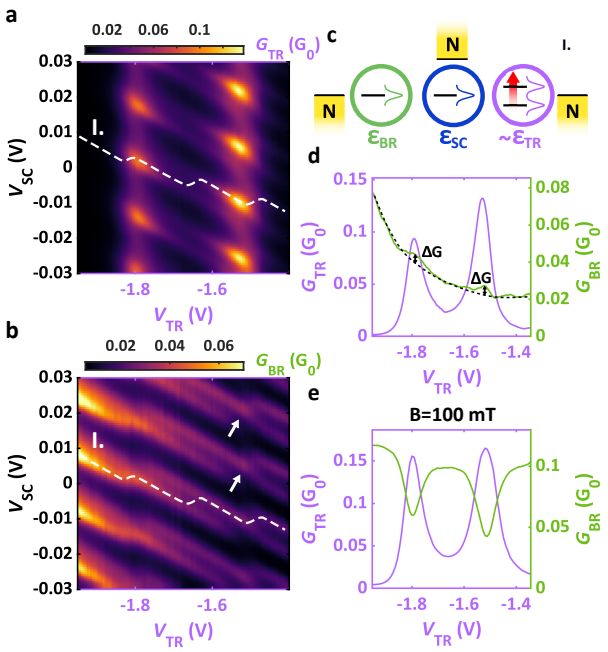

Figure A.2.5: **CPS detection on the SCI. a** Measured G_{TR} and **b** G_{BR} vs V_{TR} and V_{SC} with the green QD level position fixed along the white dotted line **I.** in Fig. A.2.4**b**. G_{BR} is enhanced at the purple QD resonances marked by the white arrows. **c** Illustration of the level positions along the white dashed line **I.** from panels **a-b**. $\varepsilon_{\mathrm{BR}}$ and $\varepsilon_{\mathrm{SC}}$ are kept constant, while $\varepsilon_{\mathrm{TR}}$ is varied. **d** G_{TR} and **b** G_{BR} plotted along the white dashed lines from panels **a-b** in the superconducting and **e** normal states. In the superconducting state, the two signals have positive correlations, in the normal state, they have negative ones.

panel **a** one can see the purple QD resonances at $V_{\mathrm{TR}} = -1.8\,\mathrm{V}$ and $V_{\mathrm{TR}} = -1.5\,\mathrm{V}$ gate voltage values, whereas the diagonal lines are identified as the SCI resonance lines exhibiting a weak even-odd effect. The latter feature is even more manifest in panel **b**, where the SCI is probed via the resonant green QD. However, this even-odd behavior disappears and turns into a clear 2e periodic one at the G_{TR} peak positions highlighted by the white arrows in panel **b**. In these points, the resonance conditions for all 3 QDs are satisfied and a conductance enhancement is detected. To visualize this effect, we focus on the evolution of G_{TR} and G_{BR} along a single SCI resonance traced by the white dashed line from panels **a-b**. In these curves, the level positions of the green QD and the SCI ($\varepsilon_{\mathrm{BR}}$ and $\varepsilon_{\mathrm{SC}}$) are aligned with the Fermi level in the normal leads, while the purple QD ($\varepsilon_{\mathrm{TR}}$) is tuned continuously, as explained by Fig. A.2.5**c**. The line cuts measured in the superconducting and normal states are shown in Figs. A.2.4**d-e**.

In panel **d**, G_{BR} has a decreasing trend in V_{TR}, whose baseline is indicated by the black dashed curve. This trend perhaps originates from the instability of the green QD level position unintentionally shifted slightly from resonance during the measurement. For any case, when the purple QD becomes resonant, additional peaks appear on the top of the trendline in G_{BR} labeled with ΔG. The positive peak correlations are replaced by dips providing that the superconductivity is switched off by a 100 mT out-of-plane magnetic field. This feature is the common sign of CPS as we have seen in Chapter 3.

The same analysis can be accomplished by reversing the roles of the green and purple QDs. Figs. A.2.5**a-b** show a series of measurements where the zero-bias stability diagram of the green QD-SCI hybrid was recorded as a function of V_{BR} and V_{SC} with the purple QD level position kept resonant. There $V_{\mathrm{TR}} = -1.5\,\mathrm{V}$ was set thereby bringing the purple QD to the resonance indicated by the white dotted **II.** line from Fig. A.2.4**c**. In this scenario, G_{TR} is recognized as the "non-local" signal, and G_{BR} is the "local" one. The SCI displays a clean 2e periodic

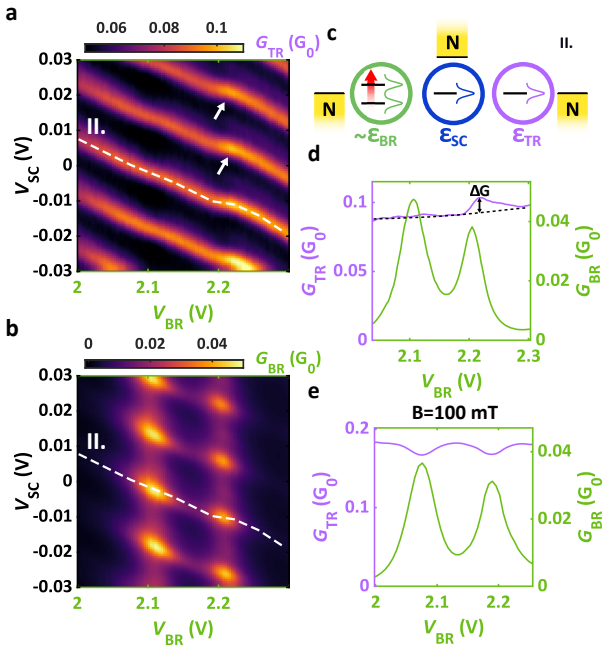

Figure A.2.6: **CPS detection on the SCI (with swapped roles of the green and purple QDs). a** Measured G_{TR} and **b** G_{BR} as a function of V_{BR} and V_{SC} with the purple QD level position fixed along the white dotted line **II.** in Fig. A.2.4**c** G_{TR} is enhanced at the green QD resonances (see the white arrows). **c** Similar to Fig. A.2.5**c**, but tuning the green QD ($\varepsilon_{\mathrm{BR}}$) instead of the purple one ($\varepsilon_{\mathrm{TR}}$) along the white dashed line **II.** from panels **a-b**. **d** Similar analysis of G_{TR} and **b** G_{BR} to Figs. A.2.5**d-e** plotted along the white dashed lines from panels **a-b** with and **e** without superconductivity. An additional peak at one of the green QD resonances appears in the signal of the purple QD in the superconducting state, while a solid negative correlation is observed in the normal state.

behavior, and a conductance enhancement of G_{TR} is visible at $V_{\mathrm{BR}} = 2.21\,\mathrm{V}$ (pointed by the white arrow in panel **a**) in coincidence with the green QD resonances. This feature tells us that the purple QD is responsible for renormalizing the even-odd effect of the SCI, which is not understood yet. Similarly to Figs. A.2.5**c-e** now we are interested in the conductance along linecuts where the entire "TR" arm is resonant ($\varepsilon_{\mathrm{SC}}$ and $\varepsilon_{\mathrm{TR}}$ are fixed) while the green QD level position ($\varepsilon_{\mathrm{BR}}$) is tuned as sketched in Fig. A.2.6**c**. Such curves taken along the white dashed lines II. from panels **a-b** are shown in Figs. A.2.6**d-e** in the superconducting and the normal states.

Although no clear peak is present at $V_{\mathrm{BR}} = 2,11\,\mathrm{V}$ in panel **d**, a finite ΔG increase is observed at $V_{\mathrm{BR}} = 2,21\,\mathrm{V}$ above the trendline illustrated by the black dashed line. Analogously to Fig. A.2.5**e**, this positive correlation turns into a negative one in the normal state of panel **e**, which hints the undergoing CPS processes in the device.

The average splitting efficiency was found to be $\overline{s_{\mathrm{SCI}}} \approx 5.5\%$ based on Eq. 2.2.28 with ΔG being measured from the trendlines of Figs. A.2.5**d** and A.2.6**d**. This value is much lower than what we obtained for the Cooper pair splitter device in Chapter 3 ($\overline{s} \approx 19 - 28\%$), which is not surprising as the SCI itself is only a Cooper pair box. We also mention that the dips appearing in Figs. A.2.5**e** and A.2.6**e** does not come from the Coulomb interaction of the QDs like in Chapter 3, but from the classical resistive cross-talk resetting the voltage drop in the junction. Since the SCI functions as a serial resistor (R_{SC}) in the circuit as explained by the cartoon in Fig. A.2.4**a**, once both the purple and green QDs are set to resonance, their total resistance (R_{TR} and R_{BR} connected in parallel) slightly decreases. The voltage is reduced on them as well, which ends up in a smaller current compared to the case when only one QD is resonant[84].

A.3 Sample fabrication details

A.3.1 Cooper pair splitter & multi-terminal superconducting island

The InAs nanowires were grown by molecular beam epitaxy (MBE) in the wurtzite phase along the ⟨0001⟩ direction catalyzed by Au. The pattern of the pre-defined Au droplets allowed to control the geometrical properties of the proposed parallel nanowires, including the diameter, distance, and the corresponding alignment of the cross-sections[179]. The 20-nm-thick Al shell (covering 2 facets) was evaporated at low temperature in-situ providing epitaxial, oxide-free layers. The evaporation on such a pair of adjacent nanowires resulted in the merging by the Al. Nanowires with $\sim$ 80 nm diameter, $\sim$ 4 μm length, and $\sim$ 200 nm seed separation were deposited on a p-doped Si wafer capped with 290 nm thick SiO_2 layer by using an optical transfer microscope with micromanipulators. The Al shell was partially removed by means of wet chemical etching. A coated MMA/MAA EL-6 double-layer performed as a masking layer, in which designed windows were opened with EBL allowing the MF-321 selective developer to access the Al (45 s). The etching was followed by a careful localization of the wires with high-resolution SEM. The contact electrodes were installed in a separate EBL step with a thicker PMMA resist (300 nm). Beam alignment was performed for every single devices in a 50 μm x 50 μm window. The sample was exposed to RF Ar milling in the evaporator chamber to remove the native oxide of both the Al and InAs. The process was followed by the metallization of Ti/Au (10/80 nm) with electron beam evaporation without breaking the vacuum. In a second EBL step, the side gate electrodes were created by using thinner PMMA resist (100 nm) and depositing Ti/Au (10/25 nm).

Low-temperature characterization was carried out in a Leiden Cryogenics dry dilution refrigerator with a base temperature of 40 mK. Transport measurements were performed with standard lock-in technique by applying 10 μV AC signal on the source (at 137 Hz and 114 Hz for the Cooper pair splitter and the multi-terminal SCI device, respectively), whereas the differential conductance of the nanowires was recorded separately via home-built I/V converters. DC bias was adjusted by the offset of the I/V converters. Out-of-plane magnetic field was realized by a superconducting magnet. The QDs and the overall potential along the nanowires were tuned by the outer finger gate electrodes.

A.3.2 Andreev molecule

The InAs nanowires were grown by MBE in the wurtzite phase along the ⟨0001⟩ direction catalyzed by Au. The pattern of the pre-defined Au droplets allowed to control the geometrical properties of the proposed double nanowires, including the diameter, distance, and the corresponding alignment of the cross-sections. The 20-nm-thick full-shell Al was evaporated at low temperature in-situ, by rotating the substrate, providing epitaxial, oxide-free layers. The evaporation on such a pair of adjacent nanowires resulted in the merging by the Al. Nanowires with $\sim$ 80 nm diameter and $\sim$ 4 μm length were deposited on a p-doped Si wafer capped with 290 nm thick SiO_2 layer by using an optical transfer microscope with micromanipulators. The Al shell on a $\sim$ 250 nm long segment was removed by means of wet chemical etching. A MMA/MAA EL-6 double-layer performed as a masking layer, which was locally exposed by EBL, allowing the MF-321 selective developer to access the Al (60 s). The etching was followed by a careful localization of the wires with high-resolution SEM. Both source-drain and side gate electrodes were installed in a common EBL step. The sample was exposed to RF Ar milling in the evaporator chamber to remove the native Al_2O_3. The process was followed by the metallization of Ti/Al (5/95 nm) without breaking the vacuum.

Low-temperature characterization was carried out in a Leiden Cryogenics dry dilution refrigerator with a base temperature of 40 mK. Transport measurements were performed with

standard lock-in technique by applying a $10\,\mu$V AC signal at 113 Hz on one of the SC electrodes, whereas the differential conductance was recorded via a home-built current amplifier on the other one. DC bias was adjusted by the offset of the amplifier. We note that due to the geometry, the features of both QDs were measured simultaneously in a single measurement, and hence, the sum of two excitation spectra was captured. Out-of-plane magnetic field was realized by an AMI superconducting magnet.

A.3.3 General recipies

Al etching on 20 nm half/full-shell

- AR-300 80 adhesion promoter, 4-5 drops next to the sample, cover it for 5 mins
- spin-coat: MMA(MAA) EL-6 150 nm @ 4000/40, bake @ 185°C, 90 s
- spin-coat: MMA(MAA) EL-6 150 nm @ 4000/40, bake @ 185°C, 90 s
- aperture: 20 kV, 10 um
- area dose: 80 uC/cm^2
- line dose: 450 pc/cm
- writefield: 500 um x 500 um, 10 nm stepsize
- development: MIBK:IPA, 1:3 60 s, IPA, 30 s, (N_2 dry)
- postbake: bake @ 120°C, 60 s
- etching: MF-321/MF-21A developer, T$\approx$ 35° vertically hang the sample, 45 s for half-shell, 60 s for full-shell, f $\approx$200 rpm stirring
- rinse: 50 ml DI-water 20 s
- rinse: 50 ml DI-water 20 s
- rinse: 50 ml DI-water 20 s
- removal of the mask: acetone @ 55 °C, 10 min, IPA, 60 s, (N_2 dry)

3-step lithography for parallel nanowires (CPS and polyatomic Andreev molecule devices)

- 1st round: normal contacts
  - spin-coat: AR-P 679 950K, 4%, 270 nm @ 4000/40, bake @ 170°C, 180 s
  - aperture: 20 kV, 10 um
  - area dose: 750 uC/cm^2
  - writefield: 50 um x 50 um, 2 nm stepsize
  - development: cold MIBK:IPA 1:3, 60 s, cold IPA, 30 s (N_2 dry), bake @ 110°C, 60 s
  - RF bias: Ar 10 sccm, 3 mTorr, 50 W, 6 min (8 min for contacting Al surface)
  - metallization: Ti 10 nm,1 A/s (Ti getter suggested), Au 80 nm, 4 A/s
  - lift-off: acetone @ 55 °C
- 2nd round: side gate electrodes with 100 nm periodicity

- spin-coat: AR-P 669 600K, 2.5%, 100 nm @ 4000/40, bake @ 150°C, 180 s
- aperture: 20 kV, 10 um
- area dose: 520 uC/cm^2
- line dose: 8000 pc/cm (dose test recommended)
- writefield: 50 um x 50 um, 2 nm stepsize
- development: cold MIBK:IPA, 1:3 60 s, cold IPA, 30 s (N_2 dry), bake @ 110°C, 60 s
- metallization: Ti 10 nm,1 A/s (Ti getter suggested), Au 30 nm, 2 A/s
- lift-off: acetone @ 55 °C, few 10 min, then syring, then sonication 1-2 s

- 3rd round: superconducting electrode with pads
  - spin-coat: AR-P 679 950K, 4% 270, nm @ 4000/40, or AR-P 669 600K, 5.1%, 300 nm @ 4000/40, bake @ 150°C, 180 s
  - aperture: 20 kV, 30 um
  - area dose: 290 uC/cm^2
  - writefield: 500 um x 500 um, 20 nm stepsize
  - development: MIBK:IPA, 1:3 60 s, IPA, 30 s (N_2 dry), bake @ 110°C, 60 s
  - RF bias: Ar 10 sccm, 3 mTorr, 50 W, 6 min (8 min for contacting Al surface)
  - metallization: Ti 5 nm,1 A/s (Ti getter suggested), Al 95 nm, 3 A/s
  - lift-off: acetone @ 55 °C

Acknowledgements

I would like to thank Dr. Szabolcs Csonka for the supervision, the offered opportunities, and all the help throughout the PhD.

I would also like to thank Dr. Péter Makk and Dr. Zoltán Scherübl for being my mentors with Dr. Szabolcs Csonka during the years.

I am grateful for the whole Quantum Electronics group and the Department of Physics, BUTE for all the support they gave, for the administration, and for our collaborators, the group of Dr. Jesper Nygård from the University of Copenhagen for their material support, and for EK MFA for providing their facilities for sample fabrication.

This research was supported by the Ministry of Innovation and Technology and the NKFIH within the Quantum Information National Laboratory of Hungary and by the Quantum Technology National Excellence Program, UNKP-22-3 and UNKP-23-4 New National Excellence Program of the Ministry for Innovation and Technology from the source of the National Research, Development and Innovation Fund.

References

[1] Moore, G. E. Gramming more components onto integrated circuits. *Electronics* **38**, 8 (1965).

[2] Waldrop, M. M. The chips are down for moore's law. *Nature News* **530**, 144 (2016).

[3] Feynman, R. P. Plenty of room at the bottom. In *APS annual meeting*, 1–7 (Little Brown Boston, MA, USA, 1959).

[4] DiVincenzo, D. P. The physical implementation of quantum computation. *Fortschritte der Physik: Progress of Physics* **48**, 771–783 (2000).

[5] Kaye, P., Laflamme, R. & Mosca, M. *An introduction to quantum computing* (OUP Oxford, 2006).

[6] Ladd, T. D. *et al.* Quantum computers. *nature* **464**, 45–53 (2010).

[7] Nielsen, M. A. & Chuang, I. L. *Quantum computation and quantum information* (Cambridge university press, 2010).

[8] Ekert, A. K. Quantum cryptography based on bell's theorem. *Physical review letters* **67**, 661 (1991).

[9] Chuang, I. L., Vandersypen, L. M., Zhou, X., Leung, D. W. & Lloyd, S. Experimental realization of a quantum algorithm. *Nature* **393**, 143–146 (1998).

[10] Jones, J. A., Mosca, M. & Hansen, R. H. Implementation of a quantum search algorithm on a quantum computer. *Nature* **393**, 344–346 (1998).

[11] Gisin, N., Ribordy, G., Tittel, W. & Zbinden, H. Quantum cryptography. *Reviews of modern physics* **74**, 145 (2002).

[12] DiCarlo, L. *et al.* Demonstration of two-qubit algorithms with a superconducting quantum processor. *Nature* **460**, 240–244 (2009).

[13] Arute, F. *et al.* Quantum supremacy using a programmable superconducting processor. *Nature* **574**, 505–510 (2019).

[14] Siddiqi, I. Engineering high-coherence superconducting qubits. *Nature Reviews Materials* **6**, 875–891 (2021).

[15] Elzerman, J. *et al.* Single-shot read-out of an individual electron spin in a quantum dot. *nature* **430**, 431–435 (2004).

[16] Koppens, F. H. *et al.* Driven coherent oscillations of a single electron spin in a quantum dot. *Nature* **442**, 766–771 (2006).

[17] Nowack, K. C., Koppens, F., Nazarov, Y. V. & Vandersypen, L. Coherent control of a single electron spin with electric fields. *Science* **318**, 1430–1433 (2007).

[18] Veldhorst, M. *et al.* An addressable quantum dot qubit with fault-tolerant control-fidelity. *Nature nanotechnology* **9**, 981–985 (2014).

[19] Pioro-Ladriere, M. *et al.* Electrically driven single-electron spin resonance in a slanting zeeman field. *Nature Physics* **4**, 776–779 (2008).

[20] Yoneda, J. *et al.* A quantum-dot spin qubit with coherence limited by charge noise and fidelity higher than 99.9%. *Nature nanotechnology* **13**, 102–106 (2018).

[21] Takeda, K., Noiri, A., Nakajima, T., Kobayashi, T. & Tarucha, S. Quantum error correction with silicon spin qubits. *Nature* **608**, 682–686 (2022).

[22] Van Der Wal, C. H. *et al.* Quantum superposition of macroscopic persistent-current states. *Science* **290**, 773–777 (2000).

[23] Chiorescu, I., Nakamura, Y., Harmans, C. M. & Mooij, J. Coherent quantum dynamics of a superconducting flux qubit. *Science* **299**, 1869–1871 (2003).

[24] You, J., Hu, X., Ashhab, S. & Nori, F. Low-decoherence flux qubit. *Physical Review B* **75**, 140515 (2007).

[25] Manucharyan, V. E., Koch, J., Glazman, L. I. & Devoret, M. H. Fluxonium: Single cooper-pair circuit free of charge offsets. *Science* **326**, 113–116 (2009).

[26] Peropadre, B., Forn-Díaz, P., Solano, E. & García-Ripoll, J. J. Switchable ultrastrong coupling in circuit qed. *Physical review letters* **105**, 023601 (2010).

[27] Yan, F. *et al.* The flux qubit revisited to enhance coherence and reproducibility. *Nature communications* **7**, 12964 (2016).

[28] Zazunov, A., Shumeiko, V., Bratus, E., Lantz, J. & Wendin, G. Andreev level qubit. *Physical review letters* **90**, 087003 (2003).

[29] Janvier, C. *et al.* Coherent manipulation of andreev states in superconducting atomic contacts. *Science* **349**, 1199–1202 (2015).

[30] Hays, M. *et al.* Direct microwave measurement of andreev-bound-state dynamics in a semiconductor-nanowire josephson junction. *Physical review letters* **121**, 047001 (2018).

[31] Tosi, L. *et al.* Spin-orbit splitting of andreev states revealed by microwave spectroscopy. *Physical Review X* **9**, 011010 (2019).

[32] Nakamura, Y., Pashkin, Y. A. & Tsai, J. S. Coherent control of macroscopic quantum states in a single-cooper-pair box. *nature* **398**, 786–788 (1999).

[33] Bladh, K., Duty, T., Gunnarsson, D. & Delsing, P. The single cooper-pair box as a charge qubit. *New Journal of Physics* **7**, 180 (2005).

[34] Wallraff, A. *et al.* Approaching unit visibility for control of a superconducting qubit with dispersive readout. *Physical review letters* **95**, 060501 (2005).

[35] Koch, J. *et al.* Charge-insensitive qubit design derived from the cooper pair box. *Physical Review A* **76**, 042319 (2007).

[36] Schreier, J. A. *et al.* Suppressing charge noise decoherence in superconducting charge qubits. *Physical Review B* **77**, 180502 (2008).

[37] Barends, R. *et al.* Coherent josephson qubit suitable for scalable quantum integrated circuits. *Physical review letters* **111**, 080502 (2013).

[38] Devoret, M. H. & Schoelkopf, R. J. Superconducting circuits for quantum information: an outlook. *Science* **339**, 1169–1174 (2013).

[39] Barends, R. *et al.* Superconducting quantum circuits at the surface code threshold for fault tolerance. *Nature* **508**, 500–503 (2014).

[40] Place, A. P. *et al.* New material platform for superconducting transmon qubits with coherence times exceeding 0.3 milliseconds. *Nature communications* **12**, 1779 (2021).

[41] Larsen, T. W. *et al.* Semiconductor-nanowire-based superconducting qubit. *Physical review letters* **115**, 127001 (2015).

[42] Zhuo, E. *et al.* Hole-type superconducting gatemon qubit based on ge/si core/shell nanowires. *npj Quantum Information* **9**, 51 (2023).

[43] Hutter, A. & Loss, D. Quantum computing with parafermions. *Physical Review B* **93**, 125105 (2016).

[44] Kitaev, A. Y. Fault-tolerant quantum computation by anyons. *Annals of Physics* **303**, 2–30 (2003).

[45] Nayak, C., Simon, S. H., Stern, A., Freedman, M. & Sarma, S. D. Non-abelian anyons and topological quantum computation. *Reviews of Modern Physics* **80**, 1083 (2008).

[46] Alicea, J., Oreg, Y., Refael, G., Von Oppen, F. & Fisher, M. P. Non-abelian statistics and topological quantum information processing in 1d wire networks. *Nature Physics* **7**, 412–417 (2011).

[47] Sarma, S. D., Freedman, M. & Nayak, C. Majorana zero modes and topological quantum computation. *npj Quantum Information* **1**, 1–13 (2015).

[48] Sau, J. D. & Sarma, S. D. Realizing a robust practical majorana chain in a quantum-dot-superconductor linear array. *Nature communications* **3**, 1–6 (2012).

[49] Loss, D. & DiVincenzo, D. P. Quantum computation with quantum dots. *Physical Review A* **57**, 120 (1998).

[50] Kouwenhoven, L. P., Austing, D. & Tarucha, S. Few-electron quantum dots. *Reports on progress in physics* **64**, 701 (2001).

[51] Hanson, R., Kouwenhoven, L. P., Petta, J. R., Tarucha, S. & Vandersypen, L. M. Spins in few-electron quantum dots. *Reviews of modern physics* **79**, 1217 (2007).

[52] Tarucha, S., Austing, D., Honda, T., Van der Hage, R. & Kouwenhoven, L. P. Shell filling and spin effects in a few electron quantum dot. *Physical Review Letters* **77**, 3613 (1996).

[53] Kouwenhoven, L. P. *et al.* Excitation spectra of circular, few-electron quantum dots. *Science* **278**, 1788–1792 (1997).

[54] Björk, M. T. *et al.* Few-electron quantum dots in nanowires. *Nano Letters* **4**, 1621–1625 (2004).

[55] Anderson, P. W. Localized magnetic states in metals. *Physical Review* **124**, 41 (1961).

[56] Weinmann, D., Häusler, W. & Kramer, B. Transport properties of quantum dots. *Annalen der Physik* **508**, 652–695 (1996).

[57] Eldridge, J., Pala, M. G., Governale, M. & König, J. Superconducting proximity effect in interacting double-dot systems. *Physical Review B* **82**, 184507 (2010).

[58] Jalabert, R. A., Stone, A. D. & Alhassid, Y. Statistical theory of coulomb blockade oscillations: Quantum chaos in quantum dots. *Physical review letters* **68**, 3468 (1992).

[59] Schoeller, H. & Schön, G. Mesoscopic quantum transport: Resonant tunneling in the presence of a strong coulomb interaction. *Physical Review B* **50**, 18436 (1994).

[60] Datta, S. *Electronic transport in mesoscopic systems* (Cambridge university press, 1997).

[61] Nazarov, Y. V. & Blanter, Y. M. *Quantum transport: introduction to nanoscience* (Cambridge university press, 2009).

[62] Landauer, R. Spatial variation of currents and fields due to localized scatterers in metallic conduction. *IBM Journal of research and development* **1**, 223–231 (1957).

[63] Kohn, W. & Luttinger, J. Quantum theory of electrical transport phenomena. *Physical Review* **108**, 590 (1957).

[64] Breit, G. & Wigner, E. Capture of slow neutrons. *Physical review* **49**, 519 (1936).

[65] Van der Wiel, W. G. *et al.* Electron transport through double quantum dots. *Reviews of Modern Physics* **75**, 1 (2002).

[66] Hewson, A. C. *The Kondo problem to heavy fermions.* 2 (Cambridge university press, 1997).

[67] Tinkham, M. *Introduction to superconductivity* (Courier Corporation, 2004).

[68] Sólyom, J. *Fundamentals of the Physics of Solids: Volume II: Electronic Properties*, vol. 2 (Springer Science & Business Media, 2008).

[69] Bardeen, J., Cooper, L. N. & Schrieffer, J. R. Theory of superconductivity. *Phys. Rev.* **108**, 1175–1204 (1957). URL `https://link.aps.org/doi/10.1103/PhysRev.108.1175`.

[70] Sólyom, J. *Fundamentals of the Physics of Solids: Volume 3-Normal, Broken-Symmetry, and Correlated Systems*, vol. 3 (Springer Science & Business Media, 2010).

[71] Pannetier, B. & Courtois, H. Andreev reflection and proximity effect. *Journal of low temperature physics* **118**, 599–615 (2000).

[72] de Gennes, P. Superconductivity of metals and alloys (1966).

[73] Zhu, J.-X. *Bogoliubov-de Gennes method and its applications*, vol. 924 (Springer, 2016).

[74] Meissner, H. Superconductivity of contacts with interposed barriers. *Physical Review* **117**, 672 (1960).

[75] Byers, J. M. & Flatté, M. E. Probing spatial correlations with nanoscale two-contact tunneling. *Physical review letters* **74**, 306 (1995).

[76] Deutscher, G. & Feinberg, D. Coupling superconducting-ferromagnetic point contacts by andreev reflections. *Applied Physics Letters* **76**, 487–489 (2000).

[77] Lesovik, G. B., Martin, T. & Blatter, G. Electronic entanglement in the vicinity of a superconductor. *The European Physical Journal B-Condensed Matter and Complex Systems* **24**, 287–290 (2001).

[78] Recher, P. & Loss, D. Superconductor coupled to two luttinger liquids as an entangler for electron spins. *Physical Review B* **65**, 165327 (2002).

[79] Beckmann, D., Weber, H. B. & v. Löhneysen, H. Evidence for crossed andreev reflection in superconductor-ferromagnet hybrid structures. *Physical Review Letters* **93** (2004). URL `http://dx.doi.org/10.1103/PhysRevLett.93.197003`.

[80] Russo, S., Kroug, M., Klapwijk, T. & Morpurgo, A. Experimental observation of bias-dependent nonlocal andreev reflection. *Physical review letters* **95**, 027002 (2005).

[81] Kleine, A., Baumgartner, A., Trbovic, J. & Schönenberger, C. Contact resistance dependence of crossed andreev reflection. *EPL (Europhysics Letters)* **87**, 27011 (2009). URL `http://dx.doi.org/10.1209/0295-5075/87/27011`.

[82] Recher, P., Sukhorukov, E. V. & Loss, D. Andreev tunneling, coulomb blockade, and resonant transport of nonlocal spin-entangled electrons. *Physical Review B* **63**, 165314 (2001).

[83] Cadden-Zimansky, P. & Chandrasekhar, V. Nonlocal correlations in normal-metal superconducting systems. *Physical review letters* **97**, 237003 (2006).

[84] Hofstetter, L., Csonka, S., Nygård, J. & Schönenberger, C. Cooper pair splitter realized in a two-quantum-dot y-junction. *Nature* **461**, 960–963 (2009).

[85] Herrmann, L. *et al.* Carbon nanotubes as cooper-pair beam splitters. *Physical review letters* **104**, 026801 (2010).

[86] Hofstetter, L. *et al.* Finite-bias cooper pair splitting. *Physical review letters* **107**, 136801 (2011).

[87] Schindele, J., Baumgartner, A. & Schönenberger, C. Near-unity cooper pair splitting efficiency. *Physical review letters* **109**, 157002 (2012).

[88] Das, A. *et al.* High-efficiency cooper pair splitting demonstrated by two-particle conductance resonance and positive noise cross-correlation. *Nature communications* **3**, 1–6 (2012).

[89] Deacon, R. S. *et al.* Cooper pair splitting in parallel quantum dot josephson junctions. *Nature communications* **6**, 1–7 (2015).

[90] Tan, Z. *et al.* Cooper pair splitting by means of graphene quantum dots. *Physical review letters* **114**, 096602 (2015).

[91] Tan, Z. *et al.* Thermoelectric current in a graphene cooper pair splitter. *Nature communications* **12**, 1–7 (2021).

[92] Ranni, A., Brange, F., Mannila, E. T., Flindt, C. & Maisi, V. F. Real-time observation of cooper pair splitting showing strong non-local correlations. *Nature communications* **12**, 1–6 (2021).

[93] Pandey, P., Danneau, R. & Beckmann, D. Ballistic graphene cooper pair splitter. *Physical review letters* **126**, 147701 (2021).

[94] Dirac, P. A. M. The quantum theory of the emission and absorption of radiation. *Proceedings of the Royal Society of London. Series A, Containing Papers of a Mathematical and Physical Character* **114**, 243–265 (1927).

[95] Sauret, O., Feinberg, D. & Martin, T. Quantum master equations for the superconductor–quantum dot entangler. *Physical Review B* **70**, 245313 (2004).

[96] Fülöp, G. *et al.* Magnetic field tuning and quantum interference in a cooper pair splitter. *Physical review letters* **115**, 227003 (2015).

[97] Baba, S. *et al.* Cooper-pair splitting in two parallel inas nanowires. *New Journal of Physics* **20**, 063021 (2018).

[98] Leijnse, M. & Flensberg, K. Coupling spin qubits via superconductors. *Physical review letters* **111**, 060501 (2013).

[99] Pillet, J. *et al.* Andreev bound states in supercurrent-carrying carbon nanotubes revealed. *Nature Physics* **6**, 965–969 (2010).

[100] Bretheau, L., Girit, Ç., Pothier, H., Esteve, D. & Urbina, C. Exciting andreev pairs in a superconducting atomic contact. *Nature* **499**, 312–315 (2013).

[101] Chang, W., Manucharyan, V., Jespersen, T., Nygård, J. & Marcus, C. Tunneling spectroscopy of quasiparticle bound states in a spinful josephson junction. *Physical review letters* **110**, 217005 (2013).

[102] Balatsky, A. V., Vekhter, I. & Zhu, J.-X. Impurity-induced states in conventional and unconventional superconductors. *Reviews of Modern Physics* **78**, 373 (2006).

[103] Buitelaar, M., Nussbaumer, T. & Schönenberger, C. Quantum dot in the kondo regime coupled to superconductors. *Physical Review Letters* **89**, 256801 (2002).

[104] Sand-Jespersen, T. *et al.* Kondo-enhanced andreev tunneling in inas nanowire quantum dots. *Physical review letters* **99**, 126603 (2007).

[105] Eichler, A. *et al.* Even-odd effect in andreev transport through a carbon nanotube quantum dot. *Physical Review Letters* **99**, 126602 (2007).

[106] Grove-Rasmussen, K. *et al.* Superconductivity-enhanced bias spectroscopy in carbon nanotube quantum dots. *Physical Review B* **79**, 134518 (2009).

[107] Deacon, R. *et al.* Tunneling spectroscopy of andreev energy levels in a quantum dot coupled to a superconductor. *Physical review letters* **104**, 076805 (2010).

[108] Dirks, T. *et al.* Transport through andreev bound states in a graphene quantum dot. *Nature Physics* **7**, 386–390 (2011).

[109] Martín-Rodero, A. & Yeyati, A. L. The andreev states of a superconducting quantum dot: mean field versus exact numerical results. *Journal of Physics: Condensed Matter* **24**, 385303 (2012).

[110] Pillet, J.-D., Joyez, P., Žitko, R. & Goffman, M. F. Tunneling spectroscopy of a single quantum dot coupled to a superconductor: From kondo ridge to andreev bound states. *Phys. Rev. B* **88**, 045101 (2013). URL `https://link.aps.org/doi/10.1103/PhysRevB.88.045101`.

[111] Lee, E. J. *et al.* Spin-resolved andreev levels and parity crossings in hybrid superconductor–semiconductor nanostructures. *Nature nanotechnology* **9**, 79–84 (2014).

[112] Jellinggaard, A., Grove-Rasmussen, K., Madsen, M. H. & Nygård, J. Tuning yu-shiba-rusinov states in a quantum dot. *Physical Review B* **94**, 064520 (2016).

[113] Gramich, J., Baumgartner, A. & Schönenberger, C. Andreev bound states probed in three-terminal quantum dots. *Phys. Rev. B* **96**, 195418 (2017).

[114] Scherübl, Z. *et al.* Large spatial extension of the zero-energy yu–shiba–rusinov state in a magnetic field. *Nature communications* **11**, 1–9 (2020).

[115] Prada, E. *et al.* From andreev to majorana bound states in hybrid superconductor–semiconductor nanowires. *Nature Reviews Physics* **2**, 575–594 (2020).

[116] Affleck, I., Caux, J.-S. & Zagoskin, A. M. Andreev scattering and josephson current in

a one-dimensional electron liquid. *Phys. Rev. B* **62**, 1433–1445 (2000). URL `https://link.aps.org/doi/10.1103/PhysRevB.62.1433`.

[117] Probst, B., Domínguez, F., Schroer, A., Yeyati, A. L. & Recher, P. Signatures of nonlocal cooper-pair transport and of a singlet-triplet transition in the critical current of a double-quantum-dot josephson junction. *Physical Review B* **94**, 155445 (2016).

[118] Grove-Rasmussen, K. *et al.* Yu-shiba-rusinov screening of spins in double quantum dots. *Nature Communications* **9**, 2376 (2018). URL `https://doi.org/10.1038/s41467-018-04683-x`.

[119] Yu, L. Bound state in superconductors with paramagnetic impurities. *Acta Physica Sinica* **114**, 75–91 (1965).

[120] Shiba, H. Classical spins in superconductors. *Progress of theoretical Physics* **40**, 435–451 (1968).

[121] Rusinov, A. Theory of gapless superconductivity in alloys containing paramagnetic impurities. *Sov. Phys. JETP* **29**, 1101–1106 (1969).

[122] Bogoljubov, N., Tolmachov, V. V. & Širkov, D. A new method in the theory of superconductivity. *Fortschritte der physik* **6**, 605–682 (1958).

[123] Trocha, P. & Weymann, I. Spin-resolved andreev transport through double-quantum-dot cooper pair splitters. *Physical Review B* **91**, 235424 (2015).

[124] Hussein, R., Jaurigue, L., Governale, M. & Braggio, A. Double quantum dot cooper-pair splitter at finite couplings. *Physical Review B* **94**, 235134 (2016).

[125] Meng, T., Florens, S. & Simon, P. Self-consistent description of andreev bound states in josephson quantum dot devices. *Physical Review B* **79**, 224521 (2009).

[126] Braggio, A., Governale, M., Pala, M. G. & König, J. Superconducting proximity effect in interacting quantum dots revealed by shot noise. *Solid State Communications* **151**, 155–158 (2011).

[127] Jørgensen, H. I., Novotnỳ, T., Grove-Rasmussen, K., Flensberg, K. & Lindelof, P. Critical current 0- π transition in designed josephson quantum dot junctions. *Nano letters* **7**, 2441–2445 (2007).

[128] Kocsis, M., Scherübl, Z., Fülöp, G., Makk, P. & Csonka, S. Strong nonlocal tuning of the current-phase relation of a quantum dot based andreev molecule. *arXiv preprint arXiv:2303.14842* (2023).

[129] Maurand, R. *et al.* First-order 0- π quantum phase transition in the kondo regime of a superconducting carbon-nanotube quantum dot. *Physical Review X* **2**, 011009 (2012).

[130] Szombati, D. *et al.* Josephson ϕ 0-junction in nanowire quantum dots. *Nature Physics* **12**, 568–572 (2016).

[131] Von Delft, J. & Ralph, D. C. Spectroscopy of discrete energy levels in ultrasmall metallic grains. *Physics Reports* **345**, 61–173 (2001).

[132] Richardson, R. A restricted class of exact eigenstates of the pairing-force hamiltonian (1963).

[133] Richardson, R. & Sherman, N. Exact eigenstates of the pairing-force hamiltonian. *Nuclear Physics* **52**, 221–238 (1964).

[134] Richardson, R. Exact eigenstates of the pairing-force hamiltonian. ii. *Journal of Mathematical Physics* **6**, 1034–1051 (1965).

[135] Braun, F. & Von Delft, J. Superconductivity in ultrasmall metallic grains. *Physical Review B* **59**, 9527 (1999).

[136] Black, C., Ralph, D. & Tinkham, M. Spectroscopy of the superconducting gap in individual nanometer-scale aluminum particles. *Physical Review Letters* **76**, 688 (1996).

[137] Ralph, D., Black, C. & Tinkham, M. Gate-voltage studies of discrete electronic states in aluminum nanoparticles. *Physical review letters* **78**, 4087 (1997).

[138] Tuominen, M., Hergenrother, J., Tighe, T. & Tinkham, M. Experimental evidence for parity-based 2e periodicity in a superconducting single-electron tunneling transistor. *Physical review letters* **69**, 1997 (1992).

[139] Averin, D. & Nazarov, Y. V. Single-electron charging of a superconducting island. *Physical review letters* **69**, 1993 (1992).

[140] Eiles, T. M., Martinis, J. M. & Devoret, M. H. Even-odd asymmetry of a superconductor revealed by the coulomb blockade of andreev reflection. *Physical review letters* **70**, 1862 (1993).

[141] Lafarge, P., Joyez, P., Esteve, D., Urbina, C. & Devoret, M. Measurement of the even-odd free-energy difference of an isolated superconductor. *Physical review letters* **70**, 994 (1993).

[142] Joyez, P., Lafarge, P., Filipe, A., Esteve, D. & Devoret, M. Observation of parity-induced suppression of josephson tunneling in the superconducting single electron transistor. *Physical review letters* **72**, 2458 (1994).

[143] Higginbotham, A. P. *et al.* Parity lifetime of bound states in a proximitized semiconductor nanowire. *Nature Physics* **11**, 1017–1021 (2015).

[144] Albrecht, S. M. *et al.* Exponential protection of zero modes in majorana islands. *Nature* **531**, 206–209 (2016).

[145] Albrecht, S. *et al.* Transport signatures of quasiparticle poisoning in a majorana island. *Physical review letters* **118**, 137701 (2017).

[146] Shen, J. *et al.* Parity transitions in the superconducting ground state of hybrid insb–al coulomb islands. *Nature communications* **9**, 4801 (2018).

[147] O'Farrell, E. *et al.* Hybridization of subgap states in one-dimensional superconductor-semiconductor coulomb islands. *Physical review letters* **121**, 256803 (2018).

[148] Vekris, A. *et al.* Electronic transport in double-nanowire superconducting islands with multiple terminals. *Nano Letters* **22**, 5765–5772 (2022).

[149] Pavešić, L., Bauernfeind, D. *et al.* Subgap states in superconducting islands. *Physical Review B* **104**, L241409 (2021).

[150] Estrada Saldaña, J. C. *et al.* Excitations in a superconducting coulombic energy gap. *Nature Communications* **13**, 1–8 (2022).

[151] Kitaev, A. Y. Unpaired majorana fermions in quantum wires. *Physics-Uspekhi* **44**, 131 (2001).

[152] Klinovaja, J. & Loss, D. Time-reversal invariant parafermions in interacting rashba nanowires. *Physical Review B* **90**, 045118 (2014).

[153] Reeg, C., Klinovaja, J. & Loss, D. Destructive interference of direct and crossed andreev pairing in a system of two nanowires coupled via an s-wave superconductor. *Physical Review B* **96**, 081301 (2017).

[154] Thakurathi, M., Simon, P., Mandal, I., Klinovaja, J. & Loss, D. Majorana kramers pairs in rashba double nanowires with interactions and disorder. *Physical Review B* **97**, 045415 (2018).

[155] Fazekas, P. *Lecture notes on electron correlation and magnetism*, vol. 5 (World scientific, 1999).

[156] Lutchyn, R. M., Sau, J. D. & Sarma, S. D. Majorana fermions and a topological phase transition in semiconductor-superconductor heterostructures. *Physical review letters* **105**, 077001 (2010).

[157] Oreg, Y., Refael, G. & Von Oppen, F. Helical liquids and majorana bound states in quantum wires. *Physical review letters* **105**, 177002 (2010).

[158] Lutchyn, R. M. *et al.* Majorana zero modes in superconductor–semiconductor heterostructures. *Nature Reviews Materials* **3**, 52–68 (2018).

[159] Zhang, H., Liu, D. E., Wimmer, M. & Kouwenhoven, L. P. Next steps of quantum transport in majorana nanowire devices. *Nature communications* **10**, 5128 (2019).

[160] Jespersen, T. S., Aagesen, M., Sørensen, C., Lindelof, P. E. & Nygård, J. Kondo physics in tunable semiconductor nanowire quantum dots. *Physical Review B* **74**, 233304 (2006).

[161] Csonka, S. *et al.* Giant fluctuations and gate control of the g-factor in inas nanowire quantum dots. *Nano letters* **8**, 3932–3935 (2008).

[162] Schroer, M., Petersson, K., Jung, M. & Petta, J. R. Field tuning the g factor in inas nanowire double quantum dots. *Physical review letters* **107**, 176811 (2011).

[163] Vaitiekėnas, S., Deng, M.-T., Nygård, J., Krogstrup, P. & Marcus, C. Effective g factor of subgap states in hybrid nanowires. *Physical review letters* **121**, 037703 (2018).

[164] Mourik, V. *et al.* Signatures of majorana fermions in hybrid superconductor-semiconductor nanowire devices. *Science* **336**, 1003–1007 (2012).

[165] Das, A. *et al.* Zero-bias peaks and splitting in an al–inas nanowire topological superconductor as a signature of majorana fermions. *Nature Physics* **8**, 887–895 (2012).

[166] Deng, M. *et al.* Majorana bound state in a coupled quantum-dot hybrid-nanowire system. *Science* **354**, 1557–1562 (2016).

[167] Gül, Ö. *et al.* Ballistic majorana nanowire devices. *Nature nanotechnology* **13**, 192–197 (2018).

[168] Grivnin, A., Bor, E., Heiblum, M., Oreg, Y. & Shtrikman, H. Concomitant opening of a bulk-gap with an emerging possible majorana zero mode. *Nature communications* **10**, 1–7 (2019).

[169] Pan, H. & Sarma, S. D. Physical mechanisms for zero-bias conductance peaks in majorana nanowires. *Physical Review Research* **2**, 013377 (2020).

[170] Choi, M.-S., Bruder, C. & Loss, D. Spin-dependent josephson current through double quantum dots and measurement of entangled electron states. *Physical review B* **62**, 13569 (2000).

[171] Flatté, M. E. & Reynolds, D. E. Local spectrum of a superconductor as a probe of interactions between magnetic impurities. *Physical Review B* **61**, 14810 (2000).

[172] Leijnse, M. & Flensberg, K. Parity qubits and poor man's majorana bound states in double quantum dots. *Physical Review B* **86**, 134528 (2012).

[173] Prada, E., Aguado, R. & San-Jose, P. Measuring majorana nonlocality and spin structure with a quantum dot. *Physical Review B* **96**, 085418 (2017).

[174] Tsintzis, A., Souto, R. S. & Leijnse, M. Creating and detecting poor man's majorana bound states in interacting quantum dots. *Physical Review B* **106**, L201404 (2022).

[175] Dvir, T. *et al.* Realization of a minimal kitaev chain in coupled quantum dots. *Nature* **614**, 445–450 (2023).

[176] Zatelli, F. *et al.* Robust poor man's majorana zero modes using yu-shiba-rusinov states. *arXiv preprint arXiv:2311.03193* (2023).

[177] Bordin, A. *et al.* Crossed andreev reflection and elastic co-tunneling in a three-site kitaev chain nanowire device. *arXiv preprint arXiv:2306.07696* (2023).

[178] Fülöp, G. *et al.* Local electrical tuning of the nonlocal signals in a cooper pair splitter. *Physical Review B* **90**, 235412 (2014).

[179] Kanne, T. *et al.* Double nanowires for hybrid quantum devices. *Advanced Functional Materials* **32**, 2107926 (2022).

[180] Kürtössy, O. *et al.* Andreev molecule in parallel inas nanowires. *Nano Letters* **21**, 7929–7937 (2021).

[181] Vekris, A. *et al.* Josephson junctions in double nanowires bridged by in-situ deposited superconductors. *Phys. Rev. Research* **3**, 033240 (2021). URL `https://link.aps.org/doi/10.1103/PhysRevResearch.3.033240`.

[182] Vekris, A. *et al.* Asymmetric little–parks oscillations in full shell double nanowires. *Scientific Reports* **11** (2021). URL `http://dx.doi.org/10.1038/s41598-021-97780-9`.

[183] Krogstrup, P. *et al.* Epitaxy of semiconductor–superconductor nanowires. *Nature materials* **14**, 400–406 (2015).

[184] Chang, W. *et al.* Hard gap in epitaxial semiconductor–superconductor nanowires. *Nature nanotechnology* **10**, 232–236 (2015).

[185] Pobell, F. *Matter and methods at low temperatures* (Springer Science & Business Media, 2013).

[186] Walldorf, N., Padurariu, C., Jauho, A.-P. & Flindt, C. Electron waiting times of a cooper pair splitter. *Physical Review Letters* **120**, 087701 (2018).

[187] Walldorf, N., Brange, F., Padurariu, C. & Flindt, C. Noise and full counting statistics of a cooper pair splitter. *Physical Review B* **101**, 205422 (2020).

[188] Brange, F., Prech, K. & Flindt, C. Dynamic cooper pair splitter. *Physical review letters* **127**, 237701 (2021).

[189] Ueda, K. *et al.* Dominant nonlocal superconducting proximity effect due to electron-electron interaction in a ballistic double nanowire. *Science Advances* **5**, eaaw2194 (2019).

[190] Kürtössy, O. *et al.* Parallel inas nanowires for cooper pair splitters with coulomb repulsion. *Npj Quantum Materials* **7**, 88 (2022).

[191] Scherübl, Z., Pályi, A. & Csonka, S. Transport signatures of an andreev molecule in a quantum dot–superconductor–quantum dot setup. *Beilstein Journal of Nanotechnology* **10**, 363–378 (2019).

[192] López, R., Choi, M.-S. & Aguado, R. Josephson current through a kondo molecule. *Physical Review B* **75**, 045132 (2007).

[193] Lee, M., López, R., Aguado, R. & Choi, M.-S. Josephson current in strongly correlated double quantum dots. *Physical review letters* **105**, 116803 (2010).

[194] Yao, N. Y. *et al.* Phase diagram and excitations of a shiba molecule. *Physical Review B* **90**, 241108 (2014).

[195] Wrześniewski, K., Trocha, P. & Weymann, I. Current cross-correlations in double quantum dot based cooper pair splitters with ferromagnetic leads. *Journal of Physics: Condensed Matter* **29**, 195302 (2017).

[196] Pillet, J.-D., Benzoni, V., Griesmar, J., Smirr, J.-L. & Girit, Ç. Ö. Scattering description of andreev molecules. *SciPost Physics Core* **2**, 009 (2020).

[197] Kezilebieke, S., Dvorak, M., Ojanen, T. & Liljeroth, P. Coupled yu–shiba–rusinov states in molecular dimers on nbse2. *Nano letters* **18**, 2311–2315 (2018).

[198] Ruby, M., Heinrich, B. W., Peng, Y., von Oppen, F. & Franke, K. J. Wave-function hybridization in yu-shiba-rusinov dimers. *Physical review letters* **120**, 156803 (2018).

[199] Choi, D.-J. *et al.* Influence of magnetic ordering between cr adatoms on the yu-shiba-rusinov states of the β- bi 2 pd superconductor. *Physical review letters* **120**, 167001 (2018).

[200] Beck, P. *et al.* Spin-orbit coupling induced splitting of yu-shiba-rusinov states in antiferromagnetic dimers. *Nature communications* **12**, 1–9 (2021).

[201] Ding, H. *et al.* Tuning interactions between spins in a superconductor. *Proceedings of the National Academy of Sciences* **118** (2021).

[202] Su, Z. *et al.* Andreev molecules in semiconductor nanowire double quantum dots. *Nature Communications* **8**, 1–6 (2017).

[203] Kanne, T. *et al.* Double nanowires for hybrid quantum devices. *Advanced functional materials* **32**, 2107926 (2022).

[204] Anselmetti, G. *et al.* End-to-end correlated subgap states in hybrid nanowires. *Physical Review B* **100**, 205412 (2019).

[205] Van der Wiel, W. *et al.* The kondo effect in the unitary limit. *Science* **289**, 2105–2108 (2000).

[206] Eichler, A. *et al.* Tuning the josephson current in carbon nanotubes with the kondo effect. *Physical Review B* **79**, 161407 (2009).

[207] Dynes, R. C., Narayanamurti, V. & Garno, J. P. Direct measurement of quasiparticle-lifetime broadening in a strong-coupled superconductor. *Physical Review Letters* **41**, 1509 (1978).

[208] Herman, F. & Hlubina, R. Microscopic interpretation of the dynes formula for the tunneling density of states. *Physical Review B* **94**, 144508 (2016).

[209] Haxell, D. Z. *et al.* Demonstration of the nonlocal josephson effect in andreev molecules. *Nano Letters* **23**, 7532–7538 (2023).

[210] Coraiola, M. *et al.* Phase-engineering the andreev band structure of a three-terminal josephson junction. *Nature Communications* **14**, 6784 (2023).

[211] Matsuo, S. *et al.* Phase engineering of anomalous josephson effect derived from andreev molecules. *Science Advances* **9**, eadj3698 (2023).

[212] Matsuo, S. *et al.* Phase-dependent andreev molecules and superconducting gap closing in coherently-coupled josephson junctions. *Nature Communications* **14** (2023).

[213] Pillet, J.-D., Benzoni, V., Griesmar, J., Smirr, J.-L. & Girit, C. O. Nonlocal josephson effect in andreev molecules. *Nano letters* **19**, 7138–7143 (2019).

[214] Bordin, A. *et al.* Tunable crossed andreev reflection and elastic cotunneling in hybrid nanowires. *Physical Review X* **13**, 031031 (2023).

[215] Terhal, B. M., Hassler, F. & DiVincenzo, D. P. From majorana fermions to topological order. *Physical Review Letters* **108**, 260504 (2012).

[216] Plugge, S., Rasmussen, A., Egger, R. & Flensberg, K. Majorana box qubits. *New Journal of Physics* **19**, 012001 (2017).

[217] Bácsi, Á., Pavešić, L. *et al.* Exchange interaction between two quantum dots coupled through a superconducting island. *Physical Review B* **108**, 115160 (2023).

[218] Hergenrother, J., Tuominen, M. & Tinkham, M. Charge transport by andreev reflection through a mesoscopic superconducting island. *Physical review letters* **72**, 1742 (1994).

[219] Hansen, E. B., Danon, J. & Flensberg, K. Probing electron-hole components of subgap states in coulomb blockaded majorana islands. *Physical Review B* **97**, 041411 (2018).

[220] Saldaña, J. C. E. *et al.* Richardson model with complex level structure and spin-orbit coupling for hybrid superconducting islands: Stepwise suppression of pairing and magnetic pinning. *Physical Review B* **108**, 224507 (2023).

[221] Malinowski, F. K. Two anderson impurities coupled through a superconducting island: charge stability diagrams and double impurity qubit. *arXiv preprint arXiv:2303.14410* (2023).

[222] Matsuo, S. *et al.* Observation of nonlocal josephson effect on double inas nanowires. *Communications Physics* **5**, 221 (2022).

[223] Matsuo, S. *et al.* Josephson diode effect derived from short-range coherent coupling. *Nature Physics* **19**, 1636–1641 (2023).

[224] Jordan, P. & Wigner, E. P. *Über das Paulische Äquivalenzverbot*, 109–129 (Springer Berlin Heidelberg, Berlin, Heidelberg, 1993). URL `https://doi.org/10.1007/978-3-662-02781-3_9`.